Electron Thermal Transport Modeling of Laser-Plasmas

by

Kevin H. Ma

A dissertation submitted in partial fulfillment
of the requirements for the degree of
Doctor of Philosophy
(Mechanical Engineering)
in The University of Michigan
2024

Doctoral Committee:

Professor Eric Johnsen, Chair
Assistant Professor Rohini Bala Chandran
Professor R. Paul Drake
Associate Professor Carolyn Christine Kuranz
Dr. Mehul Vasant Patel, Lawrence Livermore National Laboratory

Kevin H. Ma

kevima@umich.edu

ORCID iD: 0000-0001-6722-3944

2024

To my grandparents.

In particular, to my late grandmother 外婆.

Thank you for teaching me how to cook eggs.

ACKNOWLEDGEMENTS

This dissertation is the final part of a long and difficult journey. This is because the duration of my graduate school studies was, objectively speaking, quite long. And my experience felt, subjectively speaking, quite difficult. Perhaps this statement would be better expounded upon in a *Preface*, but my intention in disclosing this information in this preamble is to emphasize how important the people in my life were to me during this time. Otherwise, that is all I will speak of about that.

First, I would like to extend deep gratitude to those I have met during my graduate studies at the University of Michigan and at other academic and research institutions, in passing during my travels as well as at the conferences and workshops I traveled to, in cities like Ann Arbor, Raleigh, San Francisco, Atlanta, back home in New Jersey and in various other places I have inhabited during these years. This includes friends, acquaintances, and foes – everyone. From shared moments and experiences with you, I have felt joy, pain, admiration, jealousy, and many, many other emotions. But most importantly, amidst the doldrums I have felt *alive*. So I am grateful–if only for that–to have known each and every one of you.

Now I would like to thank the individuals that have graciously agreed to serve on my committee. I would like to thank Paul Drake, Carolyn Kuranz, and Rohini Bala Chandran. Frequently my communications with you are quite urgent, but somehow you have always been responsive and helpful to me. I will always appreciate that. Next, I would like to thank Mehul Patel. Our collaboration is the most wonderful experience I have had during my graduate tenure, and your mentorship over these

years has been invaluable to my success. More importantly, I am grateful for your friendship, which I cherish and hope to keep into the future. And I would like to thank my advisor, Eric Johnsen. Our advisor-advisee relationship was intimate but also difficult, yet you always endeavored to listen and to offer your help. This work would not have been possible without your patience and support.

Finally I would like to thank my family. Firstly, a warmest welcome to my niece, Minerva, and to my nephew, Irving. Thank you for the joy that you bring, the possibilities that you embody, and the love and kinship that you share with each other. And I am grateful to my own siblings. To my older sister, Annie, for being a magnificent role model and for your wisdom. To my older brother, Dennis, for being my greatest confidant. To my younger sister, Christie, for sharing so many interests and experiences, so that I never truly felt alone. And last of all, to my mother and my father, for everything I have already mentioned, and for everything else.

This work was funded by the Lawrence Livermore National Laboratory under subcontract B632749, and was performed under the auspices of the U.S. Department of Energy by Lawrence Livermore National Laboratory under Contract No. DE-AC52-07NA27344.

TABLE OF CONTENTS

LIST OF FIGURES

Figure

LIST OF APPENDICES

Appendix

LIST OF ABBREVIATIONS

HED High-energy-density

ICF Inertial confinement fusion

NIF National Ignition Facility

SNB Schurtz-Nicolai-Busquet

SH Spitzer-Harm

EOS Equations of state

LEOS Livermore equations of state

LPI Laser-plasma interactions

IB inverse-bremsstrahlung

LTE Local thermodynamic equilibrium

NLTE Non-[Local thermodynamic equilibrium]

VFP Vlasov-Fokker-Planck

EDF Electron distribution function

EEDF Electron energy distribution function

ABSTRACT

A longstanding challenge in the field of high-energy-density physics is the development of a predictive simulation framework for inertial confinement fusion (ICF) experiments, which are complex multi-physics systems that span a large range of length scales and timescales. Computational approaches for modeling these integrated systems often employ simplified or reduced-order models for many of these physical processes, coupled with numerical multipliers to account for deficiencies in the physics modeling. For electron heat transport, flux-limiters are often employed in conjunction with the classical Spitzer-Harm electron conduction model. To address such deficiencies in electron heat transport modeling, this dissertation evaluates the effect of nonlocal deviations in the electron heat flux that emerges due to the presence of steep temperature gradients, as represented by the reduced-order nonlocal multigroup diffusion model proposed by Schurtz, Nicolai, and Busquet (SNB).

In current direct- and indirect-drive ICF approaches, lasers produce 3ω (353 nm) light, which delivers the energy required to compress the fusion fuel. In the interaction of laser light with initially solid matter, steep temperature gradients–where nonlocal transport is expected–are produced. Historically, laser-irradiated sphere experiments have been used to study laser-plasmas at ICF-relevant conditions, specifically to study the radiative properties of high-Z elements. To focus on the effect of electron transport, our computational study focuses on low- to mid-Z spheres where modeling uncertainties from radiation transport and non local thermodynamic equilibrium

(NLTE) atomic kinetics are smaller. In the laser-irradiated sphere, we benchmark a corrected form of the SNB model against Vlasov-Fokker-Planck kinetic modeling and find it matches kinetic heat flux predictions within 10%. This is an improvement to errors up to 40% from SNB heat flux predictions without these corrections. This work represents the first suite of integrated-modeling comparisons using this form of the SNB model. Compared to classical transport, we find that nonlocal electron transport produces a cooler expanded plasma corona due to anomalous heat flux reduction, and enhanced self X-ray emissions due to anomalous preheat. These nonlocal behaviors cannot be reproduced from classical electron heat flux predicted by the Spitzer-Harm model, with or without flux limiters.

Furthermore, when the electron heat transport becomes nonlocal the electron distribution becomes non-Maxwellian. And at ICF relevant laser intensities non-Maxwellian electrons are produced by the collisional absorption of laser light and by parametric laser-plasma-instabilities (LPI). Our approach employs atomic-kinetics simulations to assess the effect of such non-Maxwellian distributions on the radiative properties of the plasma from laser-irradiated spheres, using information from Vlasov-Fokker-Planck kinetic simulations or analytical theory. This approach is applied in zero-dimensional plasmas, as well as one-dimensional plasma profiles from the laser-sphere. From one-dimensional comparisons, we find the impact of non-Maxwellian electrons from nonlocal transport and from collisional laser absorption on the radiation emissions ($<$1%) and the $K-$shell line intensities ($<$10%) is minimal. These differences may not be experimentally significant, suggesting that the SNB model is sufficient for modeling electron transport in laser-irradiated spheres. Furthermore, our approach can be used to assess the effect of non-Maxwellian electrons from other physical processes, such as a number of LPI effects.

CHAPTER I

Introduction

This chapter describes the motivation and applications of the present work in the fields of physics and engineering, and outlines the scope of this dissertation . This research is relevant to inertial confinement fusion efforts within the context of high-energy-density physics, which is first described and subsequently followed by a broad description of various physical energy transport mechanisms that feature in this regime of physics. Of the many physics inherent in these high-energy-density physics systems, this work primarily focuses upon electron thermal transport. Accordingly, this chapter features a more detailed discussion of various approaches for calculating electron heat transport in laser-plasmas modeling. Finally, we provide an overview of this dissertation, including an outline complete with the objective of each chapter.

1.1 Inertial Confinement Fusion

In high-energy-density (HED) physics, matter is subject to pressures of approximately one million atmospheres or greater ($\gtrsim$ 1 Mbar) [3]. Fundamentally, the transition to the HED regime occurs when the applied pressures are comparable to the internal energy of molecules and atoms. This enables matter to ionize, leading to a plasma state composed of liberated, negatively-charged electrons and positively-charged ions as opposed to neutral particles. Compared to neutral states of matter,

collective effects from Coulomb interactions significantly influence the behavior and evolution of plasmas [4]. Additional avenues of energy transport emerge from the new-founded motility of electrons [5] and from the radiative fluxes that scale strongly with temperature [6]. Intrinsically, equations of state (EOS) become more complex due to additional thermodynamic degrees of freedom from ionization and other mechanisms. Figure 1.1 shows the regimes of high-energy-density plasmas, which span a broad parameter space over 16+ orders of magnitude in mass density, and 10+ orders of magnitude in temperature. Within this HED landscape exist processes that drive nuclear fusion, both in laboratory experiments and in the cosmos.

Nuclear fusion is a reaction where multiple atomic nuclei combine to form a heavier nucleus and subatomic particles. This reaction fuses lighter elements (beginning with hydrogen) into heavier elements and is exothermic, i.e. excess energy is released, for atoms lighter than iron. The fusion reaction requires overcoming the electrostatic force that repels like-charged atomic nuclei, necessitating very high pressures and temperatures. Within the universe, conditions that can sustain persistent nuclear fusion occur at the core of stars, facilitated by the gravitational force that entrains and compresses the (fusing) star matter. The synthesis of elements by nuclear fusion also occurs in more dynamic, transient astrophysical events such as supernovae core-collapse [7], and neutron star mergers [8]. Here on Earth, nuclear fusion occurs–if we neglect thermonuclear weaponry tests–in laboratory fusion energy experiments. Work in this area focuses on the merger of deuterium and tritium (isotopes of hydrogen), which is easiest [9]. If this fusion reaction can be controlled and sustained, the released energy could be harnessed to produce electric power from the burning fusion "fuel". Largely, the field of fusion research is composed of two approaches in the attempt to produce conditions to sustain nuclear fusion: magnetic confinement fusion (MCF), and inertial confinement fusion (ICF). In the ICF concept, the confinement and heating of deuterium-tritium to the conditions necessary for fusion is

driven by the fuel's mass inertia. A number of ICF approaches exist, reliant on either lasers [10] or–perhaps a little confusingly–on magnetic fields [11] to generate the pressures necessary to accelerate and compress the fusion fuel over typically a few nanoseconds. An example of magnetic ICF is the pulsed Z-pinch, where an axial current generates an azimuthal magnetic field and radially inward force that impulsively compresses a cylinder of fusion fuel[12]. This is in contrast to magnetic confinement fusion approaches such as tokamak devices, where the electromagnetic force instead confines and heats the fusion fuel for hundreds of seconds [13]. Furthermore, there exist magneto-inertial fusion approaches that combine the compressional heating of ICF with the confinement of heat-carrying particles from MCF in designs that operate on the timescale of hundreds of nanoseconds to microseconds [14][15]. However the work in this dissertation is most relevant to laser ICF. There are a number of laser ICF schemes, but the two main approaches are laser direct-drive and laser indirect-drive, which are shown in Figure 1.2.

In direct-drive ICF, a spherical capsule is directly irradiated by overlapping laser beams [17]. The spherical capsule is a hollow sphere, composed of an outer shell of ablator material such as plastic, beryllium, or high-density carbon, followed by an internal shell layer of cryogenically frozen deuterium-tritium fuel. The irradiating lasers are absorbed on the outer shell surface, ablating the ablator and generating high temperatures and pressures on the capsule exterior. By modulating the laser pulse shape, a series of shocks are launched through the capsule, compressing and accelerating the shell inwards until it stagnates, forming a hot spot with densities of $\sim 10^2$ g/cm^3 and temperatures of hundreds of millions of degrees Kelvin. In the indirect-drive ICF [18] approach, the fuel capsule is also shock compressed. However as the name suggests, the irradiating lasers do not directly implode the fuel capsule. Instead, the fuel capsule is placed inside a hollow cylinder called a *hohlraum*, whose inner walls are composed of a high-Z material such as gold. Lasers enter the hohlraum

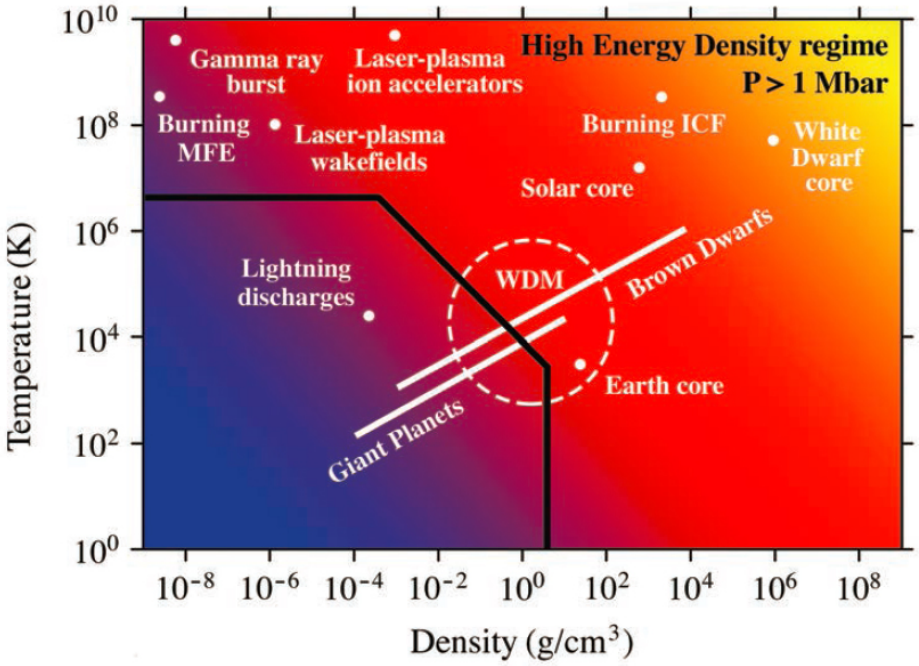

Figure 1.1: The regimes of high-energy-density (HED) plasmas. In the the map, warmer colors correspond to higher pressures and cooler colors to lower pressures. The black line outlines pressures of approximately 1 Mbar, demarcating HED and non-HED regimes. *Reproduced with permission.* (Figure taken from National Academy of Sciences report on Plasma Science, 2021) [16]

from the open ends and irradiate the gold walls. As the gold heats, it re-radiates the absorbed laser energy as X-rays, producing a uniform, hot radiation bath inside the hohlraum, which heats and compresses the fuel capsule.

Globally, a plethora of universities, institutions, and facilities engage in experiments studying the physics of laser inertial confinement fusion. However, this list narrows to a select few facilities–and experiments–which can actually produce significant fusion energy yields. Internationally, experiments are performed on the Laser Mégajoule (LMJ) at the Commissariat à l'Énergie Atomique (CEA) near Bordeaux, France [20], on the GEKKO XII laser at the Institute for Laser Engineering (ILE) of Osaka University in Osaka, Japan [21], on the ISKRA-5 laser in Russia [22], and on the ShenGuang(DivineLight)-III laser facility at the Laser Fusion Research Center (RCLF) of the China Academy of Engineering Physics (CAEP) in Sichuan, China

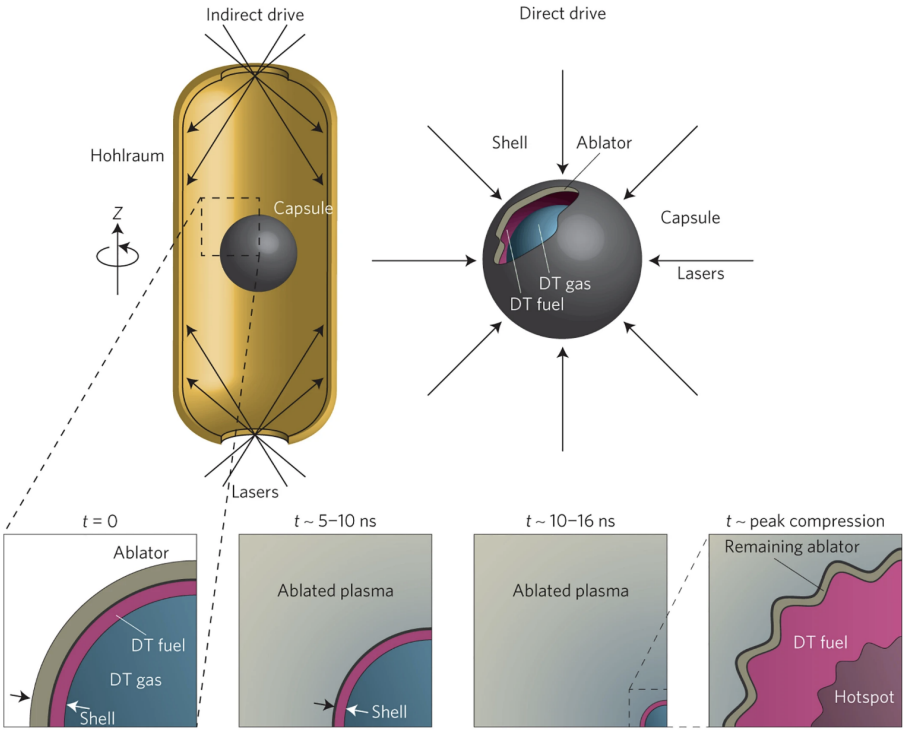

Figure 1.2: Schematic of direct-drive (right) and indirect-drive (left) inertial confinement fusion schemes. The first three panels at the bottom show cross-sections of the capsule at different stages of the capsule compression: first during ablation and shocking, then during capsule compression, and finally at minimum radius during stagnation. The final panel shows a closer cross-sectional view of the capsule at stagnation. This process is largely similar between the direct and indirect-drive confinement fusion approaches. *Reproduced with permission.* (Figure taken from Inertial Fusion with Lasers by R. Betti and O.A. Hurricane) [19]

[23]. In the United States, laser-driven ICF experiments are performed on two facilities: the National Ignition Facility (NIF) [24] at Lawrence Livermore National Laboratory, and the OMEGA laser [25] in the Omega Laser Facility at the Laboratory for Laser Energetics of the University of Rochester. The NIF is a megajoule-class laser facility that can (nominally) produce 1.8 MJ of 3ω frequency laser energy from 192 Neodynium:glass (Nd:Glass) lasers. The beams are oriented such that they enter the facility's target chamber from the North-South in four cones–two inner and two outer–at angles of 23°, 30°, 44°, and 50° with respect to the vertical axis. Indirect-drive experiments are performed on the NIF, heating the interior hohlraum walls

with laser energy over tens of nanoseconds, with laser irradiances ranging from 10^{14} W/cm^2 to a few times 10^{15} W/cm^2 [26][18]. Direct-drive ICF experiments are also performed on the NIF in a polar direct-drive configuration [27][28]. Otherwise, the majority of direct-drive ICF experiments are performed on the OMEGA laser, which features 60 uniformly spherically distributed beams that produce 30 kJ of 3ω laser light. This energy is delivered over about one nanosecond to a fusion capsule, resulting in comparable laser intensities of $10^{14} - 10^{15}$ W/cm^2 to ICF experiments on the NIF.

In 1955, John D. Lawson [29] identified the minimum required confinement conditions for sustained nuclear fusion from energy balance calculations, now referred to as the Lawson criterion. This criterion is related to a (semi-)steady state power gain product known as the *Lawson parameter*, defined as $n\tau_e$ where n is the fuel density and τ_e is the fuel confinement time. Alternative forms are more commonly used for present laboratory fusion efforts. For example, MCF schemes use the *fusion triple product*, defined as $nT\tau_e$ [9] where T is the fuel temperature. And for ICF schemes, "p-tau", defined as $p\tau_E$ where p is the fuel pressure [19], is used. Both of these products have the same physical dimensions (m^{-3} keV s) and, so, are analogous. From the perspective of achieving successful ignition of the fusion fuel, these parameters must exceed a threshold (i.e., the Lawson criterion) to sustain continuous nuclear "burn". In other words, in a successful fusion design the fuel must be contained at sufficiently extreme conditions (in temperature-density or pressure) for a sufficient amount of time.

Furthermore, the Lawson parameter is useful as a unifying metric for evaluating and comparing different fusion approaches. Figure 1.3 shows the experimentally inferred $n_i T_i \tau_e$ triple products from various fusion facilities utilizing laser ICF, magnetic ICF, or MCF approaches. Additionally, predicted triple products from two yet to be completed tokamak facilities, the International Thermonuclear Experimental Reactor

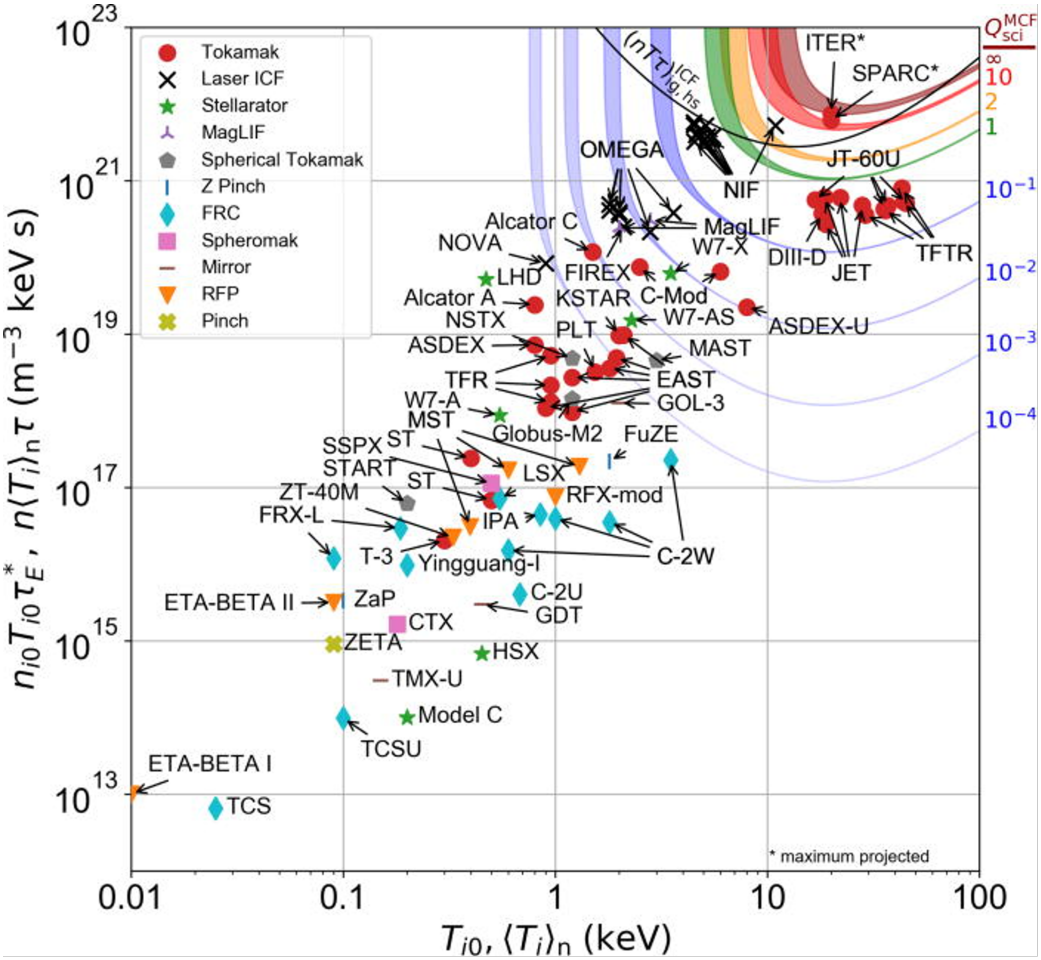

Figure 1.3: Experimentally inferred peak triple products of fusion experiments versus fuel ion temperature [32]. The colored lines indicate contours for values of Q_{sci}^{MCF}, the scientific gain ratio of produced fusion energy versus externally applied power. The black curve indicates the Lawson parameters required to achieve hot-spot ignition from ICF approaches. *Reproduced with permission.*

(ITER) in France [30], and the Soonest/Smallest Possible Affordable, Robust, Compact (SPARC) fusion reactor at the Massachusetts Institute of Technology (MIT) Plasma Science and Fusion Center (PSFC) [31], are also shown in this figure. Ignoring these speculative data points, laser ICF indirect-drive experiments on the NIF have achieved the highest triple product values and correspondingly highest fusion yields within the laboratory fusion landscape.

And now–in 2023–is an exciting time in the field of inertial fusion research. On the NIF, on August 8th, 2021 an experiment produced 1.35 MJ of fusion energy from

1.9 MJ of laser energy, which was the first evidence of controlled laboratory fusion beyond ignition [33][34][35] and approximately eightfold increase in gain over previous experiments[36]. In Figure 1.3 the triple product for this experiment, referred to as shot N210808, is indicated by the most North-East black x symbol. Then, on December 5th, 2022, an experiment with 2.05 MJ input laser energy produced 3.15 MJ of fusion energy [37], producing the first net energy gain from fusion reactions. And in July of 2023, that experiment was repeated and produced 3.88 MJ of fusion energy [38]. Naturally, the goal is to move beyond even such landmark achievements. However, extending research in ICF modeling requires advancing from the current parameter space of experimental and modeling data with more predictive simulations. As an integrated ICF experiment is a complex, multi-physics environment, the development of this enhanced predictive simulation framework requires a sufficiently accurate description of these various physical processes.

1.1.1 The Equations of Radiation Hydrodynamics

Presently, the standard approach for computational simulations of integrated ICF experiments utilizes a fluid approximation, coupled with models for the other important physical processes that exist in ICF systems. Figure 1.4 provides a schematic of various physical processes relevant to ICF experiments within HYDRA, a multi-physics ICF code developed at the Lawrence Livermore National Laboratory [39]. At the core of this computational modeling effort of ICF experiments are the equations of radiation-hydrodynamics [3]. Assuming the continuum approximation is valid, that viscous effects are negligible and that there are no magnetic fields, these equations

describe the conservation of mass, momentum, and energy:

$$\frac{\partial \rho}{\partial t} + \nabla \cdot (\rho \boldsymbol{u}) = 0, \tag{1.1}$$

$$\frac{\partial \rho \boldsymbol{u}}{\partial t} + \nabla \cdot [\rho \boldsymbol{u}\boldsymbol{u} + \boldsymbol{I}(p_i + p_e + p_R)] = 0, \tag{1.2}$$

$$\frac{\partial E_T}{\partial t} + \nabla \cdot [(E_T + p_e + p_i + p_R)\boldsymbol{u})] = -\nabla \cdot (\boldsymbol{Q_e} + \boldsymbol{F_R}) + \boldsymbol{S_L}, \tag{1.3}$$

where ρ is the fluid density, $\boldsymbol{u}$ is the velocity vector, and p_i, p_e, and p_R are the ionic, electric, and radiative contributions to the fluid pressure, respectively. In radiation-hydrodynamics modeling the fluid density, ρ, only considers the ion mass and ignores the mass of electrons, which are ≈ 1836 times less massive than protons. $\boldsymbol{Q_e}$ is the electron heat flux and $\boldsymbol{F_R}$ is the radiation heat flux, and $\boldsymbol{S_L}$ is an external source term representing laser heating. The ion species can also transport heat, however this is not considered in the equations of radiation-hydrodynamics because ions have smaller velocities at the same temperature (or mean kinetic energy), so the heat flux is smaller by factor $\sim \sqrt{m_i/m_e}$ where m_i and m_e are the ion and electron masses. $E_T =$ is the total energy, defined as

$$E_T = E_i + E_e + E_R + \frac{1}{2}\rho \boldsymbol{u}\boldsymbol{u}, \tag{1.4}$$

or as the sum of the internal energy contributions of ions, electrons, the radiation field, and the ion kinetic energy. In high-energy-density plasmas, it is not uncommon for the separate species that compose the plasma to have different temperatures ($T_e \neq T_i \neq T_R$) due to discrepancies between the rate of energy transport within each species and the rate of energy transport between various species. This is equivalent to disparate energy densities for each species, which necessitates separating Equation

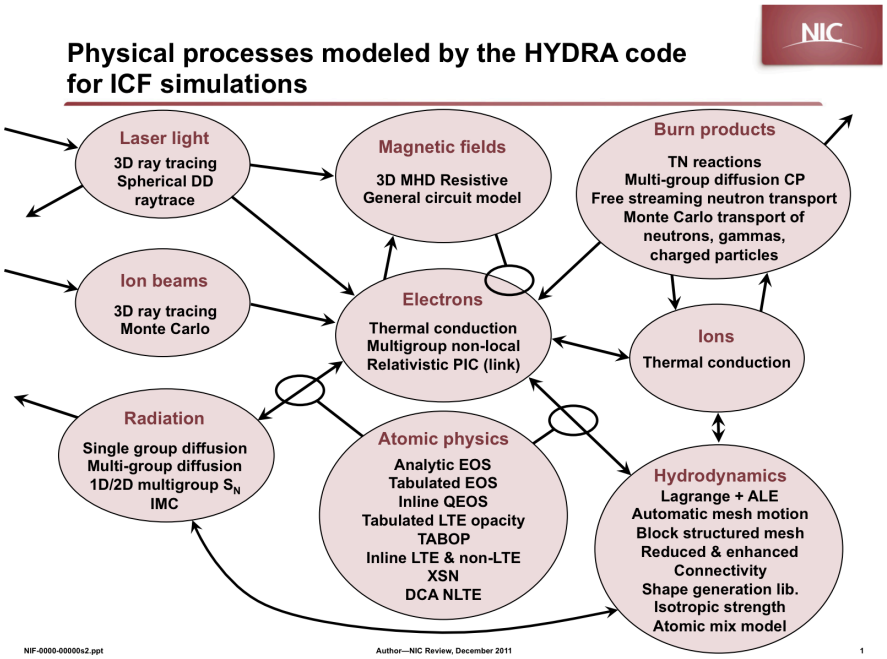

Figure 1.4: Schematic of important physics present within the HYDRA radiation-hydrodynamics ICF code [39]. *Reproduced with permission.*

1.3 into three energy equations:

$$\frac{\partial E_i}{\partial t} + \nabla \cdot (E_i \boldsymbol{u}) + p_i \nabla \cdot \boldsymbol{u} = \frac{N k_B}{\tau_{ie}}(T_e - T_i), \tag{1.5}$$

$$\frac{\partial E_e}{\partial t} + \nabla \cdot (E_e \boldsymbol{u}) + p_e \nabla \cdot \boldsymbol{u} = -\nabla \cdot \boldsymbol{Q_e} + \frac{N k_B}{\tau_{ie}}(T_i - T_e) + c(\kappa_P E_R - \kappa_E B_e) + \boldsymbol{S_L}, \tag{1.6}$$

$$\frac{\partial E_R}{\partial t} + \nabla \cdot (E_R \boldsymbol{u}) + p_R \nabla \cdot \boldsymbol{u} = -\nabla \cdot \boldsymbol{F_R} - c(\kappa_P E_R - \kappa_E B_e), \tag{1.7}$$

where here coupling terms facilitate the energy exchange between the different plasma components. Energy exchange between the electrons and ions occurs through Coulomb collisions, represented with coupling coefficient $N k_B/\tau_{ei}$ where N is the total particle number density, k_B is the Boltzmann constant, and τ_{ei} is the electron-ion relaxation time. The radiation field exchanges energy with the electrons via both absorption and emission, where κ_P is the Planck opacity, κ_E is the absorption opacity, c is the speed of

light, $B_e = a_R T_e^4$ is the blackbody (Planckian) energy density, $a_R = 4\sigma/c$ is the radiation constant, and σ is the Stefan-Boltzmann constant. For convenience, these radiation transport and energy exchange terms are written integrated through the radiation spectrum, but typically radiation transport approaches use a multi-group approach to preserve the frequency-specific details of the radiation field [6]. Here, an equation of state (EOS) is necessary to establish a closure relation between the fluid pressure and internal energy. The simplest approach would be to assume an ideal gas formulation, with pressure-temperature relation $p_e + p_i = [\rho k_B T_e/(Am_p) + \rho Z k_B T_i/(Am_p)]$ and $E_e + E_i = (p_e + p_i)/(\gamma - 1)$ where k_B is the Boltzmann constant, A is the atomic number, m_p is the proton mass, Z is the average ionization, and $\gamma = c_P/c_V$ is the adiabatic index. But more sophisticated equations of state consider additional effects such as Coulomb interactions, electron degeneracy, and pressure ionization, to name a few, and are also applicable across different phases of matter (e.g. solid, liquid). And so in practice, tabulated equations of states are used in ICF simulations. Some examples of commonly used tables are the SESAME tables from Los Alamos National Laboratory [40], PrOpacEOS tables from PrismSPECT [41], and LEOS tables from Lawrence Livermore National Laboratory [42].

1.1.2 The Laser-Plasma Ablation Front

Consider the interaction of a laser with a solid material. As the laser propagates through the matter, energy is absorbed into free electrons, up until the laser frequency ω equals the electron plasma frequency ω_{pe}, after which the electrons resonate with the light wave[43]. Equivalently, for a laser of coherent frequency there is a critical density n_c beyond which the laser light does not propagate into higher density material. For 3ω lasers on the NIF and OMEGA, $n_c \sim 9 \times 10^{21}$ cm^{-3}. For fully ionized beryllium ($Z = 4$), this corresponds to mass density $\rho \sim 0.03$ g/cm^3 or below solid density. In such a situation, the material is asymmetrically heated to a plasma state on the

laser-side surface. The pressure generated by the laser-heating expands the heated plasma away from the free-surface and simultaneously drives a shock that compresses and accelerates the denser material. The resulting structure is a laser-plasma ablation front, a key progenitor of direct-drive and indirect-drive ICF systems. Accordingly, it is useful to consider challenges in modeling physical processes associated with ICF experiments in the context of laser-ablation fronts.

Figure 1.5 shows a profile of a laser-ablation front, taken from a 1D-spherical HYDRA radiation-hydrodynamics simulation of a copper ($Z = 29$) sphere illuminated with laser irradiance 10^{15} W/cm^2. Here, the laser propagates directionally from far radii towards the origin, through the ablated plasma up the density gradient until it reaches the critical density n_c at approximately $r = 470$ μm. At these laser intensities, the most efficient laser energy deposition mechanism is the collisional inverse bremsstrahlung (IB) [43] absorption process, which can describe the energy deposition from $\boldsymbol{S_L}$ in Equation 1.6 to the electron internal energy, E_e. However, ICF laser intensities and plasma conditions can exceed thresholds necessary for significant contributions from other laser-plasma interactions (LPI) that complicate the laser description. Generally, these LPI effects modify how energy is deposited into the plasma. More specifically, LPI affects the total energy deposition from the laser, affects where energy is deposited in the plasma, and generates high energy electrons.

In the underdense plasma where the laser deposits energy, the ion, electron and radiation temperatures diverge. In this region, the plasma departs from local thermodynamic equilibrium (LTE) conditions and is NLTE. In LTE conditions, the plasma ionization distributions can be calculated with the Saha equation (i.e. Boltzmann statistics) as functions of the local density and temperature, which can then be used to calculate absorption and emission opacities. However in NLTE regions it is necessary to consider the effect of both the plasma properties (ρ, T) and the radiation field (T_R) on the atomic charge distributions. Consequently, the atomic kinetics are calcu-

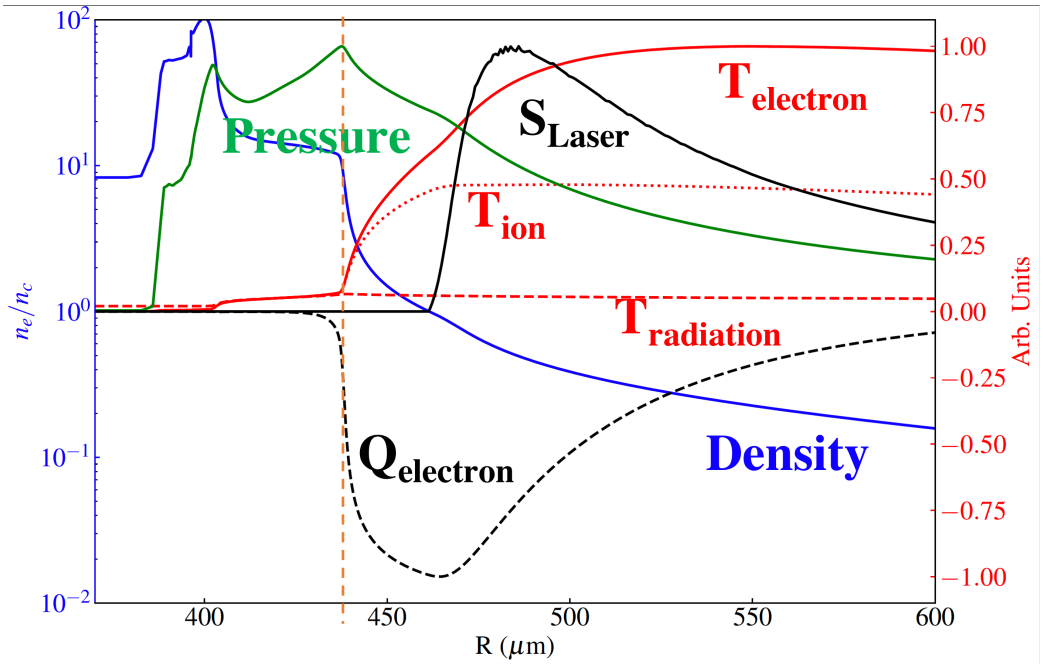

Figure 1.5: 1D profile of laser-ablation front from a 1D-spherical HYDRA radiation-hydrodynamics simulation. The laser is propagating from right-to-left towards the origin. The dashed-orange vertical line demarcates the local thermodynamic equilibrium (LTE) and nLTE portions of the plasma.

lated by employing a collision-radiative model, consisting of a series of rate equations for each population state that incorporates descriptions of various processes through which electrons and photons interact with ions. This is highly challenging as the number of electron energy states and their transitions increases orders of magnitude with Z (which increases computational expense) [44]. Collision-radiative approaches are necessary to calculate appropriate plasma ionizations, absorption and emission opacities, as well as EOS [45] in NLTE conditions.

At densities greater than n_c, the laser $\boldsymbol{S_L}$ does not deposit energy, and instead energy is transported into the denser plasma via electron heat and radiative transport. In Figure 1.5, one can see that there exists a double humped temperature and density profile, known as a double-ablation front [46]. This emerges because of the delineation of dominant energy transport mechanisms in different parts of the plasma. In the denser part of the plasma, the radiation transport from the plasma self-emission

dominates, whereas in the less dense plasma up to n_c, electron thermal transport dominates.

In the context of the laser-ablation front, the indirect- and direct-drive approaches aim to preferentially convert the absorbed laser energy into radiation energy or into hydrodynamic (kinetic) energy, respectively. For the indirect-drive approach, a higher atomic number (Z) element is chosen for the hohlraum wall material in order to more efficiently convert the laser energy into plasma internal energy, coupled with a thicker layer of material (towards the semi-infinite wall limit) to minimize kinetic energy from hydrodynamic motion. For direct-drive, a thin layer of low-Z material is chosen, such that the laser energy generates large ablation pressures ~ 100 MBar on the capsule surface, which shocks and accelerates the fuel capsuke. Integral to both approaches is electron heat transport, which is the mechanism for both heating the radiative material, or increasing the material pressure beyond n_c in order to drive shock acceleration. Electron transport models, which are the focus of this dissertation, are therefore critical to studies of laser-plasmas and of ICF.

1.2 Classical Electron Thermal Transport

The work in this dissertation focuses on electron thermal transport, so a detailed overview is given here. In the microscopic view of a plasma, heat is carried by electrons at the rate $(\frac{1}{2}m_e v_e^2) \times v_e$ where the parenthetical term here represents the electron particle kinetic energy, m_e is the electron mass, and v_e is the electron velocity. From the macroscopic fluid perspective, electron thermal transport–in its simplest form–is represented by Fick's Law:

$$\mathbf{Q_e} = -\kappa \nabla T, \tag{1.8}$$

where heat flows diffusively, proportional to the material thermal conductivity κ and to the temperature gradient ∇T. This behavior is described with Fick's Law as

opposed to Fourier's Law because fundamentally the heat flux emerges from carried by the transport of electrons (particles) with thermal energy. For plasmas, when the thermal conductivity κ and thus $\mathbf{Q_e}$ are solely dependent only upon local conditions at $\boldsymbol{x}$, this process is referred to as *classical* electron transport. While a local description for electron transport is very useful, such an expression for electron heat transport is not necessarily justifiable because of the emergence of steep temperature gradients in laser-plasmas at conditions relevant to ICF, and so its limits must be considered. To do so, we begin with the Boltzmann transport equation for particle species s:

$$\frac{\partial f_s}{\partial t} + \boldsymbol{v} \cdot \nabla f_s + \frac{\boldsymbol{F}}{m_s} \nabla_v f_s = \left(\frac{\partial f_s}{\partial t} \right)_C , \tag{1.9}$$

where $f_s = f_s(\boldsymbol{x}, \boldsymbol{v}, t)$ is the velocity distribution function in units of particle number density at position $\boldsymbol{x}$ and time t with velocity $\boldsymbol{v}$, m_s is the particle mass, $\boldsymbol{F}$ represents all forces acting on the particle, and the expression on the right-hand side describes the rate of change of f_s from binary collisions. One can think of the Boltzmann equation as a continuity equation in seven dimensions that describes the evolution of the number of particles at a given position and velocity $(\boldsymbol{x}, \boldsymbol{v})$ subject to the net flux of particles with velocity $\boldsymbol{v}$ into that position, the flux of particles at $\boldsymbol{x}$ accelerated by the force $\boldsymbol{F}$ to velocity $\boldsymbol{v}$, and finally the net production of particles at $(\boldsymbol{x}, \boldsymbol{v})$ by collisions via the right-hand side. If the considered species are the free electrons ($s = e$) within a plasma, the dominant force is the Lorentz force $\boldsymbol{F_L} = q(\boldsymbol{E} + \boldsymbol{v} \times \boldsymbol{B})$ where q is the electronic charge, $\boldsymbol{E}$ is the electric field, and $\boldsymbol{B}$ is the magnetic field. A further assumption of a collisionless plasma reduces Equation 1.9 to the Vlasov equation. But if rather one assumes that the effect of collisions is retained and dominated by Coulomb interactions, one yields the kinetic Vlasov-Fokker-Planck (VFP) equation:

$$\frac{\partial f_s}{\partial t} + \boldsymbol{v} \cdot \nabla f_s + \frac{q_s}{m_s} \left(\boldsymbol{E} + \boldsymbol{v} \times \boldsymbol{B} \right) \nabla_v \cdot f_s = C_s(f_s), \tag{1.10}$$

where here the right-hand collision operator $C_s(f_s)$ describes the effect of inter- and intra-species particle collisions between electrons and ions in a plasma in aggregate as opposed to binary collisions in the case of the Boltzmann equation. This operator can be represented with various formulations, but typically consists of terms representing electron-ion and electron-electron collisions $C_s = C_{ei} + C_{ee}$, and principally shifts f_s towards the Maxwell-Boltzmann distribution, $f_{s,MB}(v) = \left(\frac{m_s}{2\pi k_B T_s}\right)^{3/2} \mathrm{e}^{-\frac{m_s v^2}{2k_B T_s}}$, where k_B is the Boltzmann constant and T_s is the thermodynamic temperature, and $v = |\boldsymbol{v}|$.

In principle, a kinetic computational approach using the Vlasov-Fokker-Planck equation could be used to model an ICF system, providing the advantage of considering non-Maxwellian (or non-fluid) effects in the plasma. However, kinetic approaches face significant challenges with respect to radiation-hydrodynamics modeling for ICF simulations. Present ICF experiments are on timescales of the order of tens of nanoseconds (10^{-8} s) and spatial scales up to millimeters (10^{-3} m), while kinetic timescales are on the order of the electron-ion collision timescale $\nu_{ei}^{-1} \sim 10^{-16}$ s for ICF implosions, and spatial scales on the order of the electron inertial length $\sim 10^{-9}$ m at solid densities [47]. Furthermore, kinetic simulations must be discretized in velocity space, which adds both additional computational cost and increased storage requirements from the increased dimensionality. For specific ICF concepts like fast ignition [48] and shock ignition [49], kinetic effects are important, and VFP studies have been performed to study the latter [50]. But for typical ICF modeling, it is preferable to supersede a kinetic representation for electrons by assuming they follow a Maxwell-Boltzmann distribution. This leads to a fairly straightforward connection from f_e to n_e, T_e as the zero and second velocity moments of f_e respectively. However, calculating the heat flux $\boldsymbol{Q_e}$, or third velocity moment of f_e, requires a little more work.

1.2.1 Spitzer-Harm Thermal Conduction

With the appropriate assumptions, the kinetic equations can be solved and integrated across velocity space to yield an analytic expression for the heat flux $\boldsymbol{Q_e}$. This is the case for Spitzer-Harm theory [5], which is derived from the VFP equations for a nearly uniform, unmagnetized ($\boldsymbol{B} = 0$) plasma, constant in density (n_e), and slowly varying in electron temperature (T_e) in the x-direction. In the diffusion limit, the kinetic modeling of the electron distribution can be approximated by $f = f_0 + f_1$ where f_0 is isotropic, and f_1 is a small, anisotropic perturbation. Here specifically, it is assumed that f is defined up to first-order as

$$f(v) = f_0(v) + f_1(v)\cos\theta, \tag{1.11}$$

where $f_0(v)$ is the Maxwell-Boltzmann distribution, and $f_1(v)cos\theta$ is the first-order perturbation to f. The polar angle θ is defined with respect to the direction x of the temperature gradient. Intuitively, this can be viewed as a Legendre expansion of the electron distribution function up to the first harmonic, with first-order corrections to the symmetric zeroth-order function (the Maxwelllian) from f_1 largest when considering positions parallel to x, e.g., in the direction of the temperature gradient. Like any other linear expansion, this definition for f is valid provided the truncation at first-order is justified, or $f_0(v) \gg f_1(v)$. We note that in the calculation of the heat flux $\mathbf{Q_e}$ the contribution of f_0 does not generate any heat transport since it is symmetric; the electron heat flux therefore emerges from the third-order velocity moment of f_1.

Next it is assumed that electron-ion collisions dominate. In this limit where electron-electron collisions are negligible, and Shkarofsky et al. [4] show that the

electron-ion collision term then reduces to a simple relaxation rate of

$$C_{ei}(f) = -\left(\frac{n_i Y}{v^3}\right)(f - f_0) = -\left(\frac{n_i Y}{v^3}\right) f_1 \cos\theta, \tag{1.12}$$

where n_i is the ion density, $Y = 4\pi(Ze^2/m_e)^2 \ln\Lambda$, Z is the average ionization of the plasma, e is the electric charge, m_e is the electron mass, and $\ln\Lambda = \frac{1}{2}\ln(1+b_{max}^2/b_{min}^2)$ is the Coulomb logarithm, and $b_{min,max}$ are cutoff limits on the impact parameter for Coulomb scattering. The maximum impact parameter b_{max} is defined as the Debye-Huckel screening length $\lambda_{DH} = \sqrt{\frac{k_B T_e}{4\pi n_e e^2}}$. Using this approximation for the collision-operator as well as the form of the EDF given in Equation 1.11 substituted into Equation 1.10, and keeping terms proportional to $\cos\theta$, yields

$$\frac{\partial f_1}{\partial t} + v\frac{\partial f_0}{\partial x} - \frac{eE}{m_e}\frac{\partial f_0}{\partial v} = -\frac{-n_i Y}{v^3} f_1. \tag{1.13}$$

Assuming steady-state conditions ($\cancelto{0}{\frac{\partial f_1}{\partial t}}$), Equation 1.13 can be rearranged for f_1:

$$f_1 = -\frac{v^3}{n_i Y}\left(v\frac{\partial f_0}{\partial x} - \frac{eE}{m_e}\frac{\partial f_0}{\partial v}\right), \tag{1.14}$$

where f_1 is defined proportional to derivatives of the Maxwell-Boltzmann distribution f_0 and the electric field E. Finally, it is assumed that in the steady-state the electron velocity distribution induces zero net-current despite the flow of heat-carrying electrons in x, or $J_x = -e\int v_x f(\boldsymbol{v}) d\boldsymbol{v} = 0$. Similar to the the electron heat flux, the current J_x only depends upon f_1, which yields

$$\int v^3 f_1(v) dv = \int v^6 \left(v\frac{\partial f_0}{\partial x} - \frac{eE}{m_e}\frac{\partial f_0}{\partial v}\right) dv = 0, \tag{1.15}$$

within the integral. This expression can be rearranged to define the electric field as

$$eE = -m_e \frac{\int \frac{\partial f_0}{\partial x} v^7 dv}{6 \int f_0 v^5 dv}, \tag{1.16}$$

yielding the Spitzer electric field $eE = -k_B T_e(\frac{1}{n_e}\frac{\partial n_e}{\partial x} + \frac{5}{2}\frac{1}{T_e}\frac{\partial T_e}{\partial x})$ or simply $eE = -\frac{5}{2}\frac{\partial k_B T_e}{\partial x}$ assuming negligible (electron) density gradients. Penultimately, substituting this expression of eE into Equation 1.14 as well as the appropriate derivatives of f_0, $\partial f_0/\partial x$ and $\partial f_0/\partial v$, yields the fully defined first-order anisotropy of the electron velocity distribution function as

$$f_1 = f_0 \frac{v^4}{2 n_i Y k_B T_e} \left[8 - \frac{m_e v^2}{k_B T_e}\right] \frac{\partial k_B T_e}{\partial x}. \tag{1.17}$$

The directional heat flux along x is defined as

$$Q = \int \left(\frac{1}{2} m_e v^2\right) v \cos\theta f_1 \cos\theta d^3 v. \tag{1.18}$$

Here, all that is required is the substitution of f_1 with the definition given in Equation 1.17 and then fully integrating in v. Ultimately, this yields the Spitzer-Harm heat flux:

$$Q_{SH} = \frac{16\sqrt{2}}{\pi^{3/2}} \frac{(k_B T_e)^{5/2}}{Z e^4 m_e^{1/2} \ln\Lambda} \frac{\partial k_B T_e}{\partial x} = -\kappa_{SH} \frac{\partial k_B T_e}{\partial x}. \tag{1.19}$$

This analytic expression of the heat flux follows Fick's Law in Equation 1.8, with the gradient term $\nabla \cdot (k_B T_e)$ is given in terms of electron energy $k_B T_e$ instead of electron temperature, and the conductivity κ_e is defined with respect to fluid quantities. The thermal conductivity κ_{SH} scales with the plasma temperature $T_e^{5/2}$. This is consistent with analytical thermal conductivities calculated by Chapman and Cowling from the Boltzmann equation [51], which is more generally defined as $\kappa_{th} \propto T^s$, where $s = \frac{1}{2} + \frac{2}{\nu - 1}$ and ν is dependent upon the behavior of the dominant/aggregate repelling force between molecules $F/r^{-\nu}$. For an ideal gas (i.e., a neutral gas) there is no field

force. Instead inter-particle interactions are dominated by elastic collisions such that $\nu \to \infty$ and $s = 1/2$. For HED plasmas the electrostatic force is dominant, which behaves in accordance to the inverse-square law F/r^2, predicting the $s = 5/2$ scaling characteristic of Spitzer-Harm theory. At first glance, it appears that the heat flux is independent of density n_e (which is also predicted by Chapman and Cowling [51]). Physically, this can be interpreted as a perfect balance between the increase in heat-carrying particles and decrease in particle characteristic mean-free-path as density increases. However upon closer inspection it is evident that density effects on the thermal conductivity κ_{SH} are extant within the definition of the Coulomb logarithm, lnΛ. The electron temperature also affects ln Λ; however this influence is small compared to the power-law scaling of κ_{SH} with T_e.

For the derivation of classical heat flux, the assumption of a simple-relaxation collision-operator following Shkarofsky et al. [4] neglects the effect of electron-electron collisions. This effect–particularly for lower-Z plasmas–cannot be realistically discounted. To assess the Spitzer-Harm model, the analytical Spitzer conductivities were compared with kinetics simulations that do indeed include electron-electron collisions [52]. These kinetic calculations numerically solve the VFP equations for f from a uniform (Z, n_e) plasma with small temperature gradient, and then numerically integrate the third velocity-moment of f to yield thermal conductivities. From these studies it is found that Spitzer conductivities agree very well with kinetic conductivities accounting for electron-electron collisions, provided the introduction of an analytic Z-dependent correction factor, the expression of which is determined from fitting to the VFP thermal conductivities. One such form is proposed by Sanmartin et al [53], defined as $g(Z) = Z/(Z + 11/3)$. Another is proposed by Epperlein and Short [52], defined as $\xi(Z) = (Z + 0.24)/(Z + 4.2)$. As shown in Figure 1.6 reproduced from Brodrick et al. [2], both Z-dependent factors are reasonable adjustments for the electron conductivity in comparison with kinetic calculations. For this dissertation, it is

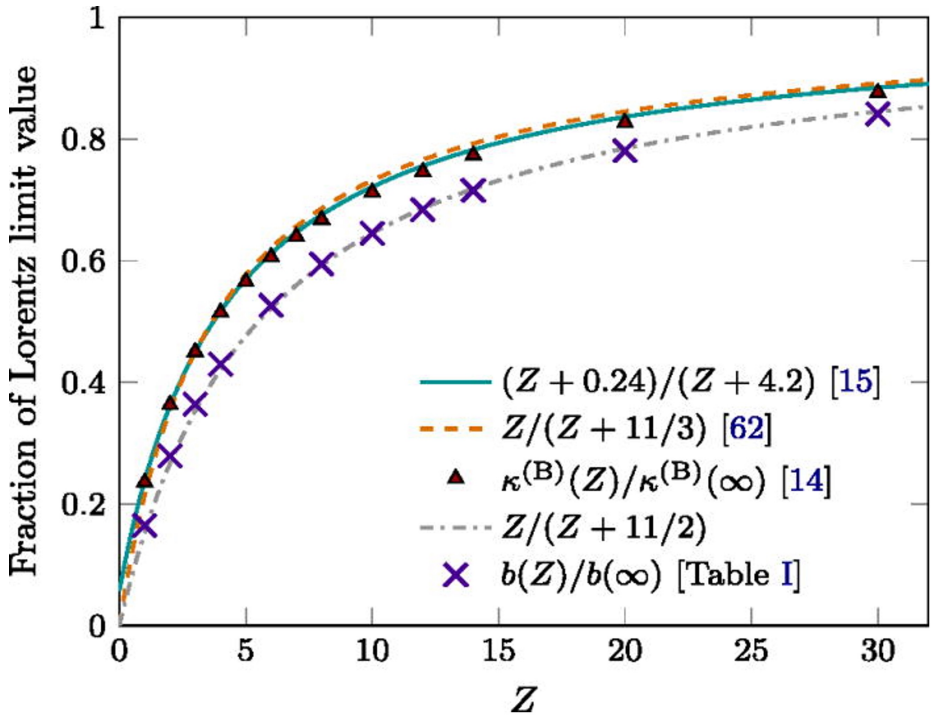

Figure 1.6: Comparison of Z-dependent conductivity factors $\xi(Z) = (Z + 0.24)/(Z + 4.2)$ (green) and $g(Z) = Z/(Z + 11/3)$ compared to numerical calculations (triangles) from Brodrick et al. [2]. *Reproduced with permission.*

noteworthy that the latter term $\xi(Z)$ features prominently in the reduced-order non-local Schurtz-Nicolai-Busquet (SNB) model by Schurtz et al. [1], which is extensively employed in Chapters 2 and 3.

With respect to Spitzer-Harm theory, Lee and More [54] proposed an improved thermal conductivity model for dense plasmas, which employs a definition of ln Λ incorporating the effects of electron degeneracy, ion-ion correlations, and electron neutral scattering in addition to the standard contribution from the Debye-Huckel screening length. Figure 1.7 compares the thermal conductivities of Spitzer-Harm theory with the Lee-More model for aluminum at densities 0.215 g/cm^3 and 2.5 g/cm^3, showing that the Lee-More model predicts conductivities at lower electron temperatures closer to those from numerical calculations, while Spitzer-Harm conductivities are incorrect by a factor of $\mathcal{O}(10)$. At higher temperatures ($T_e > 100$ eV) Spitzer-Harm and Lee-More behave similarly: both predicting nonlinear ($\kappa_{th} \propto T_e^{5/2}$)

heat fluxes solely dependent upon local plasma conditions. However as temperature gradients become large such that the characteristic diffusive length-scale becomes large relative to the temperature length scale, such descriptions for the heat flux prove insufficient.

1.2.1.1 Moments of the f_1 Anisotropy

To understand the limits and consequently the classical expression for the electron heat flux, it is instructive to examine the normalized first-order correction to the Maxwellian EDF, f_1/f_0. Equation 1.17 can be rewritten for f_1/f_0 as

$$\frac{f_1}{f_0} = \frac{1}{\sqrt{2\pi}} \left(8\frac{v^4}{v_{th}^4} - \frac{v^6}{v_{th}^6} \right) \frac{\lambda_{ei}}{L_T}, \tag{1.20}$$

where $\lambda_{ei} = 128\sqrt{2\pi}\frac{(k_B T_e)^2}{n_e e^4 \ln \Lambda}$ is the electron mean-free-path (mfp), $L_T = T_e/|\frac{\partial T_e}{\partial x}|$ is the temperature gradient scale-length, and $v_{th} = \sqrt{k_B T_e/m_e}$ is the electron thermal velocity. The ratio of the heat-carrying electron mfp to the scale-length of the temperature gradient λ_{ei}/L_T is also referred to as the Knudsen number, a dimensionless number that ideally is small ($\lambda_{ei}/L_T \ll 1$) for the diffusion approximation of electron transport to be valid. Figure 1.8 shows the velocity dependence of f_1/f_0, here also normalized by λ_{ei}/L_T, which exhibits a local maxima at $v/v_{th} \sim 2.3$. Intuitively, it appears appropriate to require that $|f_1/f_0| < 0.1$ or similar proportion, as this enforces the "smallness" of f_1, which is required to justify the truncation of the distribution function to first-order within Spitzer-Harm theory. But for most kinetic studies of electron transport, instead it is required that $|f_1/f_0| < 1$. This simply states that the EDFs defined by $f_0 + f_1$ must be physical, because $f_1 > f_0$ suggests the production of negative density populations. At $v/v_{th} = 2.3$, this imposes the limit of $\lambda_{ei}/L_T < 0.033$. However as the electron velocity increases the v^6 dependency of f_1 on f_0 becomes the dominant behavior, and the distribution f_1 becomes increasingly

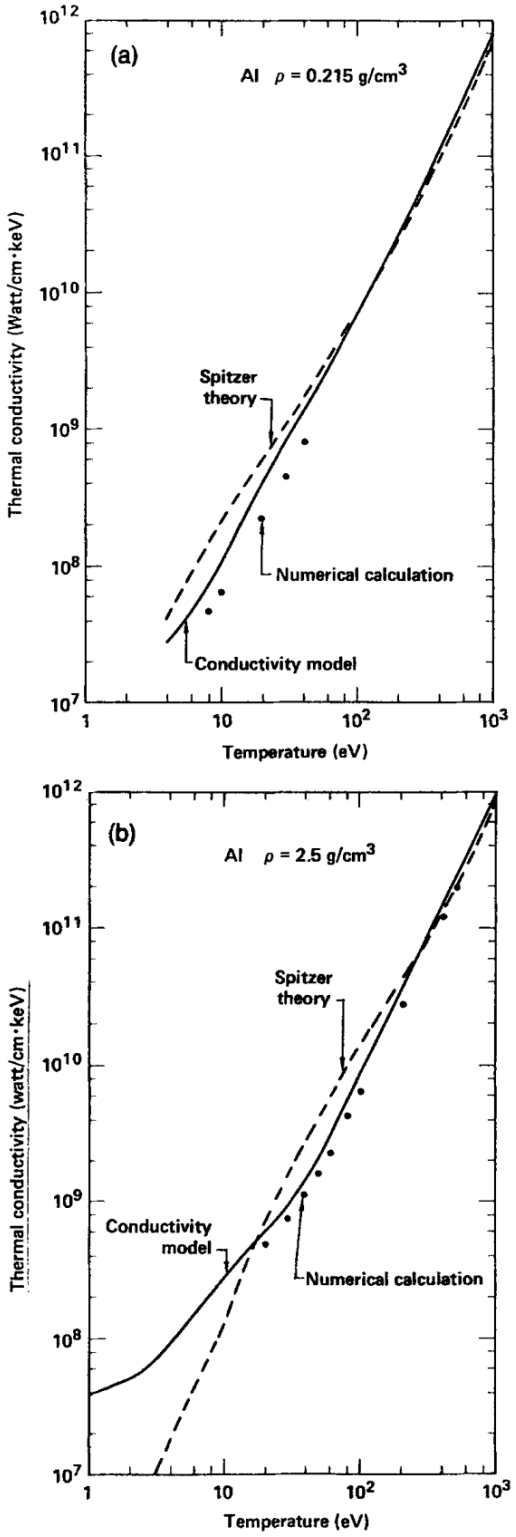

Figure 1.7: Thermal conductivity of aluminum versus the electron temperature for mass densities of (a) 0.215 g/cm^3 and (b) 2.5 g/cm^3. The solid curve here is the electron conductivity model from Lee & More, which improves conductivity predictions to be closer to numerical calculations (circles) compared to Spitzer-Harm theory at lower plasma temperatures. *Reproduced with permission.* [54]

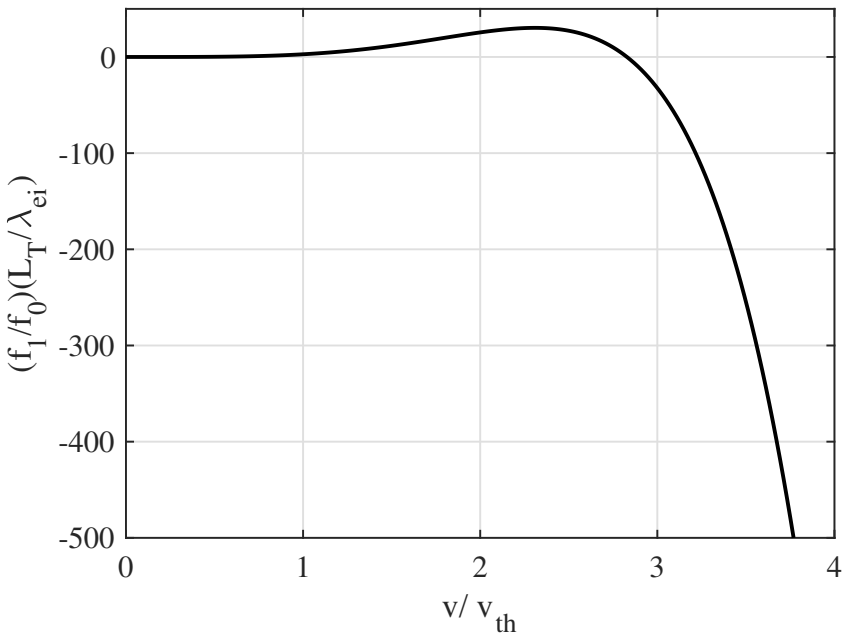

Figure 1.8: The ratio of the first-order perturbation to the Maxwellian and the Knudsen number, $\frac{f_1(v)}{f_0(v)} / \left(\frac{\lambda_{ei}}{L_T}\right)$. At $v/v_{th} = 2.3$ this ratio is ~ 30, and around the maximum contribution of $f_1 v^5$ to the heat flux at $v/v_{th} = 3.7$ this ratio is ~ 420.

negative as v increases. It is evident that no limit on λ_{ei}/L_T prevents this behavior.

Figure 1.9 shows the first-order anisotropy f_1 as well as the first and third velocity moments of f_1, corresponding to the velocity-dependent contribution to the electric current and heat flux respectively. While it was observed in Figure 1.8 that f_1/f_0 becomes largely negative, here it is evident that f_1 is largest at $v_{th} \sim 2$, and has a local minimum after becoming negative at $v_{th} \sim 3.7$. This is because the exponential Maxwell-Boltzmann function for f_0 decreases much more rapidly with velocity than the proportional increase of the first-order perturbation $|f_1/f_0|$.

The first velocity moment reflects the distribution that yields the electric current ($j = e \int v^3 f_1(v) dv$). This has been already integrated over velocity directions perpendicular to the the temperature gradient in x . This distribution satisfies the zero current condition and it is evident that this results from two comparable counter-propagating electric currents. The first current is composed of a larger, slower pop-

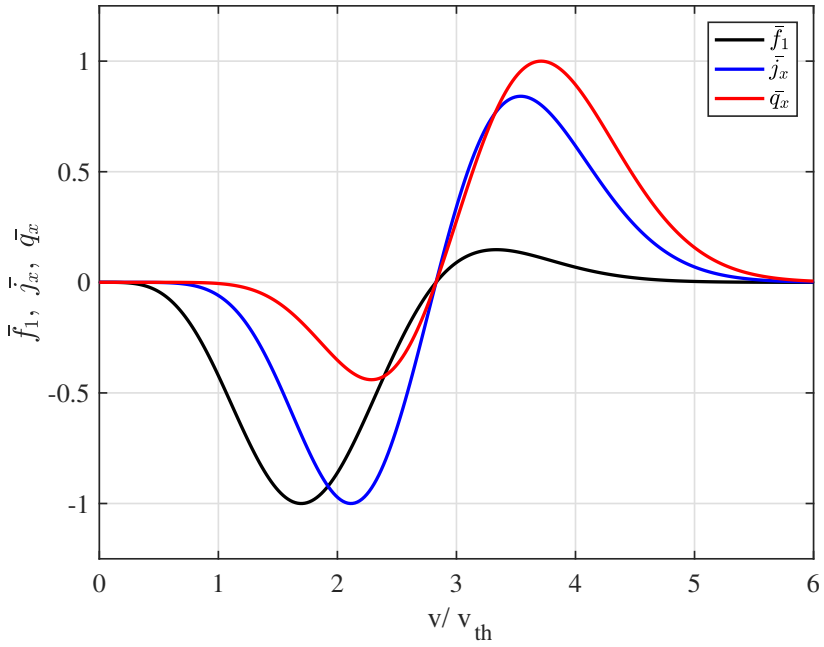

Figure 1.9: The normalized functions here are defined as $\bar{F(v)} = F(v)/\max(|F(v)|)$. Shown are the first-order correction $\bar{f}_1$ (blue) defined from Spitzer-Harm theory from Equation 1.17, the first velocity moment current $\bar{j_x} \sim v^3 f_1$ and the third velocity moment heat flux $\bar{q_x} \sim v^5 f_1$ plotted against the normalized velocity v/v_{th}.

ulation with peak near $v/v_{th} = 2$, balanced by the second electric current produced by a smaller, faster population near the peak at $v/v_{th} = 3.7$. Moving to the third velocity moment which represents the heat flux distribution q_e [also integrated in velocity components perpendicular to the heat flux, and represented as $\sim v^5 f_1(v)$], it is apparent that the higher velocity portion of f_1 gives the largest contribution to the heat flux (again here centered around $v/v_{th} \sim 3.7$), while the lower velocity electrons returns a small portion of the outgoing heat back to the plasma. In accordance with this observed behavior, the lower velocity portion of the anisotropic distribution f_1 is aptly referred to as the cold return current.

From inspecting the third velocity moment, one can surmise that the first-order anisotropy should be small enough so that the derived expression for f_1 is appropriate at electron velocities that contribute greatly to the heat flux distribution, namely for the higher electron velocity population with peak at thermal velocity $v/v_{th} \sim 3.7$.

Revisiting equation 1.20, this requires that $|f_1/f_0| < 1$ at $v/v_{th} = 3.7$, which implies a limit on the Knudsen number of $\lambda_{ei}/L_T < 0.0024$ to prevent f from becoming unphysical at these velocities. The reason this threshold for the Knudsen number is so small is due to the electron mfp λ_{ei} scaling with respect to the plasma temperature and correspondingly with v_{th}. In part due to the zero-current condition, the heat-carrying electrons are shifted to higher velocities $\sim 3.7 v_{th}$, and since $v_{th} \propto T_e^{1/2}$ and $\lambda_{ei} \propto T_e^2$, the corresponding mean-free-path of heat-carrying electrons is $\sim 200 \times \lambda_{ei}$. This analysis demonstrates the significant constraint on the Knudsen number which is conventionally defined with respect to the thermal electron velocity.

1.2.1.2 Flux Limiting for Large λ_{ei}/L_T

Often, Spitzer-Harm[5]–or Lee-More [54] or other local–thermal conduction is used in radiation-hydrodynamics simulations where λ_{ei}/L_T is too large for its use to be rigorously justified. Under these conditions, Equation 1.20 suggests that for large λ_{ei}/L_T the magnitude of f_1 also becomes too large relative to the zeroth-order Maxwellian f_0 description of the plasma, namely about the velocities of the heat-carrying electrons. At large temperature gradients, since f_1 is too large, the predicted heat flux $Q_e \sim \int v^5 f_1 dv$ is also too large and must be reduced. Unsurprisingly, this approach is commonly referred to as flux-limited heat transport.

To limit the heat flux, an upper bound must be defined. For electron transport, a commonly used upper bound is the free-streaming limit, where it is postulated that the thermal energy effectively advects at some maximum velocity. For the free-streaming limit, this is defined as the electron thermal velocity v_{th} characteristic of the local plasma temperature T_e. And thus the corresponding heat flux is defined as

$$Q_{FS} = n_e k_B T_e v_{th}. \tag{1.21}$$

In practice the Spitzer-Harm heat flux is limited against $f_e \times Q_{FS}$, where f_e is an introduced "flux-limiter" factor with value between zero and one, procedurally defined as a minimum or harmonic average of Q_{SH} and $f_e \times Q_{FS}$. This approach is widely used in simulations of plasmas primarily because of its ease. f_e can be calculated based upon the Knudsen number. For example, Mora and Yahi [55] calculate $f_e = 0.093$ for $\lambda_{ei}/L_T \approx 0.002$. But, historically in radiation hydrodynamics simulations of ICF experiments different values of f_e have been used, ranging from $f_e = 0.03$ to $f_e = 0.15$. Typically, changes in f_e are accompanied by adjustments to the modeling of other physical processes such as the atomic kinetics [56][57]. This implies that f_e is *ad hoc*, and has been used to compensate for deficiencies in other physics modeling relating to laser-plasmas. Inherently, this limits the predictive capabilities of modeling efforts that employ electron heat flux limiters.

The discussion here is predicated on the notion that f_1 is too large, i.e., the diffusion approximation ($f = f_0 + f_1$) is invalid. But Vlasov-Fokker-Planck simulations of laser-plasma temperature profiles for large λ_{ei}/L_T find that $f_0 + f_1$ is indeed sufficient to model nonlocal laser-plasmas, confirming the validity of the kinetic diffusion approximation for laser-plasma modeling [58]. Instead, the heat flux is strongly affected by the deviation of the symmetric part of the EDF, f_0, from a Maxwell-Boltzmann distribution [59][60]. The deviation of f_0 from f_{MB} can occur because of the influence of electron populations far away from the local EDF, or rather because the heat transport has become *nonlocal*.

1.3 Nonlocal Heat Transport

In a plasma, heat-carrying electrons have velocities 3-4 $\times$ v_{th}, or electron mean-free-paths $81 - 256 \times \lambda_{ei}$. So when temperature gradients become too steep, these electrons can quickly escape the local proximity of the temperature gradient and propagate deeper into the material before they scatter and deposit their thermal energy.

This delocalization of electrons about the temperature gradient diminishes the local population, ultimately leading to a reduction in the heat fluxes. This reduced heat flux is why a flux-limiter f_e is often necessary in modeling laser-plasmas where steep temperature gradients are produced. Further, these electrons instead deposit their thermal energy at positions far from the local temperature gradient, a phenomenon known as preheat. This aspect of the electron transport cannot be modeled with local conduction and instead requires nonlocal heat transport modeling.

So when the local temperature gradient in a plasma is sufficiently steep to enable nonlocal electron transport, the heat flux calculations should consider contributions from plasma conditions from a range of spatial locations. In hydrodynamic-scale modeling, such nonlocal heat transport effects can be considered with a convolution approach that modifies the local heat flux. This was first described by Luciani, Mora, and Virmont (LMV) [61], who proposed a nonlocal heat flux

$$Q_{NL}(x) = \int dx' Q_{SH}(x') W(x, x'), \tag{1.22}$$

where the nonlocal heat flux Q_{NL} at x considers the contribution from the Spitzer heat flux Q_{SH} at positions x' in accordance to the convolution kernel $W(x, x')$ defined by LMV as

$$W(x, x') = \frac{1}{2a(Z+1)^{1/2}\lambda_{ei}(x')} \exp\left[-\left| \int_{x'}^{x} dx'' n_e(x'')/\lambda_{ei}(x') n_e(x'), \right| \right] \tag{1.23}$$

where a is a constant that modifies the effective range of electrons at x', recommended to be $a = 32$ from Fokker-Planck simulations. For small λ_{ei}/L_T, $W(x, x')$ behaves like a delta function and the resultant heat flux is the local diffusion result. As λ_{ei}/L_T increases and the transport becomes more nonlocal, $W(x, x')$ extends the sphere of influence of the heat flux from x' to an effective region of size $2a(Z+1)^{1/2}\lambda_{ei}(x')$,

so the resulting heat flux Q_{NL} exhibits nonlocal transport behavior such as heat flux reduction at sharp temperature gradients and long-range preheat into smooth temperature regions.

1.3.1 The SNB Model

The concepts from the seminal work by LMV in reduced nonlocal transport models was extended by Schurtz, Nicolai, and Busquet into the multi-dimensional, multigroup diffusion SNB model (titled after the original authors) [1]. Their work employs a nonlocal kernel similar to W_3 from LMV, and calculates the nonlocal heat flux as:

$$Q_{SNB}(r) = Q_{SH}(r) - \sum_g \frac{\lambda_g}{3} \nabla H_g(r), \tag{1.24}$$

where the nonlocal deviation from the classical heat flux is calculated as the sum of $H_g(r)$ over electron groups g,and is calculated from solving the steady-state diffusion equation

$$\left(\frac{1}{\lambda_g(r)} - \nabla \frac{\lambda_g(r)}{3} \nabla \right) H_g(r) = -\nabla \cdot U_g(r), \tag{1.25}$$

with

$$U_g = \frac{1}{24} \int_{E_{g-1/2}/k_B T_e}^{E_{g+1/2}/k_B T_e} Q_{sh} \beta^4 e^{-\beta} d\beta, \tag{1.26}$$

$$\lambda_g = 2(E_g/k_B T_e)^2 \lambda_{ei}, \tag{1.27}$$

where $E_g = k_B T_{e,g}$ is the group energy with boundaries $E_{g\pm1/2}$. The Spitzer-Harm group contribution to the heat flux within the integrand is proportional to $\beta^4(\beta - 4)e^{-\beta}$; however in accordance with the W_3 kernel from LMV, SNB instead adopts the alternative integrand *sans* the cold electron return current factor $(\beta - 4)$, defined as $\beta^4 e^{-\beta}$. The group electron mean-free-path λ_g, specifically within Equation 1.25, is

subject to various modifications discussed both in the original publications and other studies [2][62]. These modifications affect the performance of the SNB model, and is further elaborated upon in Chapter 2.

Here, it is noteworthy to discuss the kinetic analog to the SNB nonlocal model described by the authors [63]. Like Spitzer-Harm theory, this starts with a first-order expansion of the electron distribution function, but differs by considering the deviation of the EDF such that the symmetric component f_0 is not necessarily Maxwellian, though f_0 remains close to it,

$$f_0 = f_0^m + \Delta f_0, f_1 = f_1^m + \Delta f_1, \tag{1.28}$$

where here Δf_0 and Δf_1 are the deviations of the symmetric and first-order perturbations of f. Using this definition in the zero and first-order Vlasov-Fokker-Planck equations yields

$$\begin{aligned} -\nu_{ee}\Delta f_0 - \frac{v}{3}\nabla\cdot\Delta f_1 + \frac{eE^m}{3m_e v^2}\cdot\nabla_v(v^2\Delta f_1) + \frac{e\Delta E}{3m_e v^2}\cdot\nabla_v(v^2 f_1^m) + \\ \frac{e\Delta E}{3m_e v^2}\cdot\nabla_v(v^2\Delta f_1) = \frac{v}{3}\nabla\cdot f_1^m - \frac{eE^m}{3m_e v^2}\cdot\nabla_v(v^2 f_1^m), \end{aligned} \tag{1.29}$$

$$-v\nabla\Delta f_0 + \frac{eE^m}{m_e}\nabla_v(\Delta f_0) - \nu_{ei}^*\Delta f_1 + \frac{e\Delta E}{m_e}\nabla_v(f_0^m) + \frac{e\Delta E}{m_e}\nabla_v(\Delta f_0) = 0, \tag{1.30}$$

where the electric field is defined as $E = E^m + \Delta E$, where E^m is the Maxwellian electric field derived from Spitzer theory and ΔE is the deviation of the local field due to the non-Maxwellian deviations of f_0 and f_1. The electron-ion collision frequency is defined with respect to the electron mean-free-path as $\nu_{ei} = v/\lambda_{ei}$; $\nu_{ee} = \nu_{ei}/Z$ is the electron-electron collision frequency and $\nu_{ei}^* = \nu_{ei}/\xi(Z)$ is the electron-ion collision frequency modified by the Z-dependent factor $\xi(Z) = (Z + 0.24)/(Z + 4.2)$ first proposed by Epperlein [52]. This system of equations is further simplified by only keeping dominant terms involving gradients, and furthermore by neglecting terms associated with the electric field corrections. The justification for the latter is tenuous

at best, but the authors argue it is considered within the model via a phenomenological correction to the electron mean free path. This reduces the Equations 1.29, 1.30 to

$$\nu_{ee}\Delta f_0 + \frac{v}{3}\nabla \cdot \Delta f_1 = -\frac{v}{3}\nabla \cdot g_1^m, \tag{1.31}$$

$$v\nabla \cdot \Delta f_0 + \nu_{ei}^E \Delta f_1 = 0, \tag{1.32}$$

where $g_1^m = \lambda_{ei}^E f_0^m \nabla T_e/T_e$ replaces the first-order perturbation f_1^m from Spitzer-Harm theory, again *sans* the return current term, and λ_{ei}^E is the electric-field modified mean-free-path. Like in the derivation from Spitzer, the heat flux here is dependent upon the asymmetric first-order term $f_1 = f_1^m + \Delta f_1$, so solving for ∇f_1 enables the calculation of the nonlocal heat as

$$Q_{SNB} = \frac{2\pi m_e}{3}\int_0^\infty f_1^m v^5 dv - \frac{2\pi m_e}{3}\int_0^\infty \lambda_{ei}^E \nabla \cdot (\Delta f_0) v^5 dv. \tag{1.33}$$

Equation 1.33 exhibits similarities to Equation 1.24, which defines the multigroup definition for the nonlocal heat flux within the SNB model. The first term on the right directly correlates to the Spitzer-Harm heat flux. In the limit of infinite electron groups ($g \to \infty$), $\nabla H_g \sim \nabla \cdot (\Delta f_0) v^5 dv$ in the second term. This suggests that to first-order the nonlocal heat flux in the SNB model is a deviation from the classical heat flux Q_{SH}, which is dependent upon Δf_0, or the distortion of the symmetric part of the electron distribution function. In the last term, $\nabla \cdot (\Delta f_0)$ is proportional to the mean-free-path of heat carrying electrons, so this term enables long range preheating as well as heat flux reduction in the vicinity of steep temperature gradients. In 2D and 3D simulations, these nonlocal aspects of transport also enable the heat flux to "rotate" relative to the classical Spitzer-Harm heat flux. In the local limit, an advantage of the SNB model is that it converges to the Spitzer-Harm heat flux. This can be an issue when the plasma becomes more nonlocal, and/or when f_0 is driven

further from away from a Maxwellian. This is discussed more extensively in Chapter 2.

In summary, the SNB model is a multigroup diffusion electron transport model that utilizes a convolution kernel approach to calculate nonlocal heat fluxes, formally defined within the model as a correction to the classical heat flux Q_{SH}. It has a demonstrated link to the kinetic equations, though the effect of electric fields is not consistently considered. SNB is multidimensional and incurs minimal additional computational cost [64] (primarily due to the multigroup component) compared to Spitzer-Harm conduction, and substantially less than kinetic approaches. As such, the SNB model has been implemented into many ICF radiation-hydrodynamics codes such as CHIC [65], DRACO and LILAC [66], FCI2 [1], LASNEX [56], and HYDRA [39].

1.4 Dissertation Overview

This dissertation studies the role of nonlocal electron heat transport in laser-plasmas at intensities relevant to ICF experiments. Chapter I introduced the ICF concept within the broader field of HEDP. The equations of radiation-hydrodynamics were presented, and provided context for highlighting the various challenges in modeling physics present in ICF experiments. These physics are inherently coupled to energy transport mechanisms in HEDP plasmas. In addition, this chapter discussed the laser-plasma ablation front and its fundamental role in both direct- and indirect-drive inertial fusion efforts. This was followed by an extensive discussion on kinetic, classical, and (reduced-order) nonlocal electron thermal transport modeling approaches.

Chapter II presents computational studies of laser-irradiated spheres by intensities ranging from $10^{14} - 10^{15}$ W/cm^2 for low- to mid-Z material coatings of beryllium, aluminum, and copper with the radiation-hydrodynamics code HYDRA. Much of this work is taken from a paper published in *Physics of Plasmas* by the author,

"Thermal transport modeling of laser-irradiated spheres" [67]. The electron transport is modeled at different levels of fidelity: classical Spitzer-Harm conduction, the SNB nonlocal model, and finally with the VFP equations using the code K2. Under the conditions of interest, it is found that the SNB model performs well (reducing heat flux errors <10%) compared to the kinetic heat flux, and presents a marked improvement to Spitzer-Harm theory. Furthermore, experimentally relevant effects are observed to fall outside the prediction space of Spitzer-Harm thermal transport, even when considering *ad hoc* flux limiting. The correlation of these effects to aspects of nonlocal transport are identified and discussed.

Chapter III presents further studies of laser-irradiated spheres, exploring the coupling of nonlocal electron transport with the radiation energy transport. While the research in chapter II identities the effect of increased heat fluxes upon the heated plasma's self-emission as dictated by the deviation of the anisotropic component of the EDF, f_1, this chapter extends the research in considering the effect of the non-Maxwellian EDFs, or the deviation of the symmetric component f_0. To accurately conisder non-Maxwellian electron energy distributions, the atomic-kinetics code Cretin is used with fully discretized electron energy distributions. Non-Maxwellian electron distributions are either calculated from the K2-VFP kinetic code, or from analytical Langdon distributions [68]. Cretin simulations are calculated for both 0D and 1D plasma conditions from laser-irradiated spheres, and the resulting emissivities and transmitted radiative spectra are discussed.

Finally the dissertation is bookended by the conclusion, where the work is summarized and discussed. Chapter IV also touches upon the limitations of the present research as well as as future directions to take this work.

CHAPTER II

Laser-Irradiated spheres I: Thermal Transport Modeling

This chapter and Appendix A are adapted from Ma, K. H., Patel, M.V., Sherlock, M., Farmer, W.A., & Johnsen, E. 2022: Thermal transport modeling of laser-irradiated spheres *Physics of Plasmas* **29 (11)**, 112307.

2.1 Abstract

Thermal transport of uniformly laser-irradiated spheres of various materials is investigated computationally. One-dimensional simulations of low- to mid-Z materials (Be, Al, Cu) are performed to evaluate the impact of nonlocal electron transport on experimental observables under laser intensities of relevance to direct-drive inertial confinement fusion. We compare thermal transport models of different levels of fidelity: flux-limited Spitzer-Harm diffusion, the Schurtz-Nicolai-Busquet (SNB) reduced-order nonlocal model, and a Fokker-Planck description. Spitzer-Harm diffusion with different flux-limiter factors are compared with different implementations of the SNB model in the HYDRA radiation hydrodynamics code. Under the conditions of interest, the peak heat flux in the thermal front with the SNB model shows good agreement with Fokker-Planck calculations, with the largest errors below 10% at

10^{15} W/cm^2 laser intensity. From HYDRA-SNB simulations, two experimentally relevant effects are observed from nonlocal heat transport when compared to flux-limited Spitzer-Harm modeling: coronal temperatures are cooler due to reduced heat fluxes in the expanding plasma, and (for mid-Z materials) X-ray emissions are enhanced due to preheating in the dense plasma.

2.2 Introduction

Modeling of electron thermal transport plays a significant role in simulations of laser-generated plasmas produced in inertial confinement fusion (ICF) experiments. However, at laser intensities relevant to direct-drive ICF ($10^{14} - 10^{15}$ W/cm^2), steep temperature gradients are generated and the electron transport departs from classical. [60] The transport exhibits nonlocal effects such as heat flux inhibition at steep gradients in electron temperature, and long-range heating of the plasma, or preheat [69].

In radiation-hydrodynamics codes, thermal transport is commonly modeled by classical Spitzer-Harm local diffusion [5], in which the local heat flux $Q_{SH} = -\kappa_{SH}\nabla T_e$, where T_e is the electron temperature, and the thermal conductivity κ_{SH} is proportional to $T_e^{5/2}$. This local diffusion representation of heat flux is valid when the temperature gradient scale-length $L_T = T_e/|\nabla T_e|$ is much larger than the electron mean-free-path λ_{ei}, defined as:

$$\lambda_{ei} = \frac{T_e^2}{4\pi Z n_e e^4 \Lambda_{ei}}, \tag{2.1}$$

where T_e is the electron temperature, n_e and e the electron density and charge respectively, and Λ_{ei} is the Coulomb logarithm for electron-ion interactions. Generally, Spitzer-Harm transport is valid when $\lambda_{ei}/L_T \ll 0.01$, however ICF experiments often do not satisfy this requirement for the classical Spitzer-Harm heat flux, and the

hot temperatures and steep temperature gradients result in unreasonably high local electron thermal fluxes. In simulations, this issue is addressed by limiting the Spitzer-Harm heat flux to the free-stream heat flux, $Q_{FS} = n_e k_B T_e v_e$, multiplied by a flux-limiter factor f_e, where n_e is the electron number density and $v_e = \sqrt{k_B T_e / m_e}$ is the local electron thermal velocity. Ultimately, the choice for f_e is ad hoc, based on attempts to match experimental observables [57][56][17]. The reduced heat flux results from the delocalization of the suprathermal heat-carrying electrons at a range of velocities $3.7 \times v_e$ relative to the local plasma temperature, resulting in preheating [69] in addition to the aforementioned local heat flux inhibition. Furthermore, heat flux inhibition can manifest from short wavelength k (relative to λ_{ei}) temperature perturbations, even if λ_{ei}/L_T is above the previously stated threshold [52]. As the Spitzer-Harm heat flux is a local diffusion term, a flux-limited approach is unable to model these nonlocal effects. A higher-fidelity treatment of electron thermal transport can be achieved through numerically solving the Vlasov-Fokker-Planck (VFP) equations, which consistently calculates the electron heat flux with the evolution of the electron velocity distribution function (EDF). However, such kinetic approaches require significant additional computational expense due to added dimensionality and more restrictive time steps. Additionally, it is difficult to include equations of state, atomic physics modeling, and radiation transport. As a result, an in-line kinetic approach is not presently viable for integrated ICF simulations.

However, nonlocal effects must be considered to ensure accurate modeling of ICF experiments. For example, in direct-drive ICF, nonlocal transport is necessary to accurately predict laser-energy coupling [70], shock timing [71], perturbation instability growth, [72] and preheat of the fuel core [66], which affect computed performance characteristics such as the implosion velocity, implosion adiabat, and peak areal density [73]. Consequently, multi-physics ICF codes often implement reduced nonlocal electron thermal transport models, a subset of which utilize a convolution kernel

approach [60][61]. Two notable models are the multi-dimensional, multigroup diffusion Schurtz-Nicolai-Busquet (SNB) model [1], and the Krook collision operator Colombant-Manheimer-Goncharov (CMG) model [74]. Both of these models have demonstrated links to the VFP kinetic equations. The present work focuses on SNB, which has been implemented into the CHIC [65], DRACO and LILAC [66], FCI2 [1] and HYDRA [39] ICF codes. SNB has been benchmarked against VFP codes in ICF-relevant plasma conditions [64], [2][62], and in principle, could be extended to incorporate magnetic fields [75].

The present studies assess nonlocal electron transport effects in low- to mid-Z direct-drive spheres, but having solid cores to maintain focus on the laser-plasma ablation front. In relation to ICF efforts, similar experiments have been performed to study high-Z materials relevant to hohlraum design [76][77][78][79], focusing on the underlying physics relating to modeling X-ray conversion efficiencies such as radiation transport, atomic physics, and laser-plasma interactions in addition to electron transport modeling. Laser-irradiated planar foil experiments have also been performed for similar purposes [65][80][81][82][83][84][85], however they lack the physical advantages the spherical geometry provides in minimizing self-generated magnetic fields [86], as well as diagnostic advantages in assessing laser-coupling, X-ray emissions, and plasma conditions. Given the various physics inherent in high-Z spheres, such systems still prove challenging to model. With low- to mid-Z materials some of these physical processes can be decoupled, as these materials exhibit fewer ionization states, reducing uncertainties from Non-Local Thermodynamic Equilibrium (NLTE) modeling [44], and also present stronger ion Landau damping, reducing one mechanism of micro-turbulence [58]. Recent experiments corroborate the advantages in both the simplicity and enhanced diagnostic capabilities in this system [87][79], indicating the laser-irradiated sphere is well tailored towards investigating nonlocal electron transport.

The primary objective of this work is to computationally study nonlocal transport effects in low-to mid-Z irradiated spheres at laser intensities ($10^{14} - 10^{15}$ W/cm^2) relevant to ICF experiments. To this end, we assess the accuracy of the HYDRA-SNB model for the range of materials and laser intensities in this study via comparisons with Fokker-Planck calculations from the kinetic code K2 [62]. A description of these models and the simulation parameters are given in section 2.3. Simulation results are presented in section 2.4, first from SNB and kinetic heat flux comparisons in stationary plasmas, then from an inline kinetic temperature evolution incorporating time-dependence, and finally from integrated radiation-hydrodynamics simulations in HYDRA. In section 2.5, experimental observables from HYDRA-SNB simulations relating to observed nonlocal effects are described. Section 2.6 provides a discussion of simulation results before the relevant conclusions are given in section 2.7.

2.3 Models and Methods

2.3.1 SNB Transport Model

The multigroup Schurtz-Nicolai-Busquet (SNB) nonlocal model [1] defines the nonlocal heat flux, $\mathbf{Q}_t$, as a sum of nonlocal corrections to the Spitzer-Harm heat flux $\mathbf{Q}_{sh}$ for each of N discretized electron energy distribution groups:

$$\mathbf{Q}_t(\mathbf{r}) = \mathbf{Q}_{sh}(\mathbf{r}) - \sum_g^N \frac{\lambda_{g,ei}(\mathbf{r})}{3} \nabla H_g(\mathbf{r}), \tag{2.2}$$

Here $\lambda_{g,ei}(\mathbf{r})$ is the group electron-ion mean-free-path (mfp), and $H_g(\mathbf{r})$ is calculated from multigroup steady state diffusion transport equations:

$$\left(\frac{r}{\lambda_{g,ee}(\mathbf{r})} - \nabla \cdot \frac{\lambda'_{g,ei}(\mathbf{r})}{3} \nabla \right) H_g(\mathbf{r}) = -\nabla \cdot \mathbf{U_g}, \tag{2.3}$$

where:

$$\mathbf{U_g} = \frac{1}{24} \int_{E_{g-1/2}/k_B T_e}^{E_{g+1/2}/k_B T_e} \beta^4 \mathrm{e}^{-\beta} d\beta \mathbf{Q}_{sh}, \tag{2.4}$$

$$\lambda'_{g,ei} = \left[1/(\xi\lambda_{g,ei}) + 1/\lambda_{g,\mathcal{E}}\right]^{-1}, \tag{2.5}$$

$$\lambda_{g,ee} = Z\lambda_{g,ei}, \tag{2.6}$$

$$\lambda_{g,ei} = 2(E_g/k_B T_e)^2 \lambda_{ei}, \tag{2.7}$$

$$\lambda_{g,\mathcal{E}} = E_g/k_B T_e |e\mathcal{E}|, \tag{2.8}$$

where $E_g = k_B T_{e,g}$ is the group energy with energy boundaries $E_{g\pm1/2}$, and Z the material ionization. The group electron-ion mfp $\lambda'_{g,ei}$ within Eq. 2.5 incorporates the effect of electric fields by the inclusion of $\lambda_{g,\mathcal{E}}$ defined in Eq. 2.8, where $\mathcal{E}(T_e,\ n_e,\ Z)$ is the Spitzer electric field [1], which serves to restricts nonlocal deviations from Q_{SH} in regions with strong electric fields. ξ is an electron-ion collision fix, while the factor r on λ_{ee} emerges from discrepancies amongst SNB implementations in various studies. These adjustments to the mfp definitions are further described in Sec. III.C. of Brodrick et al. [2], where is it found that SNB implemented with $r = 2$ and $\xi(Z) = (Z + 0.24)/(Z + 4.2)$, corresponding to the ionization-dependent collision fix, first proposed by Epperlein and Short [52], brings SNB predictions in better agreement with VFP modeling. In addition, it is noted here that the present implementation of SNB within HYDRA incorporates a factor of 4 correction to λ_{ei} and λ_{ee} due to differences in v_e definitions between HYDRA and the IMPACT VFP code. [88]

In this study four variations of SNB are considered in HYDRA simulations, which are briefly summarized in Table 2.1. The above described corrections are implemented in the baseline HYDRA-SNB configuration, henceforth referred to as Base-SNB. The second model considered represents a reversion towards SNB without the described

improvements ($r = 1, \xi = 1$), and is referred to as noBR-SNB. The other two SNB variations are motivated by previous work by Sherlock et al. [62]. The third, noSL-SNB, discounts the effect of separate mfp definitions for electron-electron and electron-ion collisions by employing geometrically averaged mfp $\lambda_g = \sqrt{\xi \lambda_{g,ee} \lambda'_{g,ei}/r}$ for both collision terms in Eqn (3), akin to SNB formulation in the original publication [1]. This treatment assumes constant average ionization Z in the plasma [2][62], while SNB with λ_{ei} and λ_{ee} considered separately appropriately considers ionization gradients present in the plasma profile. The fourth variant, noEF-SNB, neglects the Spitzer-electric field correction $\lambda_{g,\mathcal{E}}$ to $\lambda_{g,ei}$, which was found to faciliate better agreement with VFP calculations. [62]

2.3.2 HYDRA Laser-Irradiated Sphere Model

The HYDRA laser-irradiated sphere model is based upon an OMEGA platform used for sphere experiments [77][87][79] Figure 2.1 exhibits a cross-section schematic of the laser-irradiated sphere, which has an outer radius of 430 μm. The solid sphere is

Table 2.1: Overview of variations in SNB models used, with $\xi = (Z+0.24)/(Z+4.2)$, and Krook collision correction factor $r = 2$. The mean free path definitions $\lambda_{g,ee}$, $\lambda_{g,ei}$ correspond to those used in Equation 2.3, and $\lambda_{g,\mathcal{E}}$ is the Spitzer electric-field correction to the electron-ion mean-free-path.

Name	$\lambda_{g,ee}$	$\lambda'_{g,ei}$
Base	$\lambda_{g0,ee}/r$	$\left[\frac{1}{\xi\lambda_{g0,ei}} + \frac{1}{\lambda_{g,\mathcal{E}}}\right]^{-1}$
noBR	$\lambda_{g0,ee}$	$\left[\frac{1}{\lambda_{g0,ei}} + \frac{1}{\lambda_{g,\mathcal{E}}}\right]^{-1}$
noSL	$\sqrt{\xi\lambda_{g0,ee}\lambda_{g0,ei}}/r$	$\left[\frac{1}{\sqrt{\xi\lambda_{g0,ee}\lambda_{g0,ei}}} + \frac{1}{\lambda_{g,\mathcal{E}}}\right]^{-1}$
noEF	$\lambda_{g0,ee}/r$	$\xi\lambda_{g0,ei}$

comprised of an inner 417.5 μm of solid carbon with density 1 g/cm^3, coated by a 12.5 μm layer of low- to mid-Z material. We consider three materials to assess both the consistency of the SNB model and resulting effects from nonlocal heat fluxes against atomic number: beryllium (Z = 4) with mass density ρ = 1.83 g/cm^3, aluminum (Z = 13) with ρ = 2.7 g/cm^3, and copper (Z = 29) with ρ = 8.96 g/cm^3. The sphere is uniformly irradiated by sixty 351 nm wavelength (3ω) beams, with intensity profile $I(r) = I_o \mathrm{e}^{-\left(\frac{r}{r_o}\right)^n}$, where r is the profile radius in microns, r_o = 358 μm and n = 5.2. In our studies, we consider three laser pulses relevant to ICF conditions, with $I_L = 10^{14} - 10^{15}$ W/cm^2. All three laser pulses are square pulses with 200 ps rise time, and are constrained to conditions relevant to OMEGA experiments. They consist of the following total energy and duration:

- 4.8 kJ in 2 nanoseconds, $I_L \sim 1.03 \times 10^{14}$W/cm^2.
- 24 kJ in 2 nanoseconds, $I_L \sim 5.2 \times 10^{14}$W/cm^2.
- 24 kJ in 1 nanoseconds, $I_L \sim 1.03 \times 10^{15}$W/cm^2.

The 1D-sphere is simulated with the multiphysics radiation hydrodynamics code HYDRA [42]. The radiation transfer equation is solved using a polar S_N (discrete ordinates) method [89] with 24 discrete angles and 60 energy groups. Additionally, simulations are performed using the multigroup flux-limited radiation diffusion approximation, and the effect of the radiation transport method is briefly discussed in section 2.5. The materials are modeled with tabulated equations of states from LEOS and TABOP local-thermodynamic equilibrium (LTE) opacities. In the hot, underdense corona the collisional-radiative model DCA [44] is employed to describe the non-LTE atomic kinetics. The threshold for transitioning from LTE tabulated data to the non-LTE DCA model is set at T_{NLTE} = 100 eV so that the transition occurs in the dense plasma. In these studies, T_{NLTE} was varied $\pm$50 eV about this temperature, and no changes in the resulting simulations was observed. The laser source

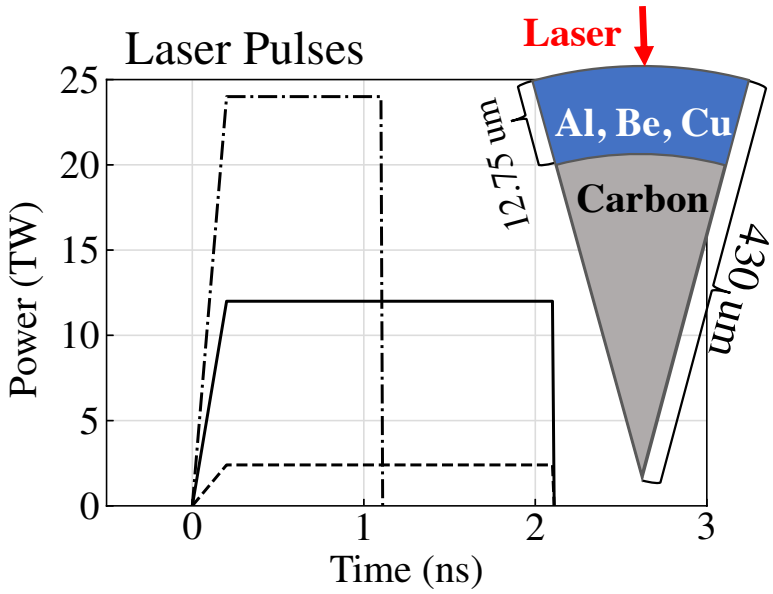

Figure 2.1: Pulse shapes used for studying OMEGA equivalent systems, with laser intensities of 1.03 $\times 10^{14}$ W/cm^2 (dashed), 5.2 $\times 10^{14}$ W/cm^2 (solid), and 1.03 $\times 10^{15}$ W/cm^2 (dot-dashed). The sphere is comprised of a solid carbon center, and 12.5 μm coating of material, for which cross-section schematic is overlaid.

is modeled as inverse-bremsstrahlung absorption using the spherical laser deposition model in HYDRA. This package is designed to illuminate spheres while producing a minimal amount of statistical noise. The capsule is illuminated with 200 parallel rays equally spaced across the beam width. This accounts for the essential effects of refraction due to the converging capsule geometry. Approximately 2600 Lagrangian zones are used in the simulation domain, which ensures $< 2.5\%$ variation in the laser absorption, coronal T_e and n_e quantities due to resolution effects (see Appendix for details regarding resolution and convergence).

Simulations are performed using flux-limited Spitzer-Harm diffusion over a range of flux-limiter factors $f_e = [0.03 - 0.15]$. Simulations with the nonlocal package model thermal transport classically with Spitzer-Harm until the maximum Knudsen number $Kn = \lambda_{ei}/L_T$ in the domain exceeds 10^{-2}, beyond which the electron transport is modeled with SNB nonlocal transport. This threshold is set so that the SNB

model is used when nonlocal effects in thermal transport become significant [60], while the Spitzer-Harm transport term is sufficient in the classical regime. The transition between thermal transport models occurs within the first 50 ps of the 200 ps laser pulse rise, such that $< 1\%$ of the total laser energy deposition in our nonlocal calculations is modeled with Spitzer-Harm transport.

In the SNB multigroup diffusion model, energy groups are discretized with respect to the integral in Equation 2.4. In HYDRA's implementation of SNB, these energy groups can be rescaled with the plasma temperature. The first energy bin between E_0 and E_1 is further discretized into "cold groups" evenly spaced in energy, which ensures the rapid rise in the integral is well resolved. The present study uses a (20/60) energy group (cold/total) configuration with temperature rescaling, which is sufficient to converge the heat flux calculation.

2.3.3 K2 Vlasov-Fokker-Planck Model

In this work, the Lagrangian Vlasov-Fokker-Planck (VFP) code K2 [62] is used to calculate kinetic heat fluxes for comparison with SNB modeling. K2 solves the VFP equation for the electron distribution function (EDF), $f(\mathbf{x}, \mathbf{p}, t)$, expanded in spherical harmonics in momentum-space $(\mathbf{p}, \theta, \phi)$ up to arbitrary order. In addition, K2 is capable of coupling the electron VFP equation to the radiation hydrodynamic equations via heating and cooling operators to account for PdV work and radiative cooling, and through advecting the EDF with hydrodynamic ion motion to maintain quasi-neutrality. Magnetic fields are not considered in the 1D spherical domain, and only the f_0 and f_1 spherical harmonics are used in these calculations. Harmonics n (with $n > 2$) are not accounted for in these simulations because they are damped in proportion to $n(n+1)$, as well as being proportional to gradients of the previous order harmonic [90]. However, it is noted that we also performed K2 calculations with f_2 and did not observe significant differences in calculated heat fluxes. As the

focus of this work is on the electron heat flux, energy transport due to radiation absorption, radiation emission, and hydrodynamic motion is not accounted for. A thorough overview of the VFP model in K2 is provided in Sherlock et al. [62].

In Section 2.4.1, plasma conditions from HYDRA-SNB simulations are used to initialize K2 simulations, from which the VFP heat fluxes are calculated. As the EDF evolves in time the temperature profile naturally relaxes from the initial condition, so external heating and cooling operators are applied to $f(\mathbf{x}, t)$ for the duration of the calculation to maintain the local plasma temperature. The heating operator is of the Langdon form [68]. For cooling, a modified Langdon operator is used, which shifts the EDF towards a Maxwellian, similar to radiation hydrodynamic effects such as PdV work and radiative cooling.

Section 2.4.2 presents results from modeling the temperature evolution of an ablated beryllium plasma heated by a laser. Laser energy deposition in K2 is modeled with the inverse bremmstrahlung heating term C_{IB} given by Weng et. al [91]. To model the attenuation of the laser intensity as it propagates through the spatial domain, K2 solves a simple 1D ray equation:

$$\frac{dI(x)}{dx} = -\kappa(x)I(x), \tag{2.9}$$

where $\kappa(x)$ is an inverse bremsstrahlung absorption coefficient that is self-consistently calculated with respect to the IB energy deposition given by C_{IB}.

2.4 Results

2.4.1 Heat Flux Calculations in Stationary Ablation Front Profiles

We first compare heat flux predictions for the range of plasma conditions generated from HYDRA-SNB simulations across for various laser intensities and materials under consideration. Specifically, plasma conditions for these comparisons are taken

from Base-SNB HYDRA simulations discussed in Section 2.4.3. K2 kinetics calculations are initiated on a spatially uniform, 1000 cell mesh, with initial conditions interpolated from HYDRA simulation outputs (T_e, n_e, Z). The momentum grid is evenly discretized over 180 groups with $p_{max} = 6p_T$, where $p_T = m_e v_T$ corresponds to the maximum thermal velocity v_T in the HYDRA profile. A CFL number of 0.5 is used, with time step Δt dependent upon the electron-ion collision time τ_{ei}. In these K2-VFP simulations, $\Delta t \sim 1 - 10 fs$. The heating and cooling operators described in 2.3.3 maintain the temperature profile as the initial Spitzer-Harm heat flux evolves a quasi-steady VFP heat flux, which occurs within a few picoseconds.

We first consider the features observed in the Cu-sphere case, heated by a laser intensity of 10^{15} W/cm^2, because this simulation exhibited the highest nonlocality, and correspondingly the highest departure from classical electron transport. Figure 2.2 shows plasma conditions at $t = 1$ ns from a HYDRA-SNB simulation of a copper coated sphere irradiated with $I_L = 1.03 \times 10^{15}$ W/cm^2. In this profile, the ratio of the electron mean-free-path to temperature gradient length-scale, λ_{ei}/L_T is ~ 0.025 near the critical density n_c, and λ_{ei}/L_T ranges from $0.01 - 0.02$ for electron densities below n_c at larger radii. The temperature and electron density profiles shown here are typical for single materials illuminated by a 350 μm laser for this range of HYDRA simulations. Here, the laser propagates from right-to-left, with the laser power deposition represented by the black line (A.U.) up until the critical electron density n_c. At radii beyond n_c lies the underdense, coronal plasma. At large r, the ablated plasma undergoes free expansion. This rarefied, optically thin plasma is strongly (but not entirely) decoupled from radiation transport, electron thermal transport, and laser heating. The cyan region encompasses the near-corona from $0.1 n_c$ up to the critical density n_c, within which the underdense plasma is strongly coupled to both electron transport and the laser heating, which drives the flow evolution. Approximately 80-90% of the laser energy is deposited here. The plasma at densities

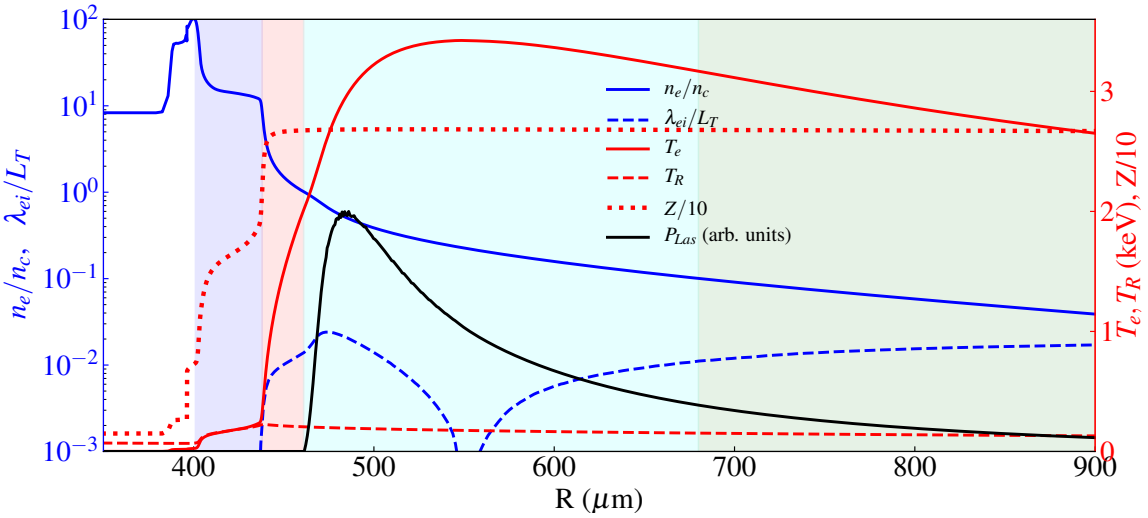

Figure 2.2: Electron density (solid blue), electron temperature (solid red), radiation temperature (red dashed), average ionization $Z/10$ (red dotted), ratio of electron mean-free-path to temperature gradient scale length λ_{ei}/L_T (blue dashed), and arbitrary unit laser energy deposition (black) profiles from a copper sphere HYDRA simulation irradiated by 1×10^{15} W/cm^2 square pulse at t = 1 ns. In this profile, the maximum λ_{ei}/L_T is approximately 0.025 near the critical density. Highlighted color regions correspond to the following(from left to right): The radiation transport dominated front (blue), the electron thermal transport front ending at the critical density n_c (red), the coronal plasma (cyan), and the free expansion region (green).

$> n_c$ compose the ablation front, which is seperated into two regions based upon the dominant energy transport mechanism. Electron heat transport is dominant in the red region, while radiation energy transport dominates in the blue region where $T_e \approx T_R$. This double-temperature front and corresponding density profile, i.e. double-ablation front [46], emerges in laser-ablation profiles for moderate-to-high Z materials, as radiation heat fluxes become significant in addition to the electron heat fluxes present in the dense, heated plasma.

Heat fluxes are shown in Figure 2.3, with peak heat flux located at radius $r \approx 470$ μm, or near the interface of the electron transport dominated and near-coronal regions. Here, the peak heat flux predicted by Spitzer-Harm exceeds the kinetic heat flux by approximately a factor of 2. The SNB model variants present a significant improvement. Amongst SNB variations, noBR-SNB exhibits the largest differences

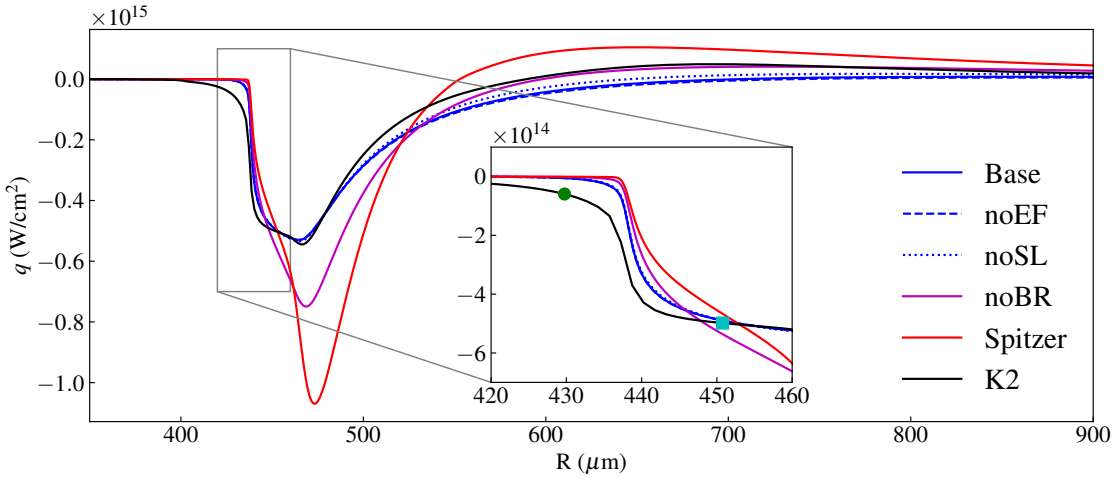

Figure 2.3: Heat fluxes in the ablation front for the initial conditions modeled in Fig. 2.2. Black: K2-VFP, red : Spitzer-Harm, green: noBR-SNB, solid-blue: Base-SNB, dashed-blue: noEF-SNB, dotted-blue: noSL-SNB. The peak nonlocal heat flux (at about 470 μm) is reduced from the classical Spitzer-Harm local heat flux. Of the SNB models, those with the corrections suggested by Brodrick et al exhibited the best agreement with Fokker-Planck calculations. Inset: Electron transport thermal fronts near the radiation front. The green circle and cyan square symbols correspond to heat fluxes from the K2-VFP calculation at the bottom and top of the conduction front, respectively.

from the kinetic heat flux, overpredicting the peak heat flux by 40%. The other SNB configurations differ from the K2-VFP calculation by only a few percent, and are nearly indistinguishable from each other. The inset in Fig. 2.3 shows the electron heat fluxes in the ablation region. The classical Spitzer-Harm heat flux follows the temperature profile, with the foot of the corresponding heat flux ending at the beginning of the radiation-dominated region at approximately 440 μm. In contrast, heat fluxes produced by various other approaches advance further inwards into the radiation dominated region, corresponding to varying degrees of preheat, with K2-VFP exhibiting the longest range preheating, noBR-SNB predicting the shortest, and other SNB preheat profiles between them.

Fig. 2.4 inspects the $f_0(v)$ distribution as well as the scaled fifth velocity moment anisotropic component of the EDF proportional to the heat flux distribution,

$dQ_{VFP} \sim v^5 f_1(v) dv$ at specific radial positions. The corresponding Maxwellian EDF and Spitzer-Harm heat fluxes calculated from local plasma conditions are also shown. These two panels correspond to radial positions from the K2-VFP simulation indicated by the green circle and the cyan square symbols in Figure 2.3. The first position (at $r = 450$ μm) is along the steep temperature front within the electron-transport-dominated region, with local $T_e = 1.5$ keV, $Z = 27$, $n_e = 1.35 \times 10^{22}$ cm^{-3}, and $\Lambda_{ei} = 4.55$. Here the inward kinetic heat flux is 4.9×10^{14} W/cm^2 and higher (due to preheat) than the local heat flux (4.5×10^{14} W/cm^2). A closer inspection of the distribution in Fig. 2.4(a) indicates that the local plasma has accumulated a high velocity tail of electrons relative to the equivalent Maxwellian, presumably from hotter regions up the temperature front. The heat flux distribution also suggests this behavior given the increased contribution to Q_{VFP} by faster electrons. In addition, $v^5 f_1$ indicates a reduction in heat contribution due to the delocalization of electrons about $3.7 v/v_T$ relative to the classic Spitzer-Harm heat flux.

The second position at $r = 430\mu$m is located at the foot of the electron temperature front within the radiation dominated region, with local $T_e = 0.2$ keV, $Z = 17.3$, $n_e = 1.2 \times 10^{23}$ cm^{-3}, and $\Lambda_{ei} = 2.04$. Relative to the previous position, f_0 shows a substantially higher velocity tail in Fig. 2.4(b). At this position, K2 predicts substantial preheating relative to the classical heat flux, exhibiting a much larger heat flux distribution, which is also shifted to higher velocities with the largest contribution centered around 13 v/v_T or ~ 34 keV.

In the coronal region, kinetic heat fluxes are also reduced relative to Spitzer-Harm. For local diffusion, the heat flux transitions from propagating into the dense sphere to outwards towards heating the corona plasma beyond the peak temperature 3.2 keV at approximately $r = 550\mu$m. In K2-VFP simulation this turning behavior occurs further outwards at $r = 590\mu$m, and instead there lies an intermediate 40 μm region where the heat flows inwards against the temperature gradient due to delocalized

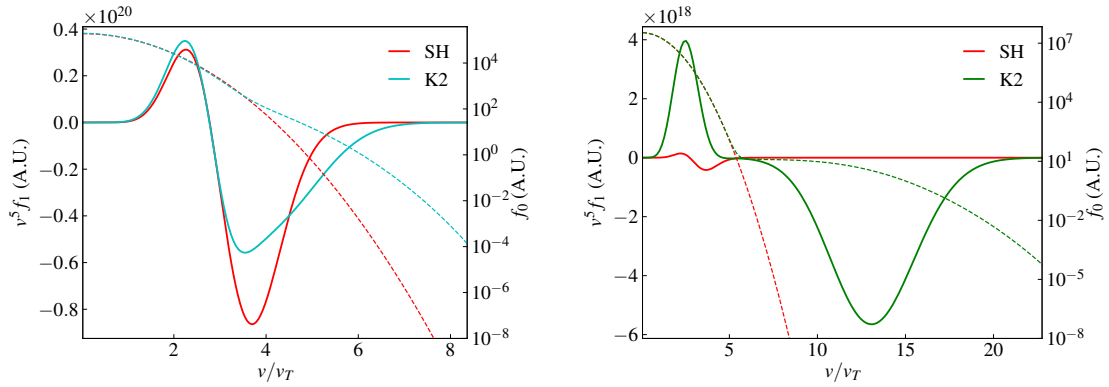

Figure 2.4: EDFs f (dashed) and heat flux proportional $v^5 f_1$ (solid) distributions plotted vs normalized velocities v/v_T from K2-VFP calculations (black) given in Fig 2.3 (a) near peak heat flux at radius $r = 450$ μm (cyan) in the electron heat flux dominated region and (b) at the foot of the temperature profile at radius $r = 430$ μm (green) in the radiation-dominated region. The corresponding Spitzer-Harm distributions for f and $v^5 f_1$ (red) are calculated from local plasma conditions.

electrons escaping towards the ablation region. Beyond the near-corona in the free expansion region, K2-VFP heat fluxes are smaller than Spitzer-Harm heat fluxes by about a factor of 2. For SNB larger differences in the heat predictions are observed among the model variations in the coronal region, though all models qualitatively indicate heat flux reduction like K2-VFP. Curiously, in the free expansion region it is observed that noBR-SNB, which predicts the largest outward heat flux, is closest to the K2-VFP result. Other SNB heat fluxes are decreased, moving further away from the kinetic prediction. Specifically, noSL-SNB predicts the largest heat flux among the three, and noEF-SNB predicts the smallest.

Similar behavior is observed in stationary profiles from beryllium and aluminum HYDRA simulations. We observe disagreements in the coronal heat fluxes, and consistently longer range preheating by K2-VFP than any of the SNB model variations. At lower laser intensities, the thermal transport in the laser-ablation profile becomes more local, and all heat transport predictions (VFP, SNB, Spitzer-Harm) lie closer. Differences in the largest predicted heat flux in the ablation region are summarized in Figure 2.5, as the percentage difference between HYDRA-SNB and K2-VFP heat

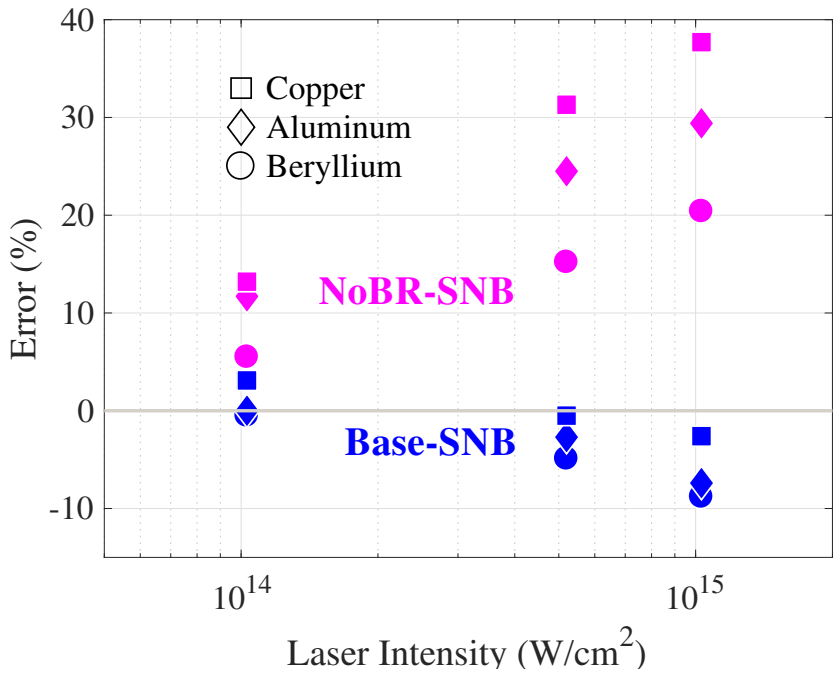

Figure 2.5: Heat flux differences of noBR SNB and Base SNB when compared to K2 (VFP), for different laser intensities in Be, Al, and Cu-spheres. With the corrections suggested by Brodrick et al., both the accuracy of the SNB nonlocal model and its consistency across different materials is improved. All comparisons are made at $t = 1$ ns, when the laser-plasma ablation front is well developed.

fluxes for the Base-SNB and noBR-SNB variations. This panel shows the Brodrick corrections incorporated in the Base-SNB model substantially improve agreement with K2-VFP heat flux predictions, reducing the difference compared to K2-VFP from 40% to <10% at 10^{15} W/cm^2 laser intensity, and essentially agreeing at lower laser intensities. Furthermore, these adjustments result in more consistent performance across the range of Z in our studies, and it is worthwhile here to reiterate that the corrections suggested by Broderick [2] extend the range of applicability of the SNB model.

2.4.2 K2-VFP Inline Temperature Evolution

Now, a more direct comparison between the VFP and SNB models is considered by simulating the evolution of two temperature profiles: one with K2-VFP heat fluxes,

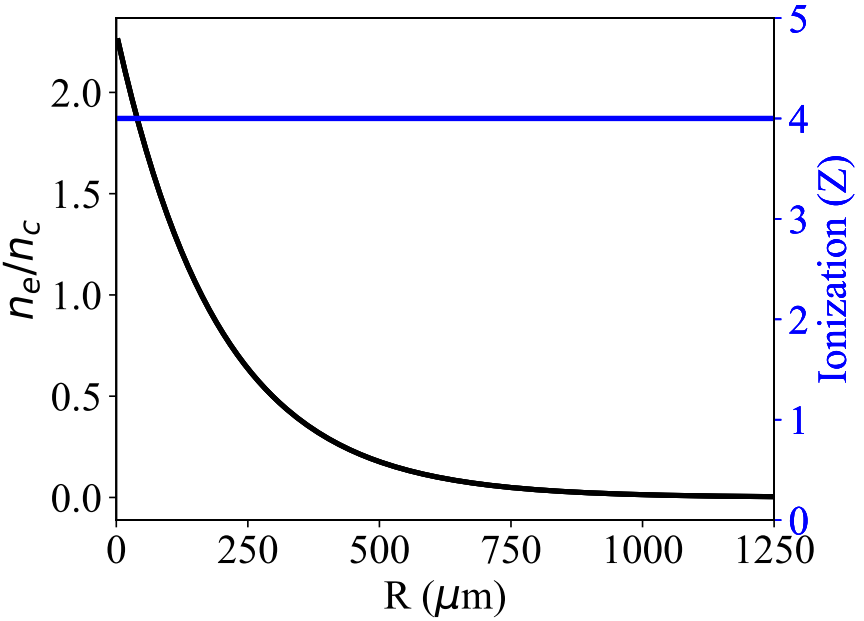

Figure 2.6: Initial normalized electron density n_e/n_c (black) and material ionization Z (blue) for K2 beryllium sphere temperature evolution simulation, irradiated at 5 $\times 10^{14}$ W/cm^2 laser intensity.

and the other with heat fluxes from the kinetic SNB model implemented in K2 [62], which is equivalent to the $r = 2$ Base-SNB model. The test problem consists of a beryllium plasma, irradiated by a 3ω-square pulse with 100 ps rise time and peak intensity of 5×10^{14} W/cm^2 using K2's laser energy deposition model. The initial electron density and ionization conditions are shown in Figure 2.6. The beryllium is modeled as fully ionized (Z = 4), while the electron density profile is exponential with gradient scale length $L_{n_e} \sim 200$ μm, which assumes the plasma expanded isothermally [3]. The electron densities in the domain spans the electron dominated region and the corona, with electron densities ranging from $(0.001 - 2)n_c$. The plasma temperatures rise in time, with $T_e \sim 2.9$ keV at 500 ps.

In this test, the evolving temperature profiles highlight the effect of differences in SNB and VFP heat fluxes. K2-VFP and K2-SNB electron temperatures are shown at different times in Figure 2.7 to illustrate how the two temperature profiles evolve over the duration of the laser-heating. The maximum electron temperatures of the two

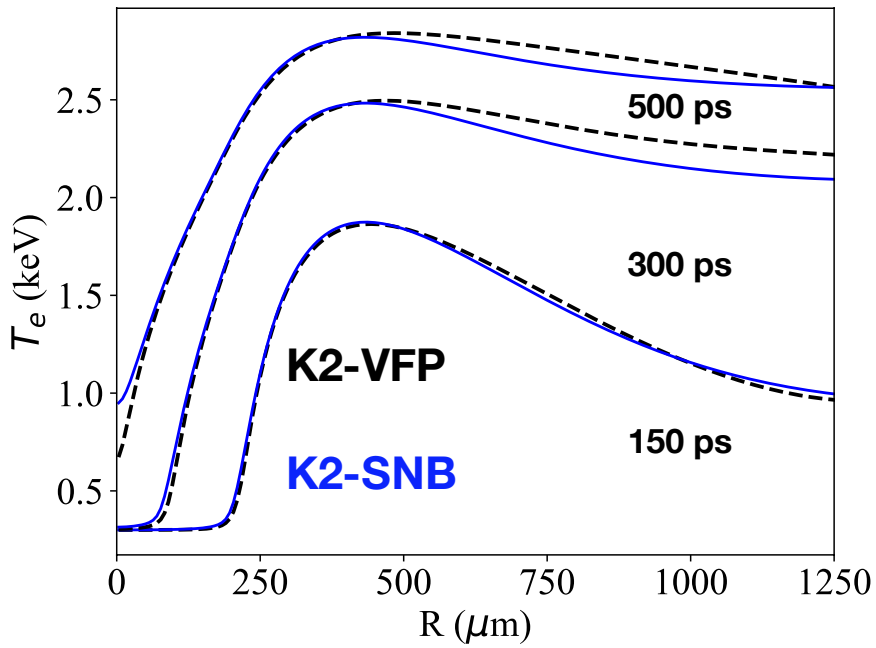

Figure 2.7: Electron temperatures for K2-VFP (black-dashed) and K2-SNB (blue) temperature profiles at 150 ps, 300 ps, and 500 ps. In the low-density corona, the electron temperatures remain fairly close for the duration of the temperature-evolution test.

profiles (positioned in the range of 0.1-0.3 n_c) remains close as the temperature profile rises. In the innermost region, the K2-SNB heat flux is larger and the temperature front advances further into the dense plasma than the front from K2-VFP. This different trend in the ablation region temperature profiles compared to the previous section is because the density profile is still exponential beyond n_c, while the density gradients are much sharper beyond n_C in the sphere profiles. In the corona region, electron temperatures from K2-VFP modeling are greater than those obtained from K2-SNB, which corresponds to the larger coronal heat flux observed from stationary profile comparisons. However from these simulations it is found that these differences are relatively small, on the order of 50-75 eV or 2-3% at the end of the laser heating. In addition, the temperatures are closer to each other than at $t = 300$ ps, where K2-SNB is cooler by 100-150 eV. The convergence of coronal temperatures suggests smaller errors in the heat flux are to a degree self-correcting: If the heat flux is too small,

the temperature gradient steepens. Subsequently, the steeper temperature gradients result in a larger heat flux.

2.4.3 Radiation-Hydrodynamics Modeling

In this section, the SNB model is considered in HYDRA radiation-hydrodynamics simulations, to assess how differences between SNB and flux-limited Spitzer-Harm, i.e., local diffusion, affect the laser-plasma evolution. Though the flux limiter is an *ad hoc* approach, it is still worthwhile to determine whether nonlocal transport effects can be reasonably modeled with an appropriate value of f_e. Similar work showed that at these laser intensities ($10^{14} - 10^{15}$ W/cm^2) an initial flux limiter with $f_e \sim 0.09$ at early time and subsequently decreased to $f_e \sim 0.06$ over the duration of a 1 ns laser pulse reasonably matches experimental measurements for direct-drive planar foil acceleration experiments [92], and similarly early time $f_e = 0.12$ and later time $f_e = 0.06$ for spherical implosions [78]. As the goal of this work is to assess nonlocal transport effects in the SNB model, relevant comparisons are constrained against HYDRA modeling with constant f_e flux-limited Spitzer-Harm heat conduction as opposed to exploring time-dependent sensitivities.

As the laser deposits energy into the material it ablates, a process in which the heated material expands and flows away from the surface. The ablation process initially is dynamic, before reaching a steady-state flow after some time. In the HYDRA simulations, this process is affected first by the rise-time of the laser-pulse (200 ps), and then a characteristic crossing time for the plasma to flow from the ablation region through the critical surface into the corona. This time is directly proportional to the incident laser intensity I_L, [93] and for 10^{15} W/cm^2 HYDRA simulations is on the order of a few hundred picoseconds, so the flow reaches a steady-state for $t > 0.5$ ns. For lower intensity cases, this process occurs quicker such that steady-state ablation occurs for the majority of the laser drive. The resulting steady-

state electron temperature and density profiles from various aluminum simulations at 10^{15} W/cm^2 laser intensity at $t = 1$ ns are shown in Figure 2.8. Differences here show the effect of the heat flux modeling upon the development of the ablation front. Various HYDRA-SNB configurations are shown, as well as two representative Spitzer-Harm cases with flux limiters $f_e = 0.03$ and 0.15.

First, we describe the local diffusion results, which span the range of Spitzer-Harm modeling. For $f_e = 0.15$, the heat flux arising naturally from the profile does not exceed the flux limit and effectively represents classical, unrestrained local diffusion. The electron-transport-dominated front is the largest, starting from the critical density $n_c \sim 8.9\times10^{21}$ cm^{-3} at $r \approx 500$ μm near the peak electron temperature of about 3 keV, and truncating at the onset of the radiation-dominated front at $r \approx$ 380 μm. In the coronal region, the persistent heat flow in the free expanding plasma produces a relatively flat temperature profile, i.e. the plasma expansion is nearly isothermal. In addition the strong heat fluxes help to relax the pressure gradients, and the resulting electron density profile is smooth across the dense plasma through the corona. In contrast, much sharper features are produced by highly restricted $f_e = 0.03$ Spitzer-Harm simulations. The electron-dominated ablation region is much narrower as the restricted heat flux cannot penetrate as far into the dense plasma, and region in the near-corona is also narrower as the restricted heat flow cannot relax the laser-generated pressure gradients, leading to a much sharper decompression near n_c. The laser-coupling is substantially reduced for $f_e = 0.03$ to 40%, in contrast to 97% energy coupling observed for $f_e = 0.15$. In the free expansion region, though absorption is smaller, the interplay of the laser-absorption with the more restrictive heat flux results in a much hotter corona of 4 keV. This temperature is consistent until $r \approx$ 750μm, after which the laser heating is insufficient and the expanding plasma begins to cool from PdV work. The rest of the Spitzer-Harm (f_e) simulations exhibit behavior that falls between these two cases in regards to the discussed temperature

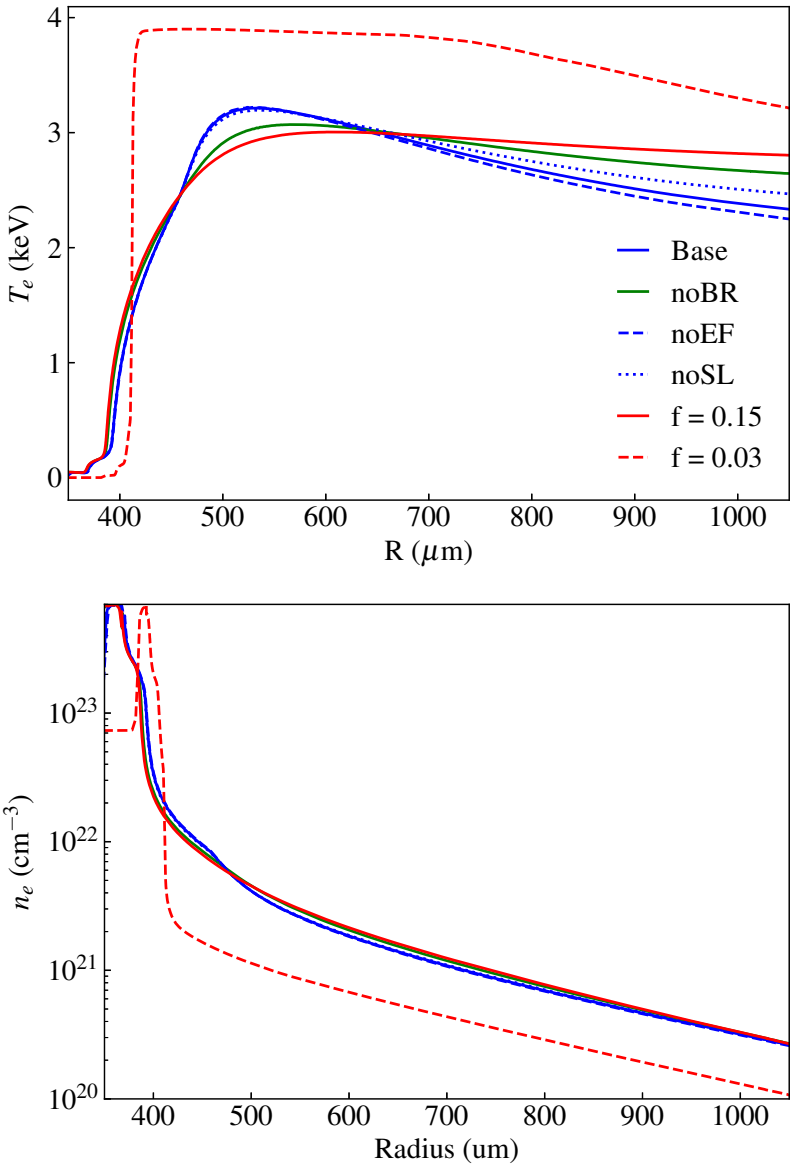

Figure 2.8: T_e (above) and n_e (below) plasma profiles from HYDRA Al-sphere simulations at 1×10^{15} W/cm^2 laser intensity and t = 1 ns fo HYDRA-SNB configurations as well as Spitzer-Harm thermal transport with flux limiters $f_e = 0.03, 0.15$. The nonlocal plasma cools more significantly as it expands, and has lower temperatures than those achieved in the $f_e = 0.15$ case (dashed black line) in the underdense corona.

and density conditions, as well as laser absorption.

Regarding HYDRA-SNB simulations, noBR-SNB is remarkably similar to the $f_e = 0.15$ Spitzer-Harm case, with similar T_e, n_e profiles and a slightly smaller absorption of 96%. For other SNB simulations, as previously discussed in Section 2.4.1, the observed

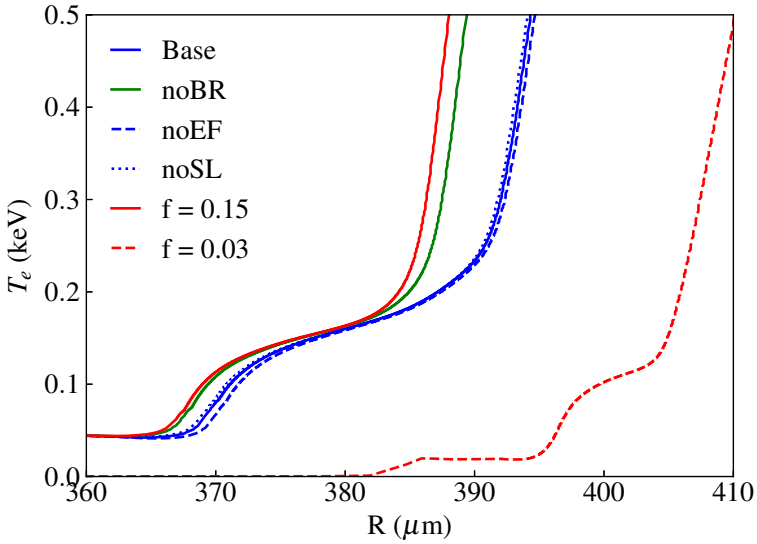

Figure 2.9: T_e profiles in the radiation-flux-dominated region of the ablation front for HYDRA aluminum-spheres at 1×10^{15} W/cm^2 laser intensity and t = 1 ns for HYDRA-SNB configurations as well as Spitzer-Harm thermal transport with flux limiters $f_e = 0.03, 0.15$. The HYDRA-SNB temperature front is hotter than that achieved with $f_e = 0.15$ Spitzer-Harm simulations.

heat fluxes are reduced in the electron-dominated region, which manifests a cooler, narrower temperature front compared to the $f_e = 0.15$ case. Similarly, the reduction in heat flux leads to a slight decompression feature near the critical surface, so n_e in the expanding plasma is similar to slightly restricted Spitzer-Harm simulations. The HYDRA-SNB simulations produce hotter peak coronal temperatures of ~ 3.2 keV, and reduced laser coupling of 92%. In the free expansion region, the restricted heat flux again leads to cooling as the plasma expands, similar to the $f_e = 0.03$ case. However, because this is cooling behavior coupled to both higher heat fluxes and laser-coupling in the near-corona, the temperatures at large distances are cooler than those observed from the range of Spitzer-Harm modeling. Here, noBR-SNB heat fluxes produce the hottest nonlocal expanding plasma, while noEF-SNB heat fluxes produce the coldest.

Recall that in Figure 2.2 the radiation-dominated region begins where the radia-

tion strongly couples to the plasma, as evidenced by the confluence of the electron and radiation temperatures. A closer inspection of the temperature that region is given in Figure 2.9, which is also where preheating was observed from SNB and K2 heat fluxes in Section 2.4.1. Despite the fact that heat fluxes are lower in the electron-dominated region, the low-foot radiation temperature front produced from SNB simulations is both longer and hotter than the $f_e = 0.15$ case, peaking at about 200 eV and 160 eV, respectively. This front appears to be enhanced by the nonlocal preheating, which enables higher energy transport from hotter regions up the temperature gradient. While again noBR-SNB is very similar to the $f_e = 0.15$ case, the slightly hotter radiation front also highlights this effect. Finally, the temperature achieved in the $f_e = 0.03$ case indicates this result is beyond the range of local diffusion modeling.

These findings are consistent in the broad array of HYDRA simulations across the range of materials and laser intensities under consideration in the present work. At 5×10^{14} W/cm^2 laser intensity, trends similar to those observed in the 1×10^{15} W/cm^2 cases are observed, while at the lowest intensity the plasma conditions enable mostly local diffusion, and simulations with different electron-transport modeling are largely the same with the exception of more restrictive values ($f_e < 0.05$) flux-limiting. Amongst materials, the biggest difference in the laser-coupling is observed in beryllium simulations where the absorption decreases from 93% ($f_e = 0.15$) to 81% (SNB) for the highest laser intensity case. At lower laser intensities, inverse-bremsstrahlung laser absorption is near order unity unless f_e is small. With respect to plasma density and laser absorption, we find that $f_e = 0.07 - 0.09$ Spitzer-Harm reasonably matches the range of laser-coupling and electron density profiles produced with the nonlocal transport model, which correlates with the range of f_e from previous work [92][78]. However, again we emphasize that no treatment of Spitzer-Harm transport can replicate the cooler coronal electron temperatures.

2.5 Implications for Experiments

In laser-plasma experiments, diagnostics cannot yield data needed to reproduce plasma conditions *vis-a-vis* simulation outputs. Rather, the appropriate experimental observables must be identified. Experimentally, coronal electron temperatures and densities can be determined by time-resolved optical Thomson Scattering diagnostics [94] placed at the appropriate radial position to probe the coronal density and temperature conditions. Once the laser-ablation front reaches a steady state, the free expansion of the irradiated plasma can be reasonably approximated as a self-similar isothermal rarefaction in spherical geometry, for which the density profile is described as $n_e(r) \sim \exp(-r/L_{n_e})$, where the density gradient scale length $L_{n_e} = c_S t/\sqrt{3}$ with plasma sound speed $c_S \propto (ZT_e/M)^{0.5}$ [95]. At 10^{15} W/cm^2, c_S ranges from 350-400 μm/ns for the different materials. The corresponding plasma scale length is $L_{n_e} \sim 200$ μm at $t = 1$ ns, and so a probe placed 600 μm (three inverse e-foldings) away from the initial outer radius ensures the simulated measurement probes electron densities below $0.1n_c$, i.e. in sufficiently underdense plasma where the 351 nm driving laser does not signficantly couple to the expanding plasma. For spheres at lower laser intensities, it may be required for the probe position to be closer to the sphere due to lower coronal temperatures.

Figure 2.10 shows the inferred T_e values at a probe placed 600 μm from the initial sphere ($r = 1030$ μm) over time for beryllium, aluminum, and copper at both 5×10^{14} W/cm^2 and 1×10^{15} W/cm^2 laser intensities. The electron densities are not shown here, but we note they fall between $0.01n_c - 0.1n_c$ at this position. The low-density tail of the plasma reaches the probe position at about the same time for simulations of different laser intensities, corresponding to when a temperature is detected by the probe. The red-shaded regions encompass the possible probe temperatures from Spitzer-Harm modeling, with the lower boundary representing the $f_e = 0.15$ results and upper boundary representing the $f_e = 0.03$ results. The blue-shaded

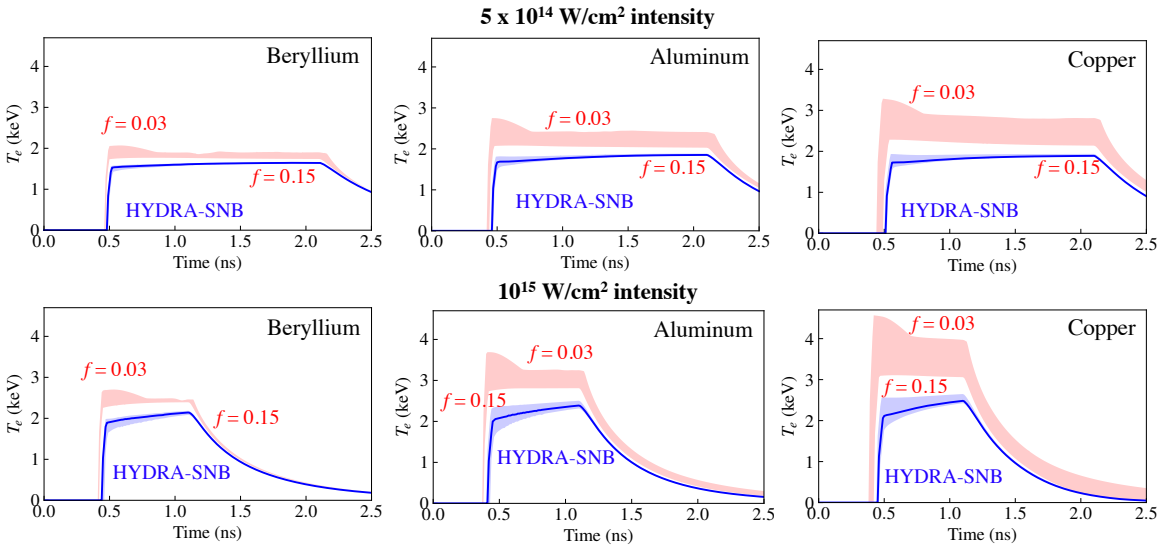

Figure 2.10: Inferred time-dependent coronal T_e from HYDRA sphere simulations driven by 5×10^{14} W/cm^2 (top) and 1×10^{15} W/cm^2 (bottom) laser intensities, taken at position $r = 1030$ μm for beryllium, aluminum, and copper. The red, shaded region encompasses the range of flux-limited Spitzer-Harm modeling with $f_e = 0.03 - 0.15$, while the blue-shaded encompasses the range of coronal temperatures observed between the Base-, noBR-, and noEF-SNB variations. HYDRA-SNB coronal electron temperatures are consistently cooler than their Spitzer-Harm counterparts, suggesting that no value of flux-limited Spitzer-Harm can match SNB for these systems.

regions encompass probe temperatures from HYDRA-SNB, which are distinct from Spitzer-Harm modeling, with the singular blue line representing Base-SNB HYDRA simulations.

Pivoting towards the ablation region, the hotter thermal front in aluminum and copper laser-irradiated spheres can be inferred by measuring the emitted radiation power. In simulations for the mid-Z materials, a non-negligible fraction of the absorbed laser energy is re-emitted as radiation, in contrast to the lower-Z beryllium where only 5% of the absorbed laser energy is converted. Some of the laser light absorbed in the corona is converted into X-rays, which radiates equally into the dense plasma and out into the corona region. In the ablation region, X-rays are also produced in the electron-dominated front, but the plurality of the radiative flux consists of a strong thermal contribution from the lower temperature radiation front where the

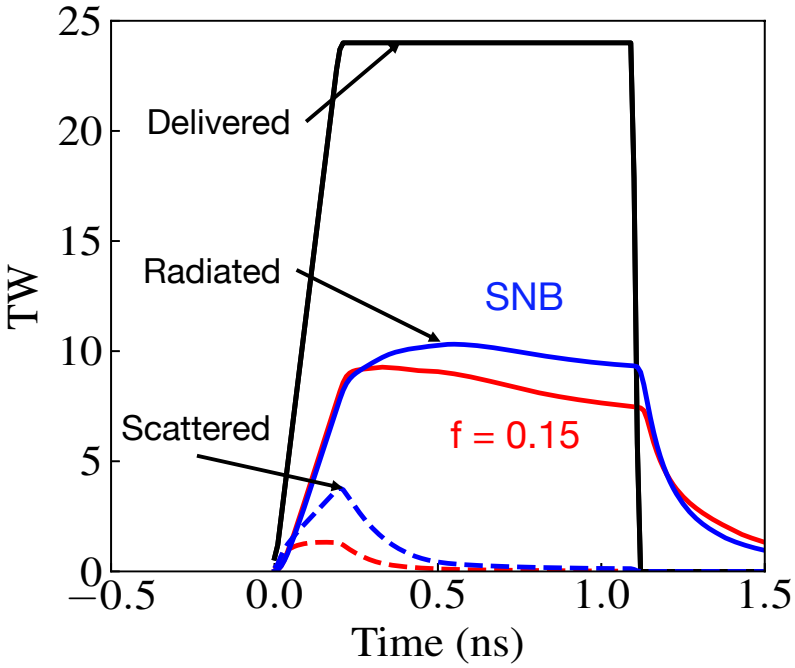

Figure 2.11: Emitted X-ray power (solid lines) and scattered laser power (dashed lines) vs. time for copper sphere simulations at 1×10^{15} W/cm^2 laser intensity for $f_e = 0.15$ (red) Spitzer-Harm transport and Base-SNB (blue) HYDRA simulations for the 24 TW square pulse (black line). The x-ray flux from the SNB nonlocal model is greater (∼10 Terawatts) than X-ray emissions with Spitzer-Harm electron transport modeling (∼7.5-9 Terawatts).

material and radiation temperature are strongly coupled. As HYDRA-SNB simulations produce a hotter thermal front due to the electron preheating, the total emitted radiative power is increased. Figure 2.11 shows the total emissions and laser scattering over time for copper at 10^{15} W/cm^2 laser intensity for the Base-SNB and f = 0.15 Spitzer-Harm thermal conduction models, illuminated by the 1 ns, 24 TW peak power square pulse. The emitted power from the $f_e = 0.15$ simulation is the largest possible radiation flux obtained from Spitzer-Harm modeling, starting at 9 TW and reducing to 7.5 TW right before the end of the pulse. In contrast, the HYDRA Base-SNB simulation presents larger radiation heat fluxes (about 10 TW throughout the pulse duration) than the range of Spitzer-Harm modeling.

In addition to HYDRA simulations with polar S_N radiation transport, we also performed HYDRA simulations using flux-limited radiation diffusion. Coronal elec-

tron temperatures and densities are similar between polar S_N and radiation diffusion methods, and the observed reduction in coronal electron temperatures due to nonlocal thermal conduction is consistent. Differences in the plasma evolution between these HYDRA simulations emerge in the size and temperature of the radiative front, and these differences propagate to the emitted radiation flux. Figure 2.12 shows the corresponding X-ray conversion efficiency η_{CE} for copper as a function of laser intensity for Spitzer-Harm with $f_e = 0.15$ and Base-SNB electron conduction models, as well as for polar S_N radiation transport and flux-limited radiation diffusion. The conversion efficiency η_{CE} is defined as (P_R/P_{abs}), where P_{abs} is the absorbed laser power, and P_R is the emitted X-ray power. Here, all values are calculated at t =1 ns. In HYDRA simulations with S_N, η_{CE} is 10% larger when compared to HYDRA simulations with radiation diffusion. However, we note that independent of the radiation transport approach the trend towards increased emissions with the SNB model is consistent. This effect is more significant with increasing laser intensity. Similar behavior is observed in aluminum sphere simulations: At 1×10^{15} W/cm^2 laser intensity and with multigroup radiation diffusion, $\eta_{CE} \sim 30\%$ and 25% for SNB and SH electron conduction (at 1×10^{15} W/cm^2). From S_N transport simulations, $\eta_{CE} \sim 20\%$ and 16%, respectively, for the reduced-nonlocal and classical electron conduction models.

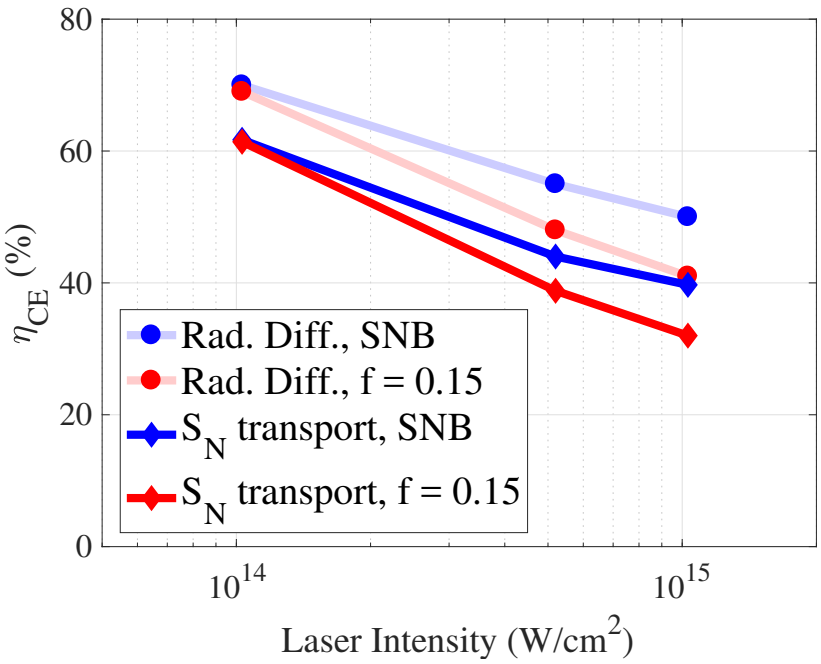

Figure 2.12: Conversion efficiency $\eta_{CE} = P_R/(P_{laser} - P_{backscatter})$ vs $\log_{10}(I_L)$, for copper spheres modeled with the Base-SNB (blue) and $f_e = 0.15$ Spitzer-Harm (red) thermal transport models, and with multigroup radiation diffusion (light lines) and S_N radiation transport (dark lines) models. With increasing laser intensity, nonlocal electron transport simulations exhibit higher conversion efficiencies than Spitzer-Harm simulations, independent of the radiation transport method.

2.6 Discussion

Close agreement between the maximum K2-VFP and SNB heat fluxes is observed in the near-corona at densities close to n_c. This is encouraging, as the heat flux in the this region influences the temperatures and densities that develop, and subsequently affects the laser coupling to the plasma. This finding is also evidenced in the inline temperature evolution test in Section 2.4.2, where the resulting plasma temperatures at electron densities close to critical are very similar between SNB and kinetic predictions. In addition, peak heat flux predictions of noBR-SNB against other SNB variations corroborate the effect of improvements suggested by Brodrick et al [2], though improvements from the adjustments suggested by Sherlock et al. [62] were not observed in radiation hydrodynamics simulations.

In the ablation front, preheat is predicted by K2-VFP simulations in the form of an advancing heat flux intruding into the radiation-dominated region from the electron-dominated region. In comparison, the SNB preheat is smaller and less penetrative into the radiation-dominated region. This preheat feature occurs because heat carrying electrons in the range of $3.7v/v_T$ from this area stream through the lower-density plasma into the denser, more collisional plasma within the radiative front. For example, consider the delocalized electrons originating from the depletion region in heat flux distribution shown in Fig. 2.4(a) at $r = 450$ μm, corresponding to a plasma temperature of 13.7 keV. Using equation 2.8 and local plasma conditions, $\lambda_{ei} = 15.8$ μm at this location, and reduces to 6 μm once the electrons reach the plasma conditions in the radiation front at $r = 430$ μm. This process is a continuous cascade, with faster electrons depleting from hotter regions and accumulating in cooler regions, as indicated by the shape of the heat flux distribution in Fig. 2.4(b). The net result is an accumulation of high-velocity electrons in low-temperature foot as indicated by the heat flux distribution in Fig. 2.4(b). In SNB, the EDF is not explicitly considered enroute to the calculation of the electron heat flux. However, Sherlock et al. [62] demonstrated that f_1 can be inferred from SNB such that the heat flux distribution $f_1 v^5$ can be reconstructed. In previous work, $f_1 v^5$ was shown for a simple-heat bath problem, with the K2 kinetic heat flux being carried by higher-velocity electrons relative to SNB. This behavior is a possible explanation for the smaller SNB preheat feature observed in Section 2.4.1, as lower velocity electrons will not penetrate as far into the radiation-dominated region. HYDRA-SNB simulations indicate that the additional electron heating into the radiation-dominated region results in a hotter radiative front, and subsequently the electron heat flux is recycled into higher self-emissions than those obtained with Spitzer-Harm modeling. This increased emission from HYDRA-SNB simulations occurs despite lower laser-coupling (as the peak heat flux is restricted). As the K2-VFP preheat feature is even larger, it is possible that

the radiative emissions would also be higher if a HYDRA-VFP simulation were to be undertaken.

From previous work comparing the SNB model to kinetic codes, a number of corrections emerged [2][62], which were considered in this work by the different variations used in HYDRA-SNB simulations. One intention of these corrections was to reduce coronal heat fluxes, which is corroborated in this work by noEF-SNB (which neglects $\mathcal{E}$, carries separate mfps for λ_{ei} and λ_{ee}, and includes ξ and $r = 2$) consistently predicting the lowest coronal heat fluxes. It should also be noted that in the present work, differences in coronal heat fluxes are the only major distinction between the noEF, noSL, and Base-SNB variations. However contrary to previous findings, here it is observed that SNB generally underpredicts coronal heat fluxes, such that these adjustments give rise to greater disagreement with kinetic modeling. Presently, it is unclear why coronal heat flux results between SNB and VFP disagree with previous findings, and for this problem the general observed trend with present modifications to λ_{ei} and λ_{ee} imply that a simultaneous agreement of these two regions with the K2-VFP calculations is not achievable. These disagreements are considered in the potential Thomson scattering measurement in Section 2.5, and despite the broadening of the range of nonlocal temperatures at the probe position the result is still distinct from Spitzer-Harm simulations. Alternatively, it is possible that a better heat flux prediction would be facilitated by definitions of λ_{ei} and λ_{ee} that differentiate between ablative and coronal plasma conditions. However, such an approach could also make SNB more problem-dependent.

A natural extension of this work would be to include 2D/3D effects which may affect the thermal transport. It is likely 2D/3D effects will present in the plasma corona near n_c. In addition to delocalization by fast electrons escaping the bulk temperature gradient, thermal conductivity is also reduced by much smaller temperature perturbations if λ_{ei} for heat-carrying electrons is long relative to the perturbation wavelength

k. In the corona, this behavior could emerge from a reduced collisionality in the low-density plasma ($\lambda_{ei} \propto n_e^{-1}$), such that the thermal transport may be inhibited even if λ_{ei}/L_T is not large. It is important to emphasize that the ability of SNB to reproduce this behavior has been assessed against kinetic codes [2] in the Epperlein-Short test [52]. In 1D, the temperature profile is fairly smooth, but in 2D/3D radiation-hydrodynamic simulations, temperature perturbations that affect the heat transport prediction could emerge from non-uniformities in laser illumination due to the beam overlap geometry. An additional asymmetry results from the stalk used to hold the sphere for the duration of laser heating [87], which necessitates dropping of beams in its proximity leading to an inherently 3D temperature map (though the temperature profile opposite of the stalk is well represented by 1D simulations). Cumulatively, these 3D temperature asymmetries could seed the growth of magnetic fields in the plasma corona from non-parallel T_e and n_e gradients via the Biermann battery effect, though recent work in similar conditions indicated this additional magnetic effect on the heat transport is minimal. [87]

As the intention of this work is to focus on the electron transport modeling, the effects of laser-plasma interactions (LPI), namely of two-plasmon decay (TPD), stimulated Raman scattering (SRS), and stimulated Brillouin scattering (SBS), were not considered. In regards to TPD, a practical intensity threshold was previously introduced [70], given here as $5 \times 10^{15} T_{e,KeV}/(L_{n,\mu m}\lambda_\mu)$ W/cm^2, where L_n is the electron density gradient scale length, and λ_μ is the laser wavelength in microns. Using copper plasma conditions from 10^{15} W/cm^2 HYDRA simulations at $t = 1$ ns at $0.25 n_C$ density ($T_e = 3.2$ keV, $L_n = 100$ μm), we calculate $I_L \sim 4.5 \times 10^{14}$ W/cm^2, meaning that TPD is likely to emerge at the higher end of laser intensities considered in this study. In practice, SRS is mitigated by smoothing spectral dispersion [96], but could also be present in these laser-plasmas. Generally, this class of LPI producing hot electrons can be disregarded due to the geometry of the solid laser-sphere and

the relevant observables, as long mean-free-path electrons do not affect conditions in the collisionless coronal plasma, and do not substantially affect the preheat feature provided that the total energy of the high-energy electrons population is not large. However, reduced laser coupling due to SBS enabling cross-beamed-energy transfer (CBET) has been shown to reduce laser-coupling to the sphere as potentially absorbed laser energy is transferred to outgoing scattered beams [87][79]. The reduced laser coupling could lead to a cooler overall plasma with less steep temperature gradients, reducing the observed nonlocal effects. This lower laser absorption could be accounted for by modulating the laser-drive profile in simulations, and of course more fully with the inclusion of an inline CBET model [97][98] or alternatively with a complimentary study of CBET effects using a laser ray-tracing code, which should be the subject of future investigation.

Nevertheless, the present work clearly demonstrates changes in the plasma and correlates them to aspects of the nonlocal transport differing from Spitzer-Harm modeling. In the far corona the expanding plasma is largely decoupled from the incoming laser, and reduced heat fluxes would still enable a cooler free-expanding plasma, regardless of LPI effects at densities near n_c to the emergent plasma. It is also worth highlighting the higher emissions observed in moderate-Z materials, owing to the secondary interaction of the electron preheat with radiation transport in the ablation region. This coupling effect may be strongest in mid-Z materials where the electron and radiative fluxes are most comparable [46]. In addition, though CBET is still present its impact may be mitigated at mid-Z due to the higher inherent efficiency of IB absorption.

2.7 Conclusions

In summary, this work assesses the effect of electron transport in the laser-irradiated sphere with a series of rigorous comparative studies, first between the SNB model with

various corrections and K2 kinetics predictions, and then between the various SNB configurations and Spitzer-Harm local diffusion in HYDRA radiation-hydrodynamics simulations. This study represents the first suite of integrated modeling comparisons of these corrections, which were previously benchmarked in simplified profiles relevant to hohlraum modeling. Stationary profile comparisons between HYDRA-SNB and K2-VFP show that the SNB model that incorporates corrections from Brodrick [2] provides reasonable agreement with K2-VFP predictions, reducing heat flux errors to from 40% to 10% at the highest laser intensity of 10^{15} W/cm^2. In the preheat region SNB underpredicts the preheat compared to K2-VFP, while in the coronal region the SNB heat fluxes are too strongly inhibited. However, a temperature evolution test between the K2-SNB and K2 Fokker-Planck heat fluxes indicates the effects resulting from these heat flux discrepancies on the temperatures in the plasma corona is small.

Three different aspects of nonlocal transport arise in the laser-irradiated sphere: the maximum electron heat flux is reduced (historically, this is addressed with flux-limited Spitzer-Harm), the heat flux at the interface between the electron-heat-flux- and radiation-heat-flux-dominated regions is enhanced by preheat, and the heat flux in the free expanding low-density coronal plasma is reduced. From HYDRA radiation-hydrodynamics simulations, it is observed that in the free-expanding coronal the reduced heat fluxes produce a cooler plasma than the range of Spitzer-Harm modeling, which can be directly measured with a Thomson Scattering diagnostic. And in the dense plasma, the preheating enhances energy transport towards the high-density, low-temperature radiation-dominated front, resulting in higher emitted radiative fluxes than the range of Spitzer-Harm modeling. For mid-Z spheres, it is proposed that the preheating within the radiation-dominated region could be assessed with measurements of the radiative emissions. Both of these effects in the laser-irradiated sphere can and should be tested by experiments.

CHAPTER III

Laser-Irradiated Spheres II: The Effect of Non-Maxwellian Electron Distributions on Laser-Plasma Radiation Emissions

3.1 Abstract

In this chapter, studies of laser-irradiated spheres are extended by considering the effect of non-Maxwellian electron energy distribution functions (EEDFs) on the predictions of non-local thermodynamic equilibrium (NLTE) collisional-radiative atomic kinetics, and subsequently on the calculated radiation transport and radiative spectra emergent from the laser-irradiated sphere using Cretin. To accurately consider non-Maxwellian electron distributions, Cretin calculations use a fully discretized representation of the EEDF for computing the ensemble-averaged atomic rate coefficients required to calculate the plasma charge state balances, radiative emissivities and radiative opacities. Cretin simulations are performed for both uniform (0D) plasma conditions and 1D HYDRA profiles with radiation transport. For 1D calculations, non-Maxwellian electron distribution information is taken from K2 Vlasov-Fokker-Planck (VFP) kinetic simulations of HYDRA plasma conditions to assess the effect of nonlocal electron heat transport, and from analytical Langdon distributions in the plasma corona to assess the effect of collisional laser absorption. From these studies,

it is found that non-Maxwellian electron distributions affect K-shell line emissions with the largest increases in the most intense $K-$shell features ($+10\%$) from Langdon distributions driven by collisional laser absorption, but do not strongly impact the total radiative flux ($<1\%$) from the laser-irradiated sphere. These changes in the radiation spectra and integrated flux from non-Maxwellian electrons are smaller than the changes that emerge from the different heat fluxes predicted from a nonlocal electron heat transport model.

3.2 Introduction

In radiation-hydrodynamics modeling of plasmas, the electron and ion species are assumed to have Maxwellian particle velocity distributions. However, many plasmas have non-Maxwellian electron distributions, which influences their radiative properties, and may also affect their energy transport and evolution. In the laboratory fusion efforts, evidence of non-Maxwellian electrons have been observed in tokamaks [99], laser-plasmas [100][101], and pulsed-power generated plasmas [11][102]. In laser-driven inertial fusion, excessive suprathermal or "hot" electrons are generated that can preheat the fusion fuel, hindering the efficient compression of the fusion fuel capsule. And in tokamaks, hot electron tails may runaway which can affect the stability and control of the confined plasma and also damage the experimental facility [103]. On the other hand, in fast-ignition schemes hot electrons are a strong candidate for igniting fusion fuel [104][105]. Clearly, non-Maxwellian electrons are impactful in many laboratory plasma systems, and it is worthwhile to study their effects.

Accordingly, this study extends on the work in Chapter II by assessing the effect of non-Maxwellian electron distributions on the radiative properties of the plasma in the laser-irradiated sphere. In laser-plasmas irradiated at these laser intensities, non-Maxwellian electrons come from three sources: from inverse-bremsstrahlung laser heating in the plasma corona [68], from additional laser-plasma interactions [106],

and from non-classical electron heat transport [60]. A complete consideration of these non-Maxwellian effects involves the simultaneous coupling of a kinetic electron VFP model with a collisional-radiative atomic-kinetics model with a relativistic particle-in-cell code, all inline within a radiation hydrodynamics code. Presently this approach is unviable. Instead, an *a posteriori* hybrid-approach is used, where radiative emissions are calculated with the atomic-kinetics code Cretin from HYDRA plasma conditions with the inclusion of discretized non-Maxwellian electron energy distributions. Descriptions for these discrete distributions are taken from either K2-VFP kinetic calculations (to consider nonlocal transport) or from analytical theory (to consider inverse-bremsstrahlung laser heating).

First, an expanded description of various sources of non-Maxwellian electrons in laser-plasmas is given in section 3.3. For completeness, this section also includes a description of LPI mechanisms that produce non-Maxwellian electrons, though they are not considered in this study. This is followed by a description of the models and codes in section 3.4. Simulation results are shown in section 3.5, first from 0D Cretin calculations of a couple of laser-plasma conditions, and then from 1D Cretin calculations of various laser-irradiated spheres illuminated with irradiances $I_L = 10^{15}$ W/cm^2. Section 3.6 provides a discussion of the study results. Finally, conclusions are given in section 3.7.

3.3 Non-Maxwellian Electrons in Laser-Plasmas

3.3.1 Super-Gaussian Energy Distribution Functions from Collisional Absorption

At the laser intensities below the relativistic threshold where collisionless absorption dominates ($[I_L \cdot \lambda_\mu^2] < 10^{17}$ W/cm^2) [107], the primary mechanism by which laser light transfers energy to a plasma is through inducing velocity oscillations in

electrons, which are then damped through electron-ion collisions, thereby transferring laser energy from the light to the plasma. This collisional process of laser photon energy absorption is known as inverse bremsstrahlung (IB) absorption [43]. In a plasma that absorbs laser energy through IB absorption, the influence of collisional absorption can distort the electron energy distribution function from a Maxwellian to a super-Gaussian of exponential order $m > 2$ [68][108], which is also referred to as a Langdon distribution. The resulting electron distribution function shape is dictated by both the rate of IB heating from electron-ion collisions ($\sim \nu_{ei} v_{os}^2$), which tends to produce a flatter electron distribution, and the rate of electron-electron collisions ($\sim \nu_{ee} v_{th}^2$), which acts to thermalize the electron distribution towards a Maxwellian. As $\nu_{ei} = Z\nu_{ee}$, the relative importance of IB heating to electron-electron collisions is characterized by the parameter

$$\alpha = Z\frac{v_{os}^2}{v_{th}^2}, \tag{3.1}$$

where Z is the plasma ionization, and v_{th} is the electron thermal velocity, and v_{os} is the electron oscillating velocity. Accordingly, the electron energy distribution is instead a super-Gaussian with exponent m, where m is solely dependent upon the parameter α, and is defined as

$$m = 2 + 3/(1 + 1.66/\alpha^{0.724}). \tag{3.2}$$

The corresponding electron velocity distribution function is

$$f_m(x, v, t) = C_m \exp\left[-\left(\frac{m_e v^2}{2k_B T_e} a_m\right)^{m/2}\right], \tag{3.3}$$

with coefficients a_m and C_m defined as

$$a_m = \frac{2}{3}\frac{\Gamma(5/m)}{\Gamma(3/m)}, \tag{3.4}$$

$$C_m = \frac{n_e}{4\pi}\left(\frac{m_e}{2k_B T_e}\right)^{3/2}\frac{m a_m^{3/2}}{\Gamma(3/m)}. \tag{3.5}$$

In the limit of $\alpha \ll 1$, then $m = 2$ and the distribution reverts to the Maxwell-Boltzmann distribution. In the limit of $\alpha \to \infty$, the distribution becomes a super-Gaussian with $m = 5$. Atomic kinetics calculations consider the electron density distribution in energy space as opposed to velocity space. From Equation 3.3, the equivalent energy distribution with respect to the electron energy $E = \frac{1}{2}m_e v^2$ is is taken from imposing the equivalence $f_m d^3v = 4\pi v^2 dv \equiv f_{m,E} dE$, which yields

$$f_{m,E} = \frac{4\pi}{m_e^{3/2}}\sqrt{2E}\; C_m \exp\left[-\left(\frac{E}{k_B T_e}a_m\right)^{m/2}\right]. \tag{3.6}$$

As is shown later in Section 3.5.1, α and m from Equations 3.1 and 3.2 can be calculated using local plasma conditions from radiation-hydrodynamic simulations, and Langdon distributions can then be defined with Equation 3.6.

3.3.2 Nonlocal Heat Transport

In kinetic simulations of fusion-relevant laser-plasmas it was found that the diffusion approximation ($f_0 + f_1$) is sufficient for modeling nonlocal electron transport in these conditions [59][60]. These studies demonstrated that the nonlocal heat flux, which is dependent upon the asymmetric component of the electron distribution f_1, is most affected by the deviation of the symmetric component f_0, which is Maxwellian in the limit of small gradients. As $f_0 \gg f_1$, non-Maxwellian electron distributions develop coincidently with nonlocal deviations from Spitzer-Harm electron transport in the vicinity of steep temperature gradients in these laser-plasmas.

Precise kinetic distributions from radiation-hydrodynamics can be calculated from Vlasov-Fokker-Planck calculations with the K2 code. Procedurally, this approach is equivalent to the kinetic studies performed in the previous chapter. However in this study our interest is not in the heat flux, which relies upon the asymmetric first-order anisotropy f_1, but rather in the entire electron distribution function $f(E)$ whose shape is dominated by the zeroth-order symmetric component of the energy distribution, f_0.

3.3.3 Hot Electron Production from Laser-Plasma Interactions

Besides collisional absorption other absorption mechanisms affect how energy from the propagating laser light couples to the plasma. Generally speaking, modifications in the laser absorption behavior induced by these laser-plasma interactions (LPI) manifest in two ways: they can affect the total energy coupling in the laser-plasma system, and they can generate hot electrons. LPI processes that generate hot electrons do so by the excitation of electron plasma waves with large phase velocities, which can accelerate electrons to high energies through nonlinear Landau damping [109], or through electron plasma wave collapse [110][111]. From the laser light, electron plasma waves are excited during resonance absorption at the critical density n_c, and through the parametric instabilities two-plasmon decay and stimulated Raman scattering.

For resonance absorption, first consider an oblique light wave propagating towards a plasma with a density gradient. If the electronic vector of the light wave lies within the plane of incidence, then the light wave is p-polarized. In this orientation, the electric field is in the direction of the density gradient, and causes electrons to oscillate. At the critical density the plasma frequency is equivalent to the laser frequency ω_L, so the electron plasma wave with frequency ω_{pe} grows resonantly, which also enhances the laser absorption into the plasma.

The other two mechanisms are parametric three-wave processes, where an incoming light wave at the laser frequency resonantly decays into two waves [43]. In stimulated Raman scattering, the laser light wave decays into a scattered light wave and an excited electron plasma wave, i.e., $\omega_L = \omega_s + \omega_{pe}$. The stimulated Raman scattering process requires that $\omega_L \geq 2\omega_{pe}$, or alternatively $n_e \leq n_c/4$, meaning this process occurs at electron densities equal to or below quarter critical. Alternatively, for the two-plasmon decay (TPD) instability the laser light wave decays into two electron plasma waves or $\omega_L \simeq 2\omega_{pe}$, and so the growth of this instability is concentrated in the proximity of quarter-critical density.

3.4 Models and Methods

In modeling a physical system, a numerical approach must be chosen. This decision is inherently challenging. One must select a physical model to represent the behavior of interest, and this model must be validated. The model must be numerically discretized, which introduces numerical errors that can affect or even obscure physical processes core to the system's evolution. Even if the former two choices are soundly made, discrepancies in the initialization of a computational simulation with those of the experiment, as well as uncertainties from experimental observations and measurements must be quantified. And finally, it is important to state here that even if this is all done correctly, such descriptions and the computational codes that feature them do not supplant reality. Rather, often studied physical systems conveniently fit within the limits of one code and its descriptions. But if the problem of interest crosses multiple descriptions–like in this study–then multiple codes are required. This study employs three codes in its modeling: the HYDRA radiation-hydrodynamics code, the K2-VFP kinetic code, and the Cretin atomic-kinetics code. The specific roles as well as numerical details of simulations from each code are described next.

3.4.1 HYDRA Laser-Irradiated Sphere

The HYDRA laser-irradiated sphere model is equivalent to the system studied and described in the previous chapter. The sphere is uniformly irradiated by sixty 351 nm wavelength (3ω) beams, with intensity profile $I(r) = I_o e^{-\left(\frac{r}{r_o}\right)^n}$, where r is the profile radius in microns, $r_o = 358$ μm and $n = 5.2$. Only one laser pulse is considered, which is a square pulse with 200 ps rise time and 2 ns duration with peak intensity of $I_L \sim 1.03 \times 10^{14}$W/cm^2, equivalent to 24 terawatts of laser energy at maximum power. In this study four materials are considered for the 12.5 μm outer coating of the 430 μm radius solid, carbon-core sphere: copper (Z = 29) with mass density $\rho = 8.96$ g/cm^3, titanium (Z = 22) with mass density $\rho = 4.51$ g/cm^3, iron (Z = 26) with mass density $\rho = 7.87$ g/cm^3, and finally germanium (Z = 32) with mass density $\rho = 10.50$ g/cm^3. The radiation transfer equation is solved using a polar S_N (discrete ordinates) method [89]; this radiation transport approach is equivalent to that used in the Cretin atomic-kinetics code. The materials are modeled with tabulated equations of states from LEOS and TABOP local-thermodynamic equilibrium (LTE) opacities. In the hot, underdense corona the collisional-radiative model DCA [44] is employed to describe the non-LTE atomic kinetics, with transition temperature from LTE to NLTE at 100 eV. Requisite with the resolution requirements found in the previous chapter (see Appendix A), $900 - 1200$ Lagrangian zones are used in the simulation domain to ensure $< 2.5\%$ variation in the total energy deposited via laser absorption(see Appendix A for details regarding resolution and convergence). Simulations are performed using Spitzer-Harm thermal transport without flux-limiting, or with the SNB nonlocal transport model with the corrections suggested by Brodrick et al. [2].

3.4.2 K2-VFP

In this work, the Lagrangian Vlasov-Fokker-Planck (VFP) code K2 [62] is used to evolve the non-Maxwellian electron energy distribution functions using plasma conditions from HYDRA-SNB simulations with a frozen-flow approximation–meaning hydrodynamics do not heat or cool the electron energy distributions. Similarly, the effects upon the electron energy distribution by energy transport from radiation absorption and emission are not considered. While the electron energy distributions evolve through electron thermal transport, heating and cooling operators are simultaneously employed to maintain the mean kinetic energy for the distributions at each position, i.e., the temperature of the plasma does not change. The heating operator is of the Langdon form [68] analogous to laser heating, while for cooling a modified Langdon operator is used that tends to shift the energy distribution towards a Maxwellian. In these K2 kinetic calculations, only the f_0 and f_1 spherical harmonics are considered.

K2-VFP simulations are initiated with a 1000 cell uniform grid on which plasma conditions from HYDRA simulations are interpolated. This interpolation is truncated in the expanding coronal region at $n_e = 0.005 n_c$, which excludes some of the hot, underdense corona. This is done to reduce the spatial range of interpolation to enable better resolution of the denser, cooler parts of the laser-ablation front, and does not affect the kinetic calculation. The electron energy group is discretized into 180 groups uniform in velocity space, with maximum velocity $v_{max} = 6 \times v_{th}$, or equivalently with $E_{max} = 36 \times E_{th}$ where E_{th} is the electron energy at the thermal temperature. The numerical time step is shorter than the electron-ion collision time, and is typically a few femtoseconds for these simulations. In the plasma, the electron distributions are evolved until they reach the non-Maxwellian steady-state, which occurs in a few picoseconds.

3.4.3 Cretin

The non-local thermodynamic equilibrium atomic kinetics and radiation code Cretin [44] is used to calculate detailed radiative spectra from HYDRA plasma conditions. Cretin employs a collisional-radiative model for the treatment of atomic kinetics, which procedurally involves the calculation of transitional rates from both collisional and radiative processes. Once all the rate coefficients have been calculated, the atomic populations are evolved using the rate equation $\frac{d\boldsymbol{y}}{dt} = \boldsymbol{A}\boldsymbol{y}$, where $\boldsymbol{y}$ is a vector representing the population densities of each the atomic levels, and $\boldsymbol{A}$ is the rate matrix. Finally, these atomic populations are used to determine the charge state distribution and to construct the line and continuum emission spectra of the plasma. There is no atomic data inherent in Cretin, rather the specific information for electronic energy level structure and transition processes for each element of interest is specified in an external model. For the studies performed in this chapter, Cretin calculations use the DCA atomic physics model, which is equivalent to the model employed in HYDRA radiation-hydrodynamic simulations.

In the collisional-radiative approach, rate coefficients $\langle v\sigma \rangle$ for collisional processes such as excitation and ionization are integrated from the particle distribution as

$$\langle v\sigma \rangle = \int_{\Delta E}^{\infty} v\sigma(\epsilon) F(\epsilon) d\epsilon, \tag{3.7}$$

where v is the electron velocity, ϵ is the electron energy, $\sigma(\epsilon)$ is the energy-dependent collisional process cross-section, and $F(\epsilon)$ is the distribution function for electrons or ions. The reverse rates of de-excitation and recombination are calculated by enforcing detailed balance. The analogous radiative rates of photoionization and photoexcitation are calculated by integrating over the photon energy spectrum. Autoionizing levels are present and Auger decay rates are included as well. If $F(\epsilon)$ is a known distribution shape (e.g., Maxwellian) for a specific plasma temperature, then it can

be analytically expressed such that $\langle v\sigma \rangle$ is easily directly calculated. To represent deviations from a single Maxwellian, a simple extension is to utilize a bimodal (e.g., 2-temperature) energy distribution, where the secondary temperature component of the distribution function is represented with an appropriate Maxwellian with temperature T_h and density fraction f_h. The subscript $_h$ denotes *hot* as typically these approaches are used in the modeling of hot electron populations. However, this 2-temperature approach is inadequate in representing the electron energy distribution functions considered in this chapter, particularly in the plasma corona where the electron distributions actually have a deficit of higher-energy electrons. This behavior is observed both in the Langdon distributions and the electron distributions from K2-VFP kinetics calculations in this work. Instead, this study employs a fully discrete representation of the electron distribution function $F(\epsilon)$ in the calculation of various collisional rates in the atomic-kinetics calculations. Forward collisional rates for excitation and ionization are calculated from numerically integrating Equation 3.7 with the non-Maxwellian discrete representation for $F(\epsilon)$. In addition, detailed balance cannot be enforced for non-Maxwellian electron distributions [112], so reverse collisional rates for de-excitation and recombination must also be directly calculated from numerical integration. At the time of this writing, this utilization of discrete electron energy distributions represents a new capability in Cretin. Because a discrete representation of $F(\epsilon)$ introduces another source of numerical error in the calculation of collisional rates from Equation 3.7, a convergence study was performed to constrain our studies (see Appendix B).

3.5 Results

3.5.1 0D Cretin Calculations

First, we perform 0D Cretin calculations to assess the effect of non-Maxwellian distributions from different plasma conditions within the laser-irradiated sphere. These 0D calculations assume an infinite plasma uniform in defined intrinsic properties (e.g., density and temperature) and do not consider radiation transport. Figure 3.1a shows the plasma conditions and the laser intensity (T_e, T_i, T_R, n_e) from HYDRA radiation-hydrodynamics simulations of copper illuminated by a square pulse with 200 picosecond (0.2 nanosecond) rise time and nominal maximum laser irradiance of $I_L = 10^{15}$ W/cm^2 at time $t = 0.5$ ns. These conditions are identical to the highest laser intensity considered for copper-spheres in the Chapter II. The shaded regions correspond to the radiation-transport dominant ablation region, electron heat-transport dominant ablation region, and near coronal region where both electron-heat and laser-absorption energy mechanisms are comparably high. The plasma is in local-thermodynamic equilibrium (meaning the temperatures of the three species–ions, electrons, and radiation field–are equivalent) through the radiation-dominated front, beyond which the bulk radiation field largely decouples from the ablating plasma in the electron thermal transport dominated region while the electron and ion temperatures begin to diverge slightly due to decreased collisionality in the less dense plasma. In the coronal plasma, the electrons are heated by the laser, which further decouples their energy (and temperature) from the ion species. From this plasma, the absolute-integrated difference between the Maxwellian and non-Maxwellian EEDFs, crudely defined as

$$\delta = \frac{1}{2} \int |f_{MW}(E) - f(E)| dE, \tag{3.8}$$

where the energy distribution functions are normalized such that $\int f(E)dE = 1$, is shown in Figure 3.1b. The one-half factor outside the integral is written for con-

venience so that $0 < \delta < 1$. The quantity δ will also be colloquially referred to in terms of percentages. The largest differences in the electron distribution functions from K2-VFP predictions are in the near-corona at sub-critical electron densities, where δ is of order 10^{-2}, with local maximum of ~ 0.045 or 4.5% at the electron density of approximately $0.5 \times n_c$. Further inside the laser-irradiated sphere ablation front in the electron heat-transport dominated ablation region, the Maxwellian and non-Maxwellian distribution functions differ by 1-2 percent. Finally in the denser, radiation-transport dominated LTE region, δ is $\sim 10^{-3}$, smaller by an order of magnitude.

In addition to EEDF information from Vlasov-Fokker-Planck simulations, we can alternatively consider super-Gaussian EEDFs in the plasma corona due to collisional heating, where $f(E)$ is dictated by Equation 3.6. From HYDRA simulations, $\alpha = Zv_{os}^2/v_{th}^2$ can be locally defined by the plasma parameters. Here, the electron oscillation velocity is calculated in cgs units as $v_{os} = c \times \sqrt{I_{14}\lambda_\mu^2}/117$, where I_{14} is the laser intensity in units of 10^{14} W/cm^2, and λ_μ is the laser light wavelength in microns ($\lambda_\mu = 0.353$), and c is the speed of light [3]. The super-Gaussian exponent m for these Langdon distributions as well as the background laser intensity are also shown in Figure 3.1b, with the steepest Langdon distributions with $m = 2.73$ near the critical density, reducing to $m = 2.55$ at $0.1n_c$. This decrease in m is primarily due to the reduction in laser intensity with radius r, which is a consequence of the spherical geometry. However, as the attenuation of the laser intensity I_L in radial distance is more gradual than the reduction in $\frac{\partial T_e}{\partial r}$ corresponding to the electron heat flux from the steep plasma electron temperature profiles, more non-Maxwellian electron energy distributions and consequently higher δ is observed in the far-corona region due to inverse-bremsstrahlung absorption.

The first region considered in 0D Cretin calculations is in the electron-dominated ablation front at radius $r = 440\mu$m, indicated by the black-diamond marker in Figure

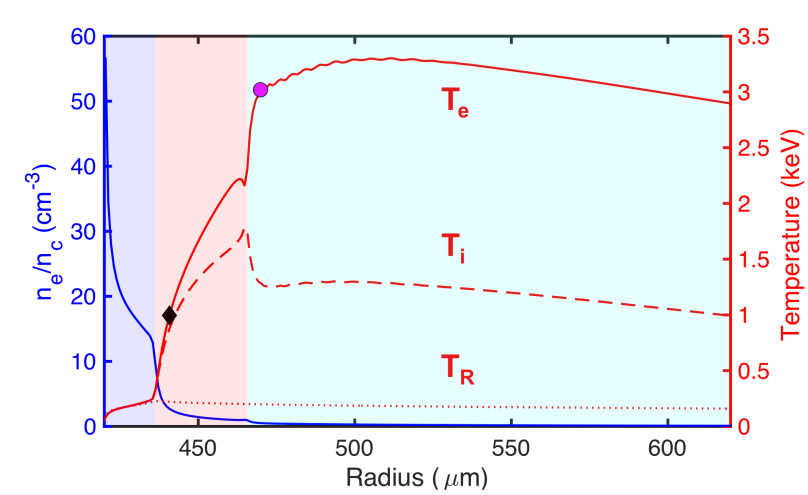

(a)

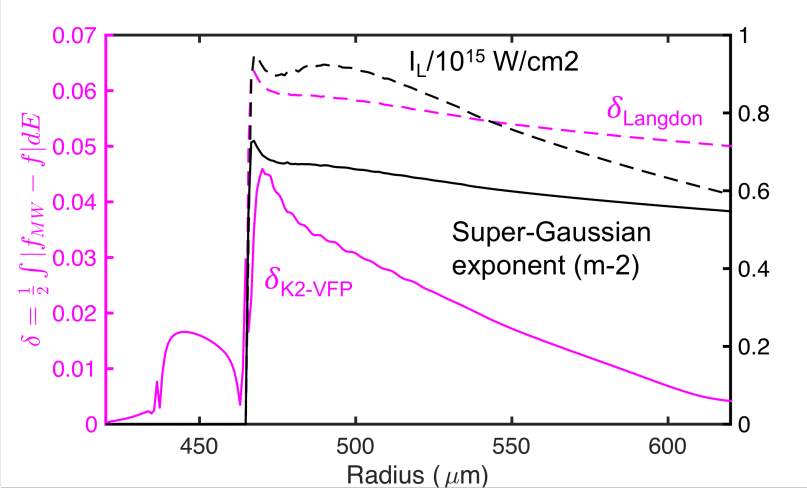

(b)

Figure 3.1: (a) Profiles of the electron, ion, and radiation temperature as well as electron density normalized by the critical density n_c for a copper sphere heated by a laser of irradiance $I_L = 1.03 \times 10^{15}$ W/cm^2 at time $t = 0.5$ ns. The shaded regions correspond to the radiation transport dominated front (blue), electron thermal transport dominated front (red), and the near coronal plasma out to $\sim 0.1 \times n_c$. The next panel (b) shows the corresponding deviation δ of the kinetic K2-VFP (magenta line) and Langdon super-Gaussian (magenta dashed) electron energy distribution functions from the Maxwellian distribution. For Langdon distributions, the spatial distribution of the laser distribution and super-Gaussian exponent m is also shown (black).

3.1a. Here the plasma electron and ion temperatures are $T_e = 995$ eV and $T_i = 875$ eV, and the radiative temperature T_R is 220 eV. The plasma electron density is $\sim 2.7 \times n_c$, with number densities of $n_e = 2.39 \times 10^{22}$ cm^{-3} and $n_i = 9.08 \times 10^{20}$ cm^{-3}, respectively,

for the electron and ion densities. With respect to the Maxwellian energy distribution for this position, $\delta = 0.0154$ or 1.54% from the kinetic K2-VFP distribution.

The Maxwellian and K2-VFP kinetics electron energy distributions are shown in Figure 3.2 as well as the difference between the distributions. Compared to the Maxwellian distribution, the kinetic distribution is narrower, with an increased population of electrons (1.1% higher) about the thermal temperature in electron energies up to 1500 eV. From 1500-6600 eV, the narrower kinetic distribution has a 1.5% deficit in electrons, and conversely has an enhanced population of hotter electrons in the high energy tail of the distribution of about 0.4%. This plasma condition from the electron heat-flux dominated region is downstream from the hotter coronal plasma. This surplus of electrons is due to the nonlocal accumulation of heat-carrying electrons from further up the temperature gradient. Subsequently, the deficit of moderate energy electrons and surplus of electrons with energies about the electron thermal velocity occurs in order to prevent an increase in the kinetic temperature from this electron distribution.

3.5.1.1 Electron-Dominated Heat Transport Ablation Front

In Cretin, atomic-kinetics calculations are initiated using HYDRA plasma conditions (T_e, T_i, T_R, n_i) and the electron energy distribution functions shown in Figure 3.2. The electron densities vary slightly with the average ionization of the plasma, which is calculated from the atomic population distribution that is obtained from solving the rate equation. For this case, the Maxwellian distribution is slightly denser with $Z = 25.92$, against $Z = 25.86$ from the non-Maxwellian energy distribution. Figure 3.3 shows the subsequent spectral emissivities produced from Cretin calculations for the Maxwellian and non-Maxwellian (K2-VFP) cases. The lines at photon energies < 2.5 keV, which are composed of emissions from $L-$ and $M-$shell transitions, are essentially the same between the Maxwellian and non-Maxwellian cases.

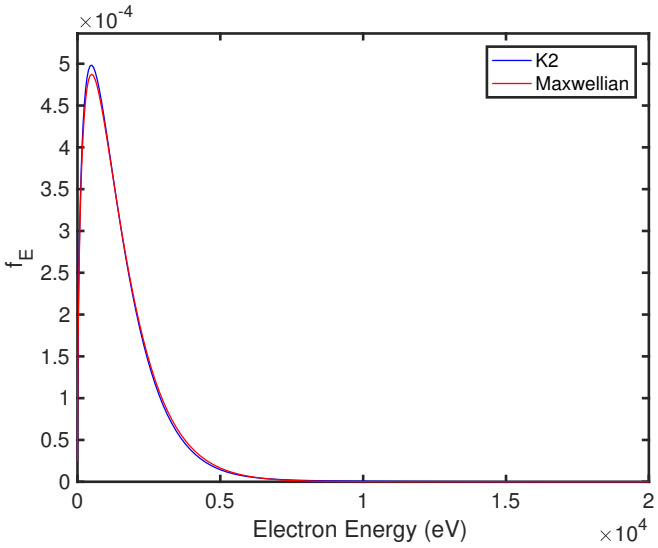

(a)

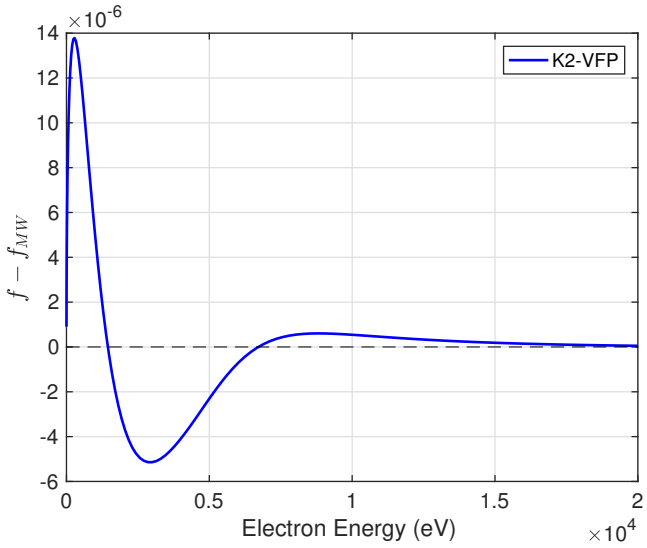

(b)

Figure 3.2: Electron energy distributions from Vlasov-Fokker-Planck calculations with the K2 code (blue) and from a Maxwell-Boltzmann distribution for a plasma with electron temperature of $T_e = 995$ eV, using HYDRA plasma conditions from position $r = 440\mu$m in Figure 3.1a.

Differences are observed at photon energies >8 keV, both in the continuum radiation and in the lines and features from the copper K-shell. The most intense K-shell feature from the higher-energy portion of the emissivity is shown in Figure 3.4(a), with the charge-state contributions shown in Figure 3.4(c). This K-shell feature is

composed of lines from $2-1$ (meaning L- to K-shell) transitions, and is dominated by lower isoelectronic (higher ionization) states, specifically with the higherest emissions from He-like, Li-like, and Be-like lines. Higher energy K-shell complexes and lines are shown in Figure 3.4(b), with again specific charge-state contributions shown in Figure 3.4(d). The complexes from $\sim$ 9500-10000 eV are due to $3-1$ ($M-$ to $K-$shell) transitions from the He-, Li-, Be-, and B-like charge states. At photon energies > 10 keV, most lines are from He-like transitions.

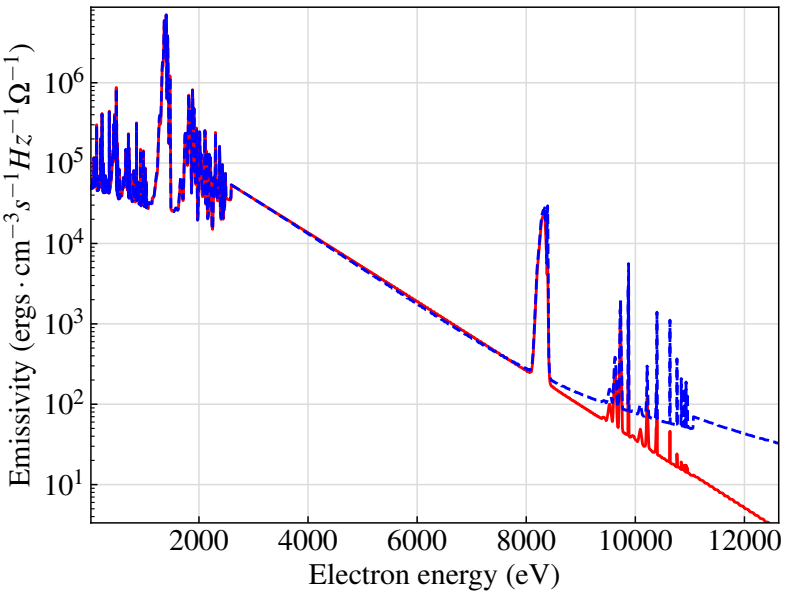

Figure 3.3: Emissivity spectra from Maxwellian (red) and K2-VFP (blue) electron energy distributions for electron temperature $T_e = 995$ eV for a copper plasma with ion density 9.08×10^{20} cm^{-3}, $T_i = 875$ eV and $T_R = 220$ eV.

Comparing the two distributions, it is evident that the K2-VFP kinetic EEDF enhances the intensity of K-shell emission features, especially for lines due to collisional excitations in He-like charge states. The intensity of lines and complexes (composed of multiple transitions) emitted from other charge-states is also enhanced, especially in the K-shell feature composed of $2-1$ transitions, where the local peak about the Li-like complex is 20% higher in the non-Maxwellian case. The changes in the intensity of these features is similar to changes invoked by a hot electron population.

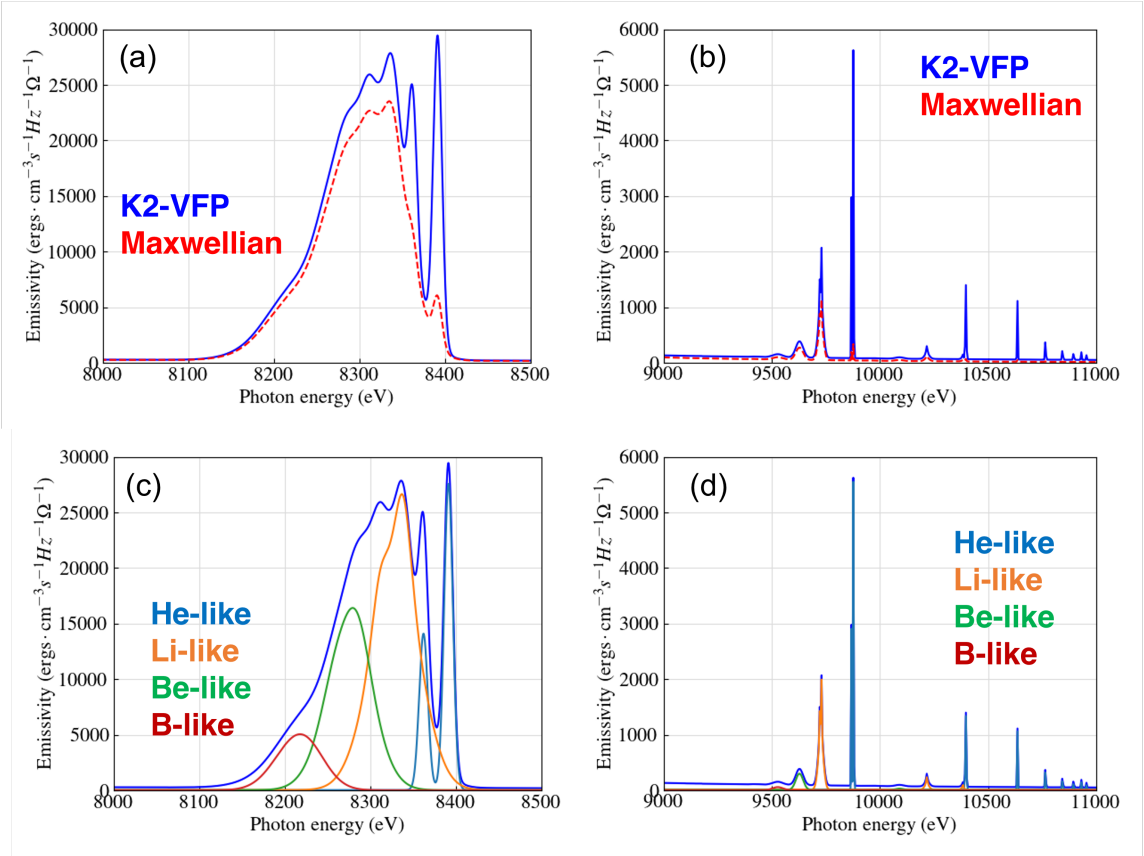

Figure 3.4: $K-$shell line emissivity spectra of a copper plasma from a Maxwellian (red) and K2-VFP (blue) electron distributions for electron temperature $T_e = 995$ eV with ion density 9.08×10^{20} cm^{-3}, $T_i = 875$ eV and $T_R = 220$ eV, from (a) photon energies between 8000-8500 eV and from (b) photon energies between 9000-11000 eV. This bulk $K-$shell feature is composed of line emissions from various charge states with emissions from (c) 2-1 transitions for photon energies 8000-8500 eV and (d) higher number shell transitions for energies from 9000-11000 eV.

This behavior is not entirely surprising as the K2-VFP electron distribution exhibits a surplus of electrons at energies higher than 6500 eV. The density modulations observed at lower energies in the electron distribution affect the $L-$ and $M-$shell transitions, which are $\sim$100 times more intense than those from the K-shell and thus have a stronger impact on the total emissivity. Considering the entire emission spectrum, the energy/frequency-integrated emission is 1.51 $\times 10^{23}$ ergs/s/cm^3 from the Maxwellian distribution. From the K2-VFP distribution the emission increases slightly to 1.56 $\times 10^{23}$ ergs/s/cm^3, and so in aggregate these density modulations in

the EEDF enhances the total emissivity of the plasma by 3%.

3.5.1.2 Sub-Critical Electron Density Laser-Plasma Corona

The second region considered is the hot, coronal plasma at sub-critical electron densities. Specifically, the plasma conditions considered here correspond to the magenta-circle marker in Figure 3.1a, at radius $r = 470\mu$m. Here, $T_e = 3013$ eV, $T_i = 1281$ eV and $T_R = 198$ eV. The plasma electron density is $\sim$0.5 $\times n_c$, with number densities of $n_e = 4.47 \times 10^{2\text{`}}$ cm^{-3} and $n_i = 1.67 \times 10^{20}$ cm^{-3} respectively for the electron and ion densities. For the K2-VFP kinetic distribution, $\delta = 0.045$. In addition, we also consider the super-Gaussian Langdon distribution produced by collisional laser absorption as described by Equations 3.4, 3.5, and 3.6. The super-Gaussian exponent m is calculated from local plasma conditions and the local laser intensity, found to be $m \sim 2.7$ here. With respect to the Maxwellian electron energy distribution, $\delta = 0.06$ from the Langdon electron energy distribution.

The electron energy distributions are shown in Figure 3.5, as well as the difference between these different populations. The general behavior of the non-Maxwellian distributions here are opposite to those observed from the K2-VFP energy distributions observed in the electron-ablation dominated region, with a deficit of electrons about the Maxwellian peak of $\epsilon_M \sim 1.5$ keV, a surfeit of moderate energy (2-7 $\times \epsilon_M$) electrons, and finally a dearth of electrons in the high energy tail. More specifically, for the K2-VFP distribution there are 1.7% fewer electrons at energies $\epsilon < 1700$ eV, 4.6% more electrons for 1700 eV $< \epsilon <$ 7800 eV, and 3% fewer electrons for $\epsilon >$ 7800 eV in the high energy tail. For the Langdon super-Gaussian distribution, there are 4.3% fewer electrons at energies $\epsilon <$ 2400 eV, 6.1% more electrons for 2400 eV $< \epsilon <$ 10500 eV, and 1.8% fewer electrons for $\epsilon >$ 10500 eV in the high energy tail.

Figure 3.6 shows the subsequent spectral emissivities produced from Cretin collisional-radiative calculations which consider the Maxwellian, K2-VFP kinetic, and Langdon

super-Gaussian electron energy distributions. In the high energy range of the spectra, it can be observed that both continuum emission and line emission from the $K-$shell are lower in the non-Maxwellian cases, with the greater reduction in intensity from various transitions from the K2-VFP plasma. This behavior is consistent with the larger deficit in the high energy tail of the K2-VFP distribution (3%) compared to the Langdon distribution (1.8%) observed in Figure 3.5b. Looking at the $2-1$ $K-$shell feature, both the He-like complexes centered at $\sim$ 8360 and $\sim$ 8390 eV from non-Maxwellian distributions are less intense, consistent with the behavior observed for higher energy lines. However, the Li-like complexes and complexes from other charge states are more intense from both non-Maxwellian EEDFs, with a greater increase from the Langdon distributions. The intensification of these lines is likely due to the increased population of moderately hot (relative to the thermal electron temperature) electrons. From these plasma conditions, the frequency-integrated total emission is 4.17 $\times 10^{21}$ ergs/s/cm^3 for the Maxwellian distribution, which is an order of magnitude smaller than the emissivity of the denser plasma. The emissivities corresponding to the kinetic and Langdon distributions are 4.03 $\times 10^{21}$ ergs/s/cm^3 and 3.99 $\times 10^{21}$ ergs/s/cm^3, corresponding to a 3.4% and 4.3% decrease respectively in emissions from the shape of these electron distributions.

3.5.2 1D Cretin Calculations

We now examine 1D Cretin calculations with conditions from the sphere laser-plasma profile, first calculating the rates, populations, emissivities and opacities for each 0D plasma state, and subsequently the emitted radiative spectra from the plasma by solving the radiation transport equation. We consider plasma conditions from HYDRA radiation-hydrodynamics simulations evolved with both the classical Spitzer-Harm (SH) electron heat conduction, and the nonlocal SNB electron heat transport model. Cretin simulations initiated with plasma conditions evolved with

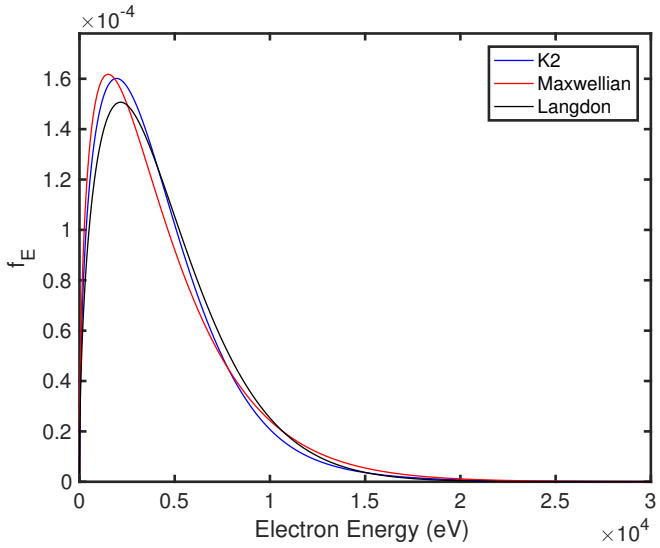

(a)

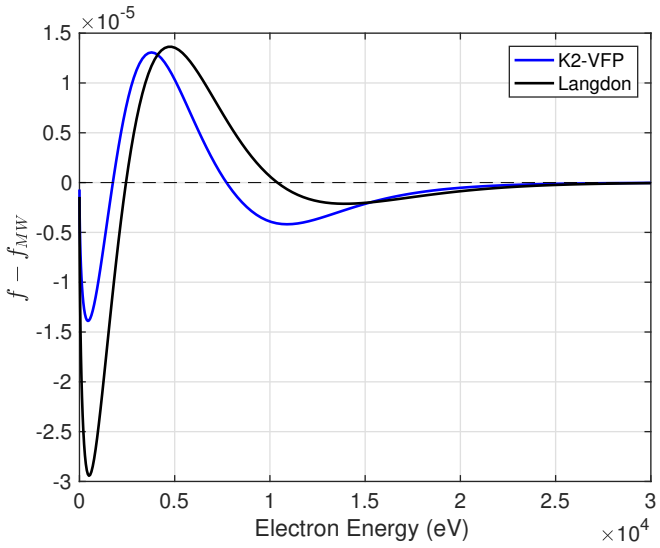

(b)

Figure 3.5: Electron energy distributions from Vlasov-Fokker-Planck calculations with the K2 code (blue) and from a Maxwell-Boltzmann distribution for electron temperature $T_e = 3013$ eV, using HYDRA plasma conditions from position $r = 465\mu$m in Figure 3.1a.

Spitzer-Harm thermal transport are assumed to have Maxwellian electron distributions, while simulations initiated with HYDRA-SNB plasma conditions also include alternate non-Maxwellian descriptions for the electron distributions either due to collisional laser absorption, or due to kinetic effects as calculated from Vlasov-Fokker-

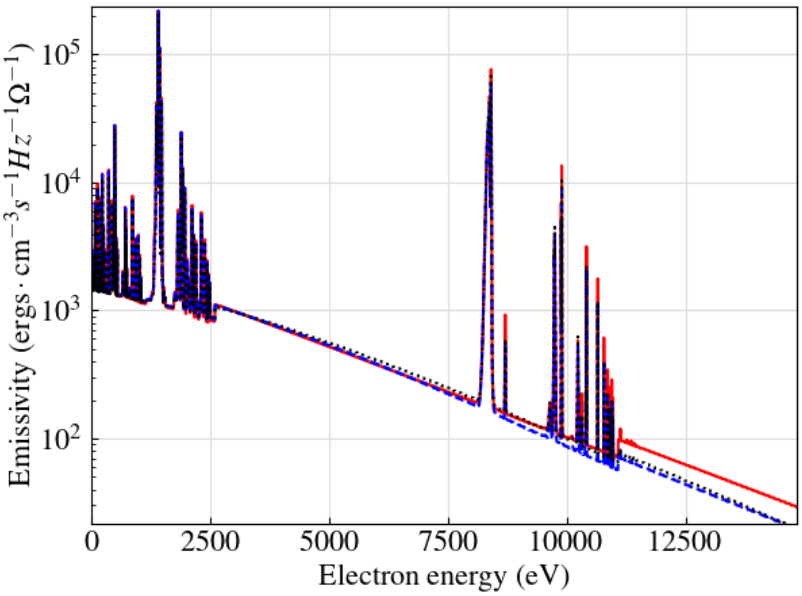

Figure 3.6: Emissivity spectra from a Maxwellian (red), K2-VFP (blue), and Langdon (black) electron distributions for a coronal copper plasma, with electron temperature $T_e = 3013$ eV, ion density 1.67×10^{20} cm^{-3}, $T_i = 1281$ eV and $T_R = 198$ eV.

Planck simulations. For plasma profiles described by Maxwellian or Langdon super-Gaussian electron distributions, Cretin simulations are initiated with plasma conditions (T_e, T_i, T_R, n_i) taken directly from the HYDRA Lagrangian mesh, which here consists of approximately 900-1200 zones to ensure $< 2.5\%$ variation in the coronal T_e and n_e plasma conditions due to resolution effects (for information on zonal resolution see Appendix A). Cretin calculations with K2-VFP electron distributions utilize plasma conditions from an 1000 cell uniform mesh (in radial distance r), which are interpolated from HYDRA simulation outputs. This resolution is necessary to use the K2 code to calculate the non-Maxwellian electron energy distribution functions generated from non-classical electron thermal transport. In Cretin simulations, the electron energy distribution function is discretized into 360 electron energy groups, distributed uniformly in electron velocity v up to maximum electron energy of 30-40 keV (where $\epsilon = k_B T_e/2$ and $v = \sqrt{k_B T_e/m_e}$), which ensures $< 1\%$ variation in total radiative flux from resolution effects (see Appendix B).

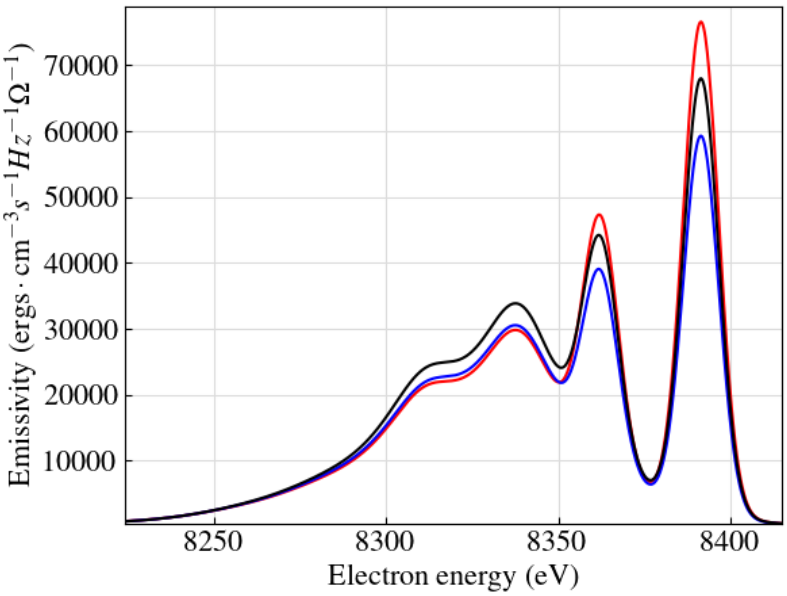

Figure 3.7: Copper K-shell line spectra from a Maxwellian (red), K2-VFP (blue), and Langdon (black) electron distributions for a coronal copper plasma, with electron temperature $T_e = 3013$ eV, ion density 1.67×10^{20} cm^{-3}, $T_i = 1281$ eV and $T_R = 198$ eV, from photon energies between 8200-8500 eV where the largest differences in emission due to non-Maxwellian electron energy distributions are observed.

3.5.2.1 Calculations of Radiation Spectra from Copper Spheres Irradiated by $I_L = 10^{15}$ W/cm^2

First, radiation spectra are calculated from plasma conditions generated from HYDRA-SNB and HYDRA Spitzer-Harm (classical) radiation-hydrodynamics simulations of a 430 μm radius copper-coated carbon sphere irradiated by square pulse laser of 2 nanosecond duration and 200 picosecond rise time and irradiance $I_L = 10^{15}$ W/cm^2, or equivalently peak laser power of 23 terawatts. Electron temperature profiles are shown in Figure 3.8 from both HYDRA-SNB and Spitzer-Harm simulations at $t = 200, 500,$ and 2000 picoseconds. Over the duration of the laser pulse, the plasma is heated and expands outwards, forming a laser-ablation front. At 200 picoseconds when the laser pulse first reaches peak power, the temperature gradients very steep (compared to later in time), thus generating the most non-Maxwellian elec-

tron energy distributions, with $\delta = 1.9\%$ in the electron-ablation dominated region, and $\delta = 6.4\%$ in the near coronal plasma. As the coronal plasma does not expand much at early time, the incident and reflecting laser is not as strongly attenuated by collisional absorption and thus the laser field remains intense. These higher intensities in the coronal plasma support steeper Langdon distributions, with a maximum of $m = 3$ and $\delta = 8\%$ at electron densities near n_c. Later in time at $t = 500$ picoseconds, after approximately one characteristic crossing time for the ablating plasma to flow from the critical surface into the coronal region, i.e., at the onset of the steady-state ablation front, both temperature and density gradient scale-lengths are longer in the plasma with $\delta \sim 1.7\%$ and 4.5% in the electron-ablation and sub-critical coronal regions of the plasma, respectively, from kinetic electron distributions. The laser energy is more readily absorbed in the longer scale-length plasma with maximum of $m = 2.7, \delta = 6.3\%$ in the coronal plasma. Finally at the end of the pulse duration at time $t = 2000$ picoseconds, the non-Maxwellian deviations are the smallest, with $\delta \sim 2\%$ from K2-VFP modeling, and $m = 2.5, \delta = 4.7\%$ from collisional absorption.

Figure 3.9 displays the calculated radiant intensity emergent from the outer boundary of the sphere, for the plasma conditions corresponding to the temperature profiles shown in Figure 3.8, specifically at three times (200, 500, 2000 ps) during the laser pulse duration, for classical and nonlocal electron transport, and with Maxwellian, nonlocal-transport-driven non-Maxwellian, and collisional-absorption-driven non-Maxwellian electron energy distributions. The inset shows the $2-1$ transition $K-$shell feature. The radiant intensity of 1D Cretin calculations from HYDRA-interpolated K2-VFP plasma conditions is shown in the inset, but not in the panel showcasing the full radiation spectra (for clarity see Appendix B). With respect to the radiant intensity, emission spectra from all conditions are similar with little discrepancies between them; the largest differences in are observed between the HYDRA-SH and HYDRA-SNB temperature profiles. At $t = 200$ picoseconds, the integrated radia-

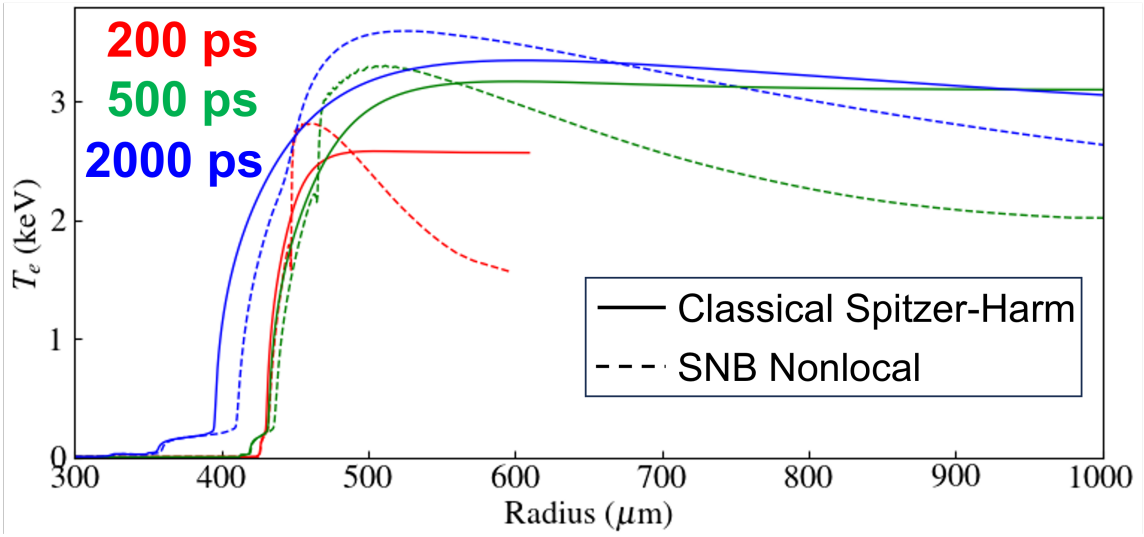

Figure 3.8: Temperature profiles from HYDRA radiation-hydrodynamics simulations of a copper sphere heated by a 3ω laser with irradiance of $\times 10^{15}$ W/cm^2 at 200 picoseconds (red), 500 picoseconds (green) and 2 nanoseconds (blue) and evolved with either classic Spitzer-Harm (solid) or SNB nonlocal (dashed) electron thermal heat transport models.

tive flux from HYDRA-SNB simulations is 5.09 terawatts (TW), compared with 5.79 TW from the HYDRA-SH simulation. At this point early in the duration of the laser pulse, the temperature gradients are very steep and thus nonlocal electron transport reduces the heat flux. Classical heat transfer overpredicts the electron heat transport, thereby facilitating the earlier development of a radiation-dominated low-temperature high-density region on the surface of the sphere. This leads to higher emissions from the Spitzer-Harm simulation. Later in time at $t = 500$ picoseconds, the growth of the radiation-dominated front becomes less pronounced, but more importantly the local electron heat flux facilitated by the electron temperature gradients saturates, hereby limiting the injection of energy into the self-emitting region of the sphere. In contrast, preheating due to nonlocal electron transport further enhances the growth of the radiation-dominated front beyond the classical limit, leading to higher radiative emissions (7.56 TW versus 6.98 TW) in the HYDRA-SNB simulation. This behavior persists over the duration of the laser pulse, and at $t = 2000$ picoseconds the HYDRA-

SNB simulation emits 8.10 TW compared to 6.62 TW from the classical simulation. In contrast to Maxwellian electron distributions, the emitted radiative power from Cretin simulations, which include descriptions of Langdon electron energy distributions is 5.10, 7.59, and 8.12 TW respectively for $t = 200, 500$, and 2000 picoseconds, for a mere increase of $0.2 - 0.4\%$. Results from Cretin simulations with K2-VFP distributions are similar, such that the change in the emissions falls below even the $< 1\%$ threshold dictated by the electron energy group discretization. Overall, we find that while the entire radiative spectra and subsequently the integrated radiative flux is affected by the changes in energy transport due to the electron heat flux model, it is not sensitive to non-Maxwellian departures in $f(\epsilon)$, neither from non-classical electron transport nor from inverse-bremsstrahlung laser absorption.

Instead, the impact of non-Maxwellian electron distributions is observed in the $K-$shell line emissions, specifically in the feature composed of lines due to $2-1$ transitions from various charge-states. Here, the effect of the electron transport model is also evident, with consistently more intense $K-$shell emissions from the HYDRA Spitzer-Harm simulations, including at later time in Figs. 3.9b and 3.9c, despite lower total radiative emissions from classical electron transport radiation-hydrodynamic simulations. These $K-$shell features have less intense He-like lines than those from the 0D emissivities because they are self-opaque. Instead, lines from the Li-like charge state are most intense in this feature. For the kinetic electron distributions from K2-VFP calculations, the largest changes in the radiation intensity are seen at early time in Figure 3.9a, with increased intensities from lines produced by lower charge (Li-like, Be-like, B-like, etc) states. This mirrors the observed changes in line intensities in emissivities from 0D calculations. With respect to the strongest emission at ~ 8340 eV associated with the Li-like complex, the K2-VFP electron distributions lead to an increased in the intensity of 6%. Later in time, this difference becomes much smaller, reducing to less than one percent due to smoother temperature gradients.

Alternatively, the consideration of Langdon super-Gaussian distributions produces a greater effect. For example, the intensity of the Li-like complex is enhanced by 10%. In contrast to K2-VFP distributions, this effect is persistent over the duration of the laser pulse.

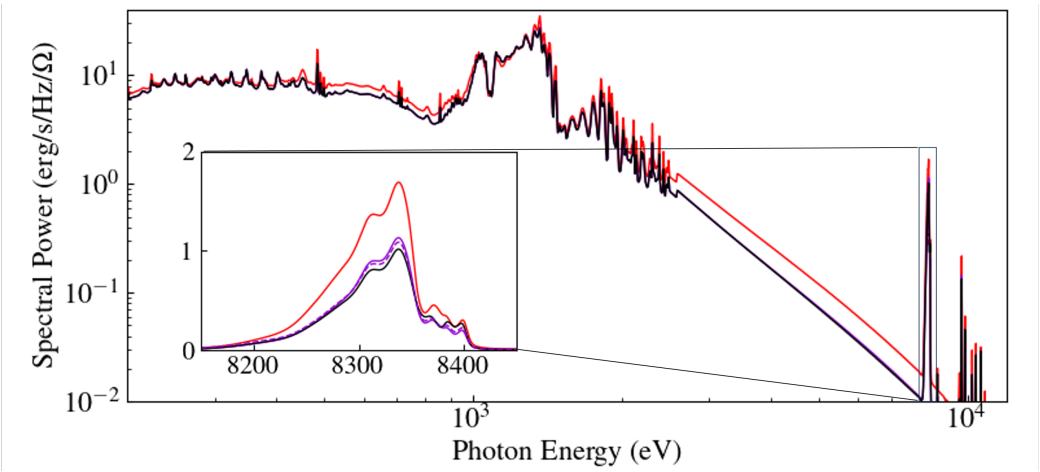

(a) $t = 200$ picoseconds

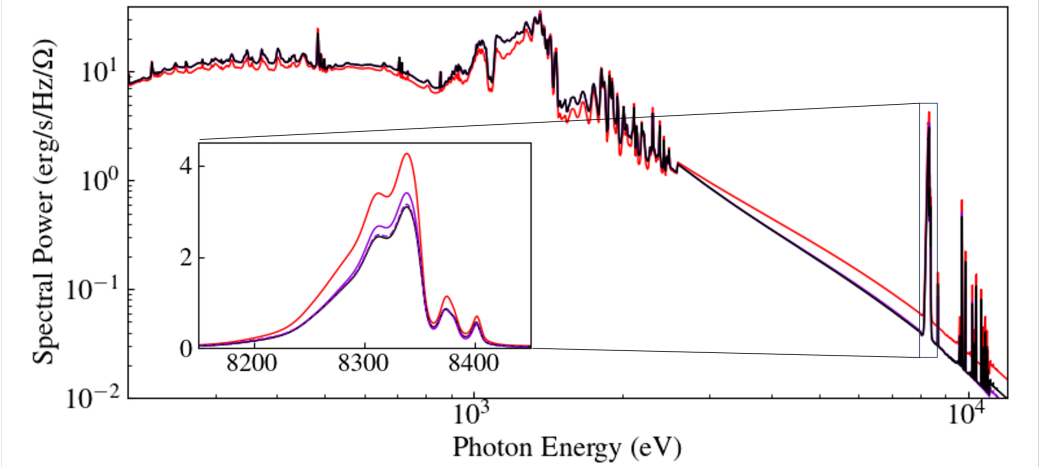

(b) $t = 500$ picoseconds

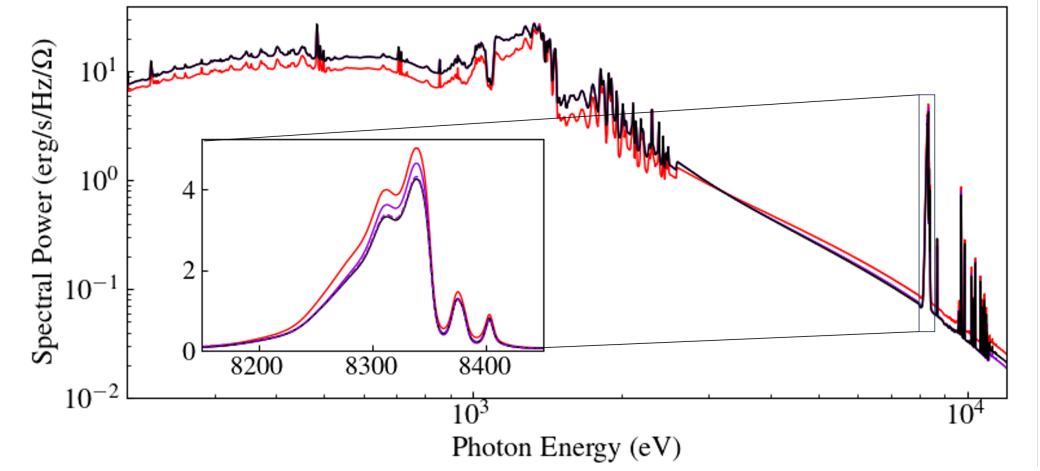

(c) $t = 2$ nanoseconds

Figure 3.9: Emitted spectral power emitted from Cu-spheres irradiated at 10^{15} W/cm^2 at three times, $t = 200, 500, 2000$ picoseconds from Spitzer-Harm Cu-sphere simulations (red lines) and SNB Cu-sphere simulations with maxwellian (black lines), Langdon super-Gaussian (violet lines), and K2-VFP kinetic (violet dashed lines) electron energy distributions. The inset shows a magnified of the largest $K-$shell features composed of $2-1$ transitions from various charge-states.

3.5.2.2 Dependence of the Emission Spectra on the Material

In addition to copper, we consider other materials for the coated-spheres irradiated at 10^{15} W/cm^2 laser intensity. Specifically, titanium ($Z = 22$), iron ($Z = 26$), and germanium ($Z = 32$) at nominal solid densities (4.51, 7.86, 10.5 g/cm^3) are studied. The motivation for studying these other materials is two-fold: Firstly, the variation in material element and atomic structure changes the energy of the characteristic X-ray emission lines Kα_1 and Kα_2 (which buttresses the lower bound of the range photonic energies from $K-$shell line emissions). Specifically, for titanium, iron, and germanium we have energies of $[4,510.75|4,504.86]$ eV, $[6,403.84|6,390.75]$ eV, and $[9,886.42|9,855.32]$ eV respectively for the K$\alpha_1|K\alpha_2$ lines from each material. Secondly, the deviation of coronal electron distributions from Maxwellian towards super-Gaussian due to collisional laser absorption is dictated by α which is proportional to the the ionization of the coronal plasma. So changing materials varies the mean ionization Z in the plasma corona, which varies the strength of the Langdon effect.

Again, from HYDRA radiation-hydrodynamic simulations of each respective material, plasma conditions are considered from $t = 200, 500$ and 2000 picoseconds in 1D Cretin simulations. In regards to the total radiation emission spectra, the behavior is similar to that of the copper sphere, namely we find non-Maxwellian electron distribution functions exhibit little influence–a few tenths of a percent–on the emitted radiative power, while radiation-hydrodynamic simulations with nonlocal electron transport radiate more energy, with the exception of very early in time ($t = 200$ ps), when radiation-hydrodynamic simulations employing classical electron thermal transport feature faster developing and–subsequently–hotter radiation-dominated temperature fronts. The influence of the macroscopic and microscopic changes in plasma conditions on the emissions from the $2-1$ transition $K-$shell feature for the different materials and different times is shown in Figure 3.10. Generally, plasma conditions

from HYDRA-SH simulations produce higher $K-$shell emissions with the exception of very late time in the titanium sphere shown in Fig. 3.10a. In regards to the non-Maxwellian energy distributions, Langdon distributions produce the largest impact on the radiative emissions, consistently increasing the strength of the highest emission within the Li-like complex. This intensity is enhanced by 8-10% for copper, iron, and germanium. Finally, the smallest changes in both the total emission and specific line features with respect to the Maxwellian 1D plasma are observed from Cretin calculations with K2-VFP distributions.

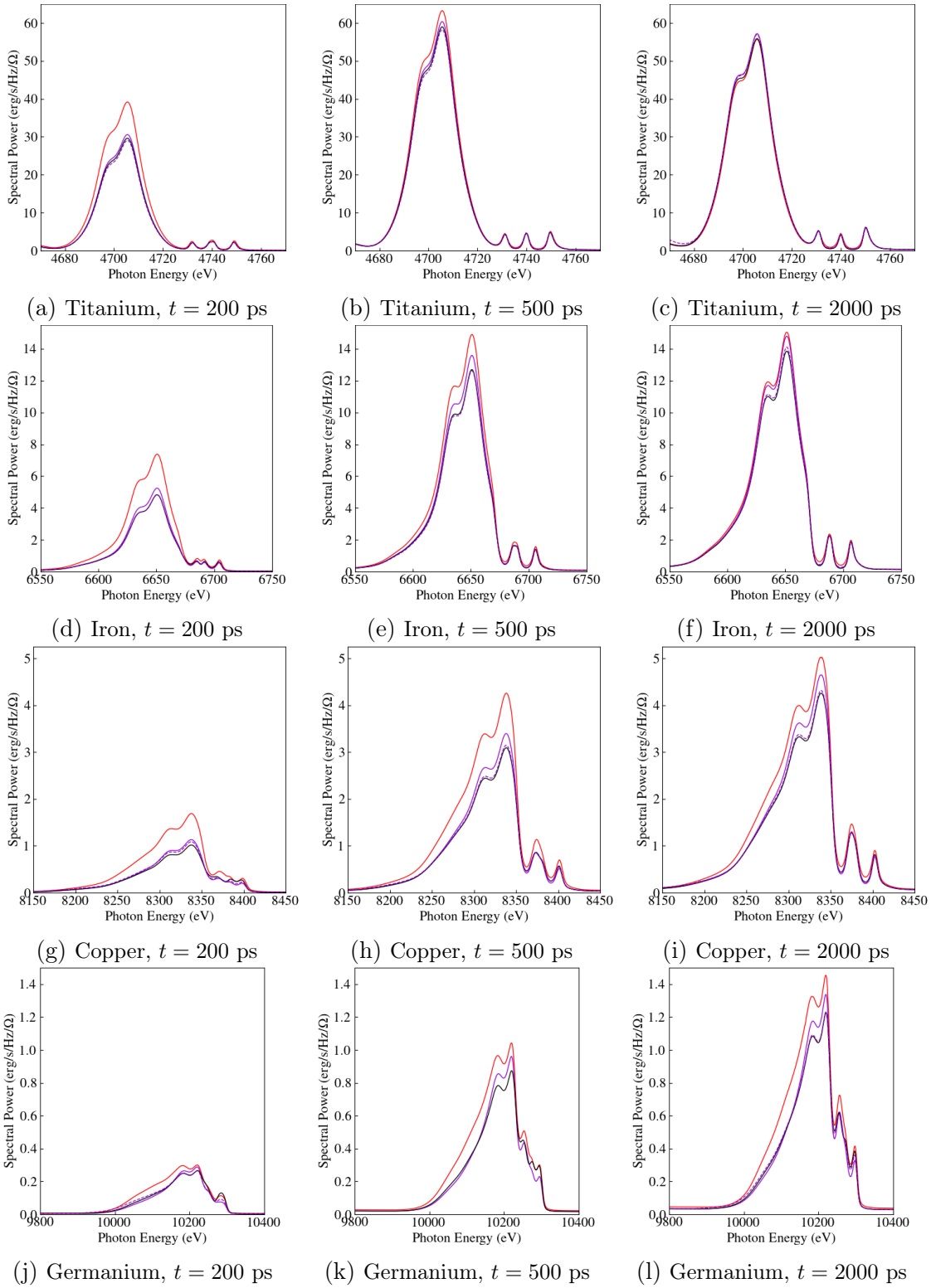

(a) Titanium, $t = 200$ ps (b) Titanium, $t = 500$ ps (c) Titanium, $t = 2000$ ps

(d) Iron, $t = 200$ ps (e) Iron, $t = 500$ ps (f) Iron, $t = 2000$ ps

(g) Copper, $t = 200$ ps (h) Copper, $t = 500$ ps (i) Copper, $t = 2000$ ps

(j) Germanium, $t = 200$ ps (k) Germanium, $t = 500$ ps (l) Germanium, $t = 2000$ ps

Figure 3.10: Integrated spectral power of the $2-1$ transition K-shell feature for (a-c) titanium, (d-f) iron, (g-i) copper, and (j-l) germanium at three times, $t = 200, 500, 2000$ picoseconds, from HYDRA-Spitzer-Harm plasma conditions (red lines), and HYDRA-SNB conditions with Maxwellian (black lines), K2-VFP kinetic (violet dashed lines) and Langdon super-Gaussian (violet solid lines) electron energy distribution functions.

3.6 Discussion

In 0D Cretin calculations with select plasma conditions from the copper sphere, it is observed that non-Maxwellian electron distributions modify the total emissivity by 3-4%, and consistently increase intensity of the largest non-Helium lines in the $2-1$ transition $K-$shell feature by 10-20%. When radiation transport is considered in 1D Cretin simulations, an approximately 10% increase in the intensities of the dominant $K-$shell feature is still observed, however the effect on the total radiative flux is greatly diminished so as to be negligible. This is due to the contribution to the radiation emissions from the low-foot radiation-dominated portion of the laser-ablation front. This region is much cooler than the corona with temperatures of hundreds of eV. However it is also denser with $n_e > 10 \times n_c$, so the intensities of the more strongest $L-$ and $M-$shell lines from photon energies up to 3 keV is $10\times$-$100\times$ greater than the intensities of those lines produced from the electron-dominated and coronal plasmas in the laser-ablation front. As a result, the radiative contribution from this region supersedes any variations in emissivity due to temperatures or electron distributions in plasma from the coronal and electron-dominated regions of the laser-plasma.

In contrast, the higher energy $K-$shell lines do not see significant contribution from the cooler plasma and is more reflective of conditions in the hotter and less dense plasma. For all plasma conditions, the classical HYDRA simulations produce the highest emissions in the $K-$shell. This implies that contributions to the $K-$shell emissions are predominantly from the electron heat flux dominated region of the ablation front, spanning electron densities of $(1-10) \times n_c$ and electron temperatures of a few hundred eV near the onset of the radiation-dominated front to 2-3 keV near the critical surface. The temperature of this region is dictated by the peak electron heat flux near n_c, which is smaller in the nonlocal simulation, thus leading to lower emissions. However it is also observed that the nonlocal plasma conditions with Langdon distributions have increased emissions in the $K-$shell. Because the

Langdon effect can only be stimulated by a persistent laser field, these effects are solely attributed to modifications in emissivities from plasma with densities $n_e < n_c$, indicating that the coronal plasma also contributes to this feature.

These multiple sensitivities of the $K-$shell features suggest that it is not a very promising portion of the spectra to analyze experiments of this system because changes in these features can originate from different regions of the laser-plasma, which makes the interpretation of any measurement challenging. And though non-Maxwellian electron distributions affect the line intensities, discrepancies relative to classical thermal transport are $\sim 10\%$ in these line features, which may not be differentiable in an experiment. Furthermore, a larger problem with considering this $K-$shell feature is highlighted by the qualitative similarity in the feature shapes from HYDRA simulations evolved with classical or nonlocal transport. Compared to the non-Maxwellian Cretin simulations, these similarities indicate that this feature exhibits low sensitivity to variations in electron temperatures in the electron-dominated and coronal plasma regions. The largest differences between local and nonlocal simulations is observed in the radiative spectra at early times ($t = 200$ ps), which is during a transitory phase in the evolution of the laser-plasma ablation front.

From radiation-hydrodynamics, Vlasov-Fokker-Planck, and atomic-kinetics simulations of plasma conditions generated from laser-heating with irradiance $I_L = 10^{15}$ W/cm^2, we see no reason to extend the study to consider a larger range of laser intensities. Firstly at lower laser intensities, non-Maxwellian effects become less significant. The laser-plasma is cooler and smoother so the thermal transport is more classical. And in the corona, reduced collisional-heating cannot sustain as steep electron energy distributions. Conversely, for higher laser intensities LPI effects become increasingly important to consider.

3.7 Conclusions

In summary, an investigation into the effect of non-Maxwellian electron energy distributions upon radiation emissions in the laser-irradiated sphere system is performed. The study employs an *a posteriori* hybrid approach that couples information from K2-VFP kinetic simulations and the atomic-kinetics code Cretin to calculate the radiation emissions from radiation-hydrodynamics simulations with HYDRA. This framework can be used to generally consider any non-Maxwellian electron distributions, specifically from other physics such as hot-electron generating laser-plasma interactions like the two-plasmon decay instability, the stimulated Raman scattering instability, or resonant absorption at the critical electron density. The present study considers the impact of non-Maxwellian electron distributions from either nonlocal electron transport or the Langdon effect, and finds that the effect upon the radiation emissions from these mid-Z materials irradiated by 3ω laser of irradiance $1\ \times 10^{15}$ W/cm^2 is a few tenths of a percent change to the total radiative flux, and up to 10% increase in intensity of certain line features from the $K-$shell. These differences may not be detectable in an experiment, and thus could (in the author's opinion) be considered negligible. This negative result does suggest that for electron heat transport modeling in laser-plasmas at these intensities for these materials, it is not necessary to precisely characterize the nonlocal deviation of the electron distribution function, provided that the nonlocal modification to the electron heat flux is accurately calculated. This approach can also be used to consider non-Maxwellian electron distributions from other physical phenomena such as hot-electron generating LPI like the Two-Plasmon-Decay instability or stimulated Raman scattering.

CHAPTER IV

Summary and Future Work

4.1 Summary

The broad goal of this dissertation is to study the role of electron heat transport modeling in laser-plasmas at intensities relevant to laser inertial confinement fusion designs and related experiments. Specifically, this problem is investigated in the laser-plasma that develops from a solid-sphere in direct-drive configuration, which mirrors tested experimental platforms relevant to ICF [76],[77],[78],[79]. This investigation of laser-irradiated spheres –split into two parts – composes the entirety of this dissertation.

In Chapter II, the effect of nonlocal electron heat transport in the sphere as modeled by the SNB reduced-nonlocal model first proposed by Schurtz, Nicolai, and Busquet [1] was investigated in a series of rigorous studies. First we evaluated the performance of the SNB model through comparisons with Vlasov-Fokker-Planck (VFP) kinetic calculations from the code K2. These comparisons indicated that the SNB model exhibits peak heat fluxes within 10% of the VFP prediction, which is a substantial improvement over the Spitzer-Harm heat flux. It bears reiterating here that this SNB model includes the improvements suggested by Brodrick [2]. Additionally, this study is notable in that it represents the first collection of integrated simulations considering the SNB model with Brodrick's corrections; previous work only considered

these effects in stationary, simplified plasma conditions pertinent to hohlraum modeling. In HYDRA radiation-hydrodynamics simulations, the SNB model was compared against flux-limited classical Spitzer-Harm electron heat transport to assess the effect of nonlocal transport on the laser-plasma ablation front. It was found that nonlocal heat transport produces cooler coronal plasma temperatures from the reduced, delocalized heat transport in this region, and higher (radiative) conversion efficiency from the laser-heated plasma due to enhanced energy transport from nonlocal electron preheat to the radiation-dominated front. This result falls beyond the parameter space of plasma conditions produced when employing classical electron heat transport. This result is significant because it both correlates directly to experimental measurables and is physically explained by different aspects of nonlocal deviations of the electron heat transport.

In Chapter III, the study of the laser-irradiated sphere is extended further towards modeling not only the nonlocal heat transport, but also the non-Maxwellian electron energy distributions, which we hypothesized could produce a noticeable impact to the radiative properties of the plasma. In addition, this work also studies the effect non-Maxwellian electron distributions from the inverse-bremsstrahlung laser heating. In order to consider non-Maxwellian electron distributions, collisional rates in the Cretin atomic-kinetics code were calculated using discrete electron energy distributions, with specific distribution information supplied either from the K2 code [62] or from analytic theory [68]. In order to computationally assess these non-Maxwellian effects, an *a posteriori* hybrid scheme was used, composed of radiation-hydrodynamic, Vlasov-Fokker-Planck, and collisional-radiative atomic-kinetics codes and approaches. This study found that non-Maxwellian electrons did not affect the total radiative flux from the laser-irradiated sphere, but did affect the intensity of the $K-$shell features. However, the changes in these features are small and are unlikely to be differentiable by experimental diagnostics. Collectively, these results suggest that non-Maxwellian

electron distributions have little influence in the laser-irradiated sphere, which counters our original hypothesis. This negative result also implies that the SNB model employed in the previous study is sufficient for modeling electron transport effects in the laser-irradiated sphere.

4.2 Future Work

This dissertation presents numerous opportunities to improve and extend the work. Here, we will discuss some limitations of the research, and specify potential avenues for further studies.

4.2.1 Improving Laser Modeling

As was described in Chapter I, the three dominant energy transport mechanisms in the laser-plasma ablation front are radiation transport, electron transport, and laser-plasma coupling. In this study, the radiation transport modeling can be enhanced with improved atomic-physics models, and of course the core operative of this work is to assess the impact of electron transport modeling. Presently, the laser absorption is assumed to be solely from inverse-bremsstrahlung absorption, and the exclusion of the effects of additional laser-plasma interactions (LPI) beyond collisional laser absorption is a clear deficiency in present modeling efforts. Including LPI effects is the logical next step for a more comprehensive model of the laser-irradiated sphere. In HYDRA, the inline LPI model could be leveraged to include the effect of cross-beam energy transfer (CBET) from stimulated Brillouin scattering, and stimulated Raman scattering (SRS) induced backscattering [113]. However, in these models there exist phenomenological multipliers like limits on ion acoustic wave amplitudes [114], and additionally the SRS backscattering model is *post hoc*. Alternatively, one could consider a more precise inline inverse ray-trace approach [115][98] that also accounts for beam polarization rotation.

These models account for the modification in laser energy deposition, but do not account for the effect of hot electrons produced by SRS, as well as by the two-plasmon decay instability and resonant laser absorption. For these various LPI, hot electron scalings relevant to laser-plasma conditions at these intensities are determined from experiments [17]. Unfortunately the SNB model does not consider the electron distribution function in its heat flux calculation and thus cannot consistently incorporate hot electron effects in a radiation-hydrodynamic model. However the transport of hot electrons generated by LPI can be consistently modeled in a kinetic code such as K2, which could – with no small effort – be coupled to a radiation-hydrodynamics code. Alternatively, the resulting electron distributions from K2 simulations could be readily supplied to the simulation-framework used in Chapter 3 to calculate the effect on the radiative properties of the laser-plasma front induced by these hot electrons.

Finally, while we considered the effect of the plasmas' non-Maxwellian electrons distributions upon radiation transport from collisional absorption, we did not consider the role of the Langdon effect on electron heat transport. The super-Gaussian electron distributions will change the electron heat transport directly by modifying f_1, and implicitly by changing the laser absorption from collisional heating [91]. These effects from super-Gaussian distributions can be accounted for with an inline inverse-bremsstrahlung modification on the laser absorption [68], coupled with a recently developed SNB model that can calculate the nonlocal transport deviation from super-Gaussian distributions (as opposed to Maxwellian) [116].

4.2.2 Laser-Heated Gas Jet

To improve models of the the laser-irradiated sphere, it is necessary to include and study the effects of additional laser physics. If instead one desires to further study nonlocal electron transport and/or non-Maxwellian distributions, it is worthwhile to consider a laser-heated gas jet [117] instead of the solid laser-irradiated sphere. In

this system, the laser propagates through the underdense gas, providing a consistent temperature source that sustains a radially propagating heat front into a relatively uniform density plasma. Here, the lower electron density ($n_e \sim 10^{19}$ cm^{-3}) reduces λ_{ei}, enabling nonlocal electron transport at lower electron temperatures and laser intensities. At lower laser intensities, the non-Maxwellian influence of both the Langdon effect and potential LPI could be reduced. And in the laser-irradiated sphere, though differences were observed in the radiative emission spectra in the coronal plasma, these effects were obfuscated in the emitted radiative spectra by the large radiative contribution from the dense, radiation-dominated front. In contrast, the entire laser-plasma in a gas jet is coronal plasma, so these emissivities are further isolated and the possibility of measuring differences in their emissivities is enhanced. In addition, non-Maxwellian electrons can be generated in the laser-heated gas jet from heating of gas clusters [118]. Like in chapter III, line emissions from $K-$shell transitions are sensitive to non-Maxwellian electrons, provided the differences in the electron distributions are at energies sufficient to stimulate these transitions. And the photon energies from the $K-$shell can be modulated by varying the gas composition. For example the noble gases neon, argon, and krypton have K-α energies of $\sim$ 850, 3000, and 12,600 eV respectively. Furthermore, $L-$shell emissions (L-$\alpha \sim$ 1600 eV) could also be considered for krypton gas.

APPENDICES

APPENDIX A

Numerical Convergence of the 1D Sphere Model in HYDRA

Here, details of a convergence study for the 1D Lagrangian laser-sphere model used in HYDRA radiation-hydrodynamics simulations is discussed. The work here informs the appropriate simulation resolutions for sphere studies in this dissertation.

A.1 Numerical Convergence of the 1D Sphere Model in HYDRA

In simulations of laser-irradiated plasmas, strong laser energy deposition occurs in the plasma at densities close to the critical density. If there are too few zones in this area of the plasma, the density profile is insufficiently resolved and the resulting ablation pressure P_A is inaccurately calculated [119]. As the ablation pressure affects the development of the strong T_e and n_e gradients in this region, we perform a convergence study to constrain our observations. In the laser-irradiated sphere model, the narrowest zone with width Δx is on the outer surface; subsequent zone widths are proportionally increased by a feathering ratio $R_f < 1$ such that the n^{th} zone thickness is $\Delta x_n = \Delta x / R_f^n$. For these simulations, a minimum zone width of 1.25 nm is used

and R_f is varied from 0.9900-0.9997, corresponding to Lagrangian simulations with ~ 600 to ~ 4800 zones for the coarsest and finest resolutions.

The prescribed Lagrangian zoning and resolution is not arbitrary, and can be physically justified. It is the opinion of the author of this dissertation that this point is worth emphasizing and discussing here. As mentioned by Scheiner et al. [119], insufficient numerical resolution affects the ablation pressure generated by laser energy deposition. The discrepancies in the predicted ablation pressure emerges because the density profile near n_c in a–laser-driven–free-expansion is exponential. In the case of an under-resolved density profile, a different mass of plasma at sub-critical densities is predicted from Lagrangian approaches, where specifically simulations with inadequate resolutions produce excessive inverse-bremsstrahlung absorption in the laser-plasma that subsequently drives higher ablation pressures. To ensure the laser deposition is accurately modeled the Lagrangian zones should resolve the minimum density-gradient scale-length L_{n_e} driven by the laser intensity near n_c. L_{n_e} was not determined for these studies, and instead we use $L_{n_e} = 0.33$ μm as reported by Scheiner et al [119], which was determined from studies of laser-plasmas in similar geometries (spherical) and subject to comparable laser irradiances ($I_L = 7.9 \times 10^{14}$ W/cm^2). The density at critical is $n_c \sim 9 \times 10^{21}$ cm^{-3}, whereas the initial Lagrangian zonal resolution is at solid density. Considering copper with density $\rho = 8.98$ g/cm^3, this suggests $\Delta x \sim 1.2$ nm expands to $\Delta x_{critical} = 0.33$ μm. As the laser(s) heats and ablates the plasma, L_{n_e} increases due to the bulk heating and expansion of the plasma, as well from the attenuation of ablation pressure necessary to sustain the strong density gradients. The ablation pressure attenuates because of the accumulation of ablating mass in the coronal plasma, which enhances the laser energy deposition and subsequently reduces the laser intensity near n_c. In practice, this relaxation of L_{n_e} enables zones to be relaxed with feathering ration R_f to reduce the computational cost. The specific limitations for this feathering ratio are assessed in this resolution study.

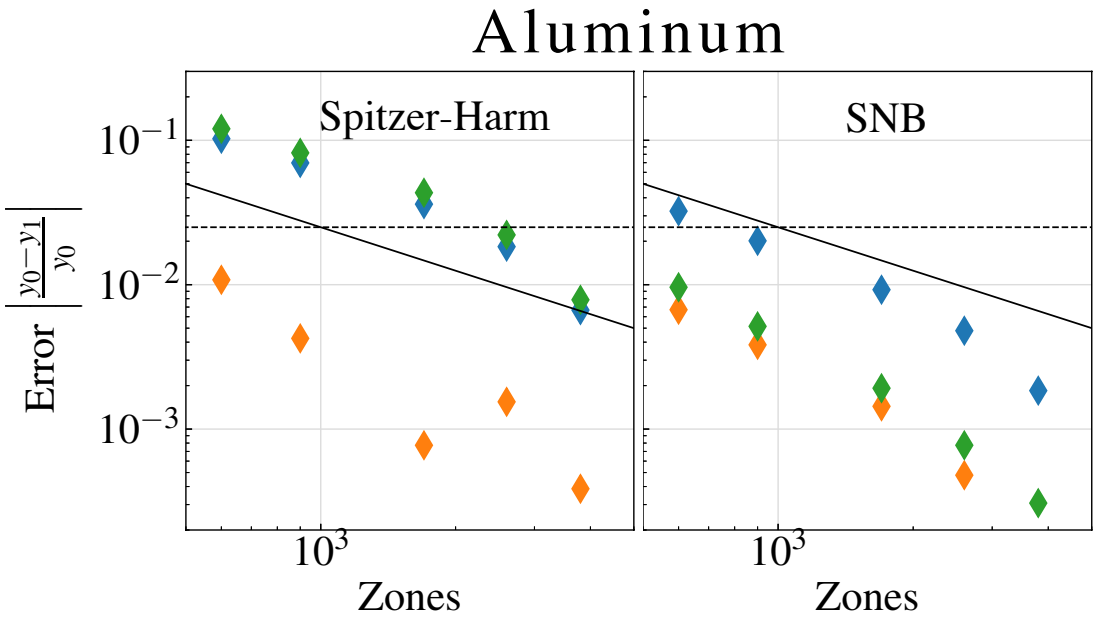

Figure A.1: Electron temperature (orange) and density (blue) convergence results at $r = 820$ μm at $t = 1$ ns as well as total energy coupling (green) for aluminum spheres simulations using the (left) Spitzer-Harm ($f = 0.05$) and (right) SNB electron thermal transport models. The error percentage is the normalized deviation from the highest resolution calculations. Solid black line: linear convergence rate; dashed black line: 2.5% error.

We quantify the convergence by the variation of the instantaneous coronal electron temperatures and densities at $t = 1$ ns, taken $r = 820$ μm or 390 μm from the initial sphere surface, as well as in the integrated quantity of total laser energy absorption during the simulation duration. The relative variation in T_e, n_e and laser absorption is calculated as $\epsilon = \left|\frac{y_1-y_0}{y_0}\right|$, where y_0 is from a maximum resolution 1D simulation using 4800 Lagrangian zones. Figure A.1 shows the convergence behavior in observables from aluminum spheres, which exhibits the largest error of the materials under consideration. The convergence behavior is close to first-order, i.e., $\epsilon \propto N^{-1}$ where N is the number of zones. HYDRA SNB simulations also exhibit first-order convergence, but with significantly smaller errors. For an error of $\epsilon < 0.025$ in T_e, n_e and laser absorption, $f = 0.05$ Spitzer-Harm HYDRA simulations require ~ 2600 Lagrangian zones, while SNB simulations require ~ 900 Lagrangian zones. Smaller

errors are observed in HYDRA-SNB simulations because the nonlocal transport incorporates information from the entire temperature profile, producing a more precise heat flux calculation with respect to numerical resolution. In addition, flux-limited ($f = 0.05$) Spitzer-Harm simulations introduce numerical discontinuities in the heat flux description, which necessitates more stringent resolution requirements. For the studies presented above, $\sim$2600 zones are used to ensure $< 2.5\%$ variation in laser absorption, coronal T_e and n_e due to resolution effects in Chapter (sphere chapter ref). In Chapter (non-Maxwell), HYDRA simulations are performed with either nonlocal electron heat transport or non-flux-limited Spitzer-Harm heat flux, so a less restrictive Lagrangian resolution equivalent to ~ 900 zones is used.

APPENDIX B

Cretin Simulation Details: Convergence and Spatial Resolution

In Chapter 2, Cretin simulations are used to calculate detailed radiation spectra from HYDRA plasma conditions and to consider the effect of non-Maxwellian electron energy distributions upon the laser-plasmas' radiative properties. The employment of a discrete description for these electron distributions naturally introduces additional numerical errors that are characterized here. In addition, the retrieval of K2-VFP kinetic information from HYDRA simulations necessitates the interpolation of plasma conditions from a Lagrangian description to a Eulerian description. This affects the radiation spectra predicted from 1D Cretin calculations, and is discussed here.

B.1 Numerical Convergence of Discrete Electron Energy Distributions in Cretin simulations

In Cretin, non-Maxwellian electron distributions are described by defining electron densities for N discrete electron energy groups, which can be arbitrarily spaced. Following the convention of the electron velocity distributions in the K2 Vlasov-Fokker-Planck kinetic code, the electron energy distributions in this study are uniformly dis-

cretized in velocity-space, or equivalently, quadratically discretized in energy space since the electron energy $E = \frac{1}{2} m_e v^2$. We assess the effect of varying both the number of electron energy groups N, and of varying the maximum upper bound E_{max} in electron energy on Cretin predictions with discrete electron energy distributions.

Convergence studies are considered for two 0D copper plasma conditions which correspond to plasma conditions in the electron-heat-dominated ablation front, and in the sub-critical coronal plasma from a HYDRA simulation of a copper-sphere irradiated by a laser of intensity 10^{15} W/cm^2 at $t = 500$ ps. At the first position, the electron density is $\sim 2 \times n_c$, and the temperatures are $T_e = 1235$ eV, $T_i = 1098$ eV, and $T_R = 217$ eV respectively for the electrons and ions, and for the radiation field. The ionization is $Z = 26.53$. At the second position, the electron density is $\sim 0.5 \times n_c$, and the temperatures are $T_e = 3012$ eV, $T_i = 1281$ eV, and $T_R = 198$ eV respectively for the electrons and ions, and for the radiation field. The ionization is a little higher here with $Z = 26.82$. For these two conditions, convergence behavior is characterized by a difference in flux from the integrated emissivity of the 0D plasma. This is considered with respect to the total emissivity integrated over the entire photon energy range, and with respect to the integrated emissivity emergent from the $2-1$ transition $K-$shell feature, which is integrated between photon energies of 8000-8500 eV.

B.1.1 Maximum Electron Energy

In this study, the maximum electron energy E_{max} is varied from 10-60 keV. The simulations are discretized uniformly in velocity-space with the same spacing for each simulation, such that the number of electron energy groups N varies with E_{max}, with 1000 discrete electron groups for the highest energy simulation where $E_{max} = 60$ keV. This simulation is used as the control case for calculating errors.

The corresponding errors for the total emissivity and the emissivity from the

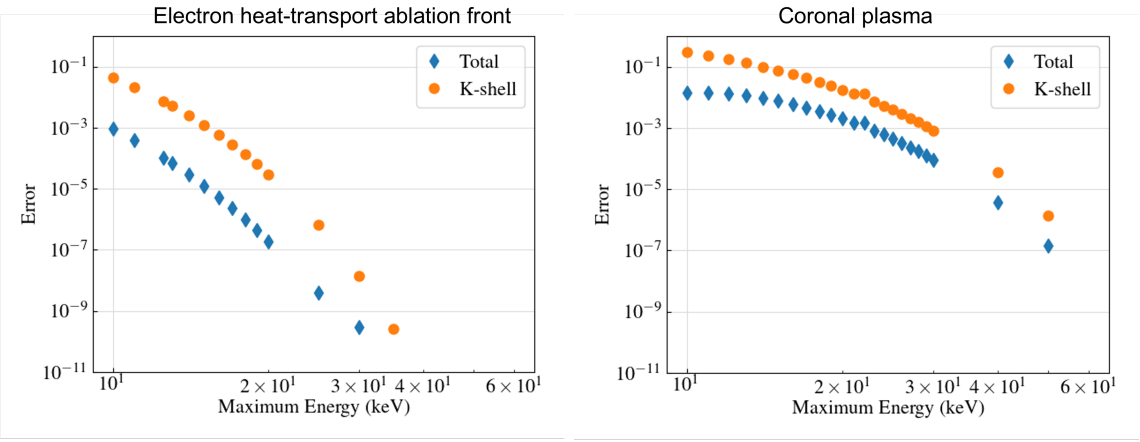

(a) (b)

Figure B.1: Error in the total (blue) integrated and 2-1 transition K-shell feature integrated emissivities for (a) plasma conditions corresponding to the electron heat transport dominated ablation front with $n_e \sim 2 \times n_c$ and (b) the coronal plasma with $n_c \sim 0.5 \times n_c$ with respect to varying the maximum electron energy E_{max} of the energy distribution discretization.

$K-$shell feature are shown in Figure B.1 for both plasma conditions. Errors are higher for the $K-$shell feature because these are amongst the highest energy transitions ($\sim$ 8 keV) present in the copper emissivity spectra, and thus are the most sensitive to electrons in the high-energy tail. The convergence behavior is similar, but errors are larger in the half-critical density plasma condition because it is hotter (3 keV vs $\sim$ 1.2 keV) and has more electrons at hotter energies.

B.1.2 Number of Electron Groups

In this study, the number of electron energy groups is varied, with fixed upper bound in electron energy E_max = 30 keV. Again the simulations are discretized uniformly in velocity-space or quadratically in energy space, with a control simulation consisting of maximum $N = 1000$ electron groups. The subsequent errors in the total and $K-$shell emissions is shown in Figure B.2 for both plasma conditions. The convergence behavior with respect to number of electron groups is less obvious than with respect to E_{max}, especially when considering the integrated emissivity from the

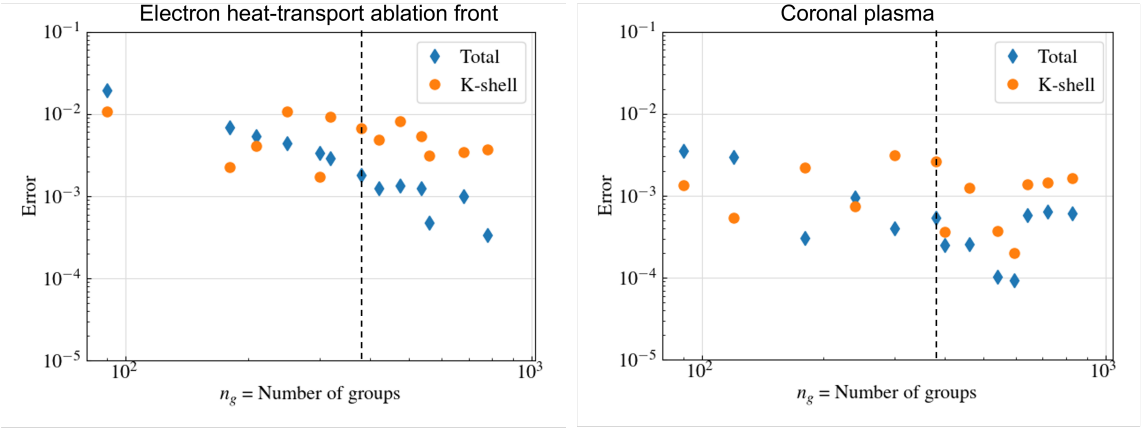

(a) (b)

Figure B.2: Error in the total (blue) integrated and $2-1$ transition $K-$shell feature integrated emissivities for (a) plasma conditions corresponding to the electron heat transport dominated ablation front with $n_e \sim 2 \times n_c$ and (b) the coronal plasma with $n_c \sim 0.5 \times n_c$ with respect number of electron energy groups.

$K-$shell feature. Instead of producing a convergence behavior, the K-shell error instead appears to be bounded, with 1% error from the denser plasma condition, and a few-tenths of a percent from the coronal plasma. Considering these results in assessing E_{max} and the electron groups, copper simulations are initialized with $N = 360$ electron energy groups up to $E_{max} = 30$ keV. The maximum error is gated by the electron group discretization, which ensures $< 0.2\%$ error in the total emissions, and 1% error in $K-$shell emissivities. Titanium and iron simulations are performed with an identical electron group discretization, however for germanium $E_{max} = 40$ keV is used due to the higher energies in the $K-$shell transitions.

B.2 Differences in Cretin Simulations with HYDRA and K2-VFP Plasma Conditions

To calculate K2-VFP kinetic electron energy distributions, HYDRA plasma conditions must be interpolated from the Lagrangian description to the Eulerian description uniformly discretized in space. The Cretin calculation, which considers the plasma

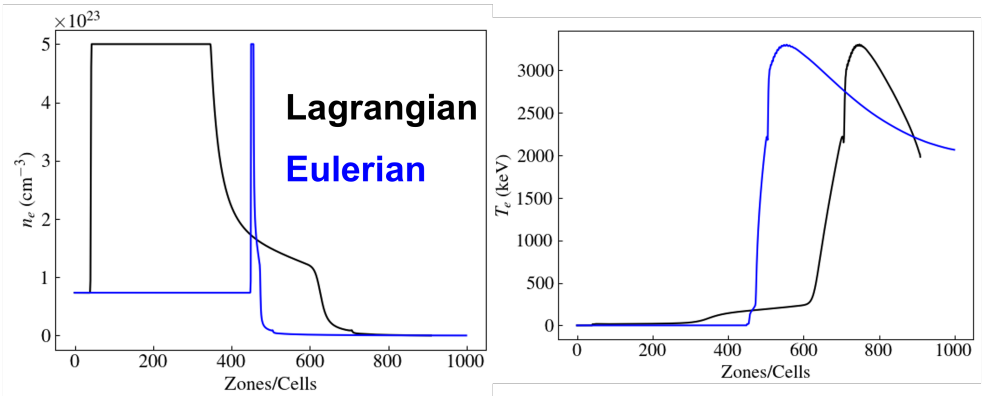

Figure B.3: Electron density n_e (left) and temperature T_e (right) profiles for Lagrangian (black) and Eulerian (blue) descriptions of the laser-plasma ablation front from copper sphere HYDRA simulations with irradiance $I_L = 10^{15}$ W/cm^2 at $t = 500$ picoseconds. The electron density is limited to 5×10^{23} cm^{-3} to avoid instability in the K2-VFP kinetic calculation.

conditions from either description, then exhibits underlying variations in the calculated radiation spectra reflective of each respective fluid description. Figure **??** shows the electron temperature and densities for the Lagrangian and Eulerian descriptions. As the Eulerian mesh is uniform, those profiles are analogous to the spatial representation of the temperature and density profiles. Here, it can be observed that the radiation-dominated ablation front and electron-heat-transport dominated ablation fronts have very different numerical resolutions in each description. This is because numerical zones in the Lagrangian description are (nearly) uniformly distributed in mass as opposed to space. The radiation-dominated ablation front is $\approx 15\mu$m in thickness, and is considerably denser than the electron-ablation front and plasma corona, with ~ 250 Lagrangian zones encompassing this region. In contrast, for the Eulerian description with $\Delta r \approx 0.92$ μm, only 16 numerical cells describes this region. Similarly, the $\sim 30\mu$m thick electron-thermal-transport dominated ablation region is represented with approximately 32 Eulerian cells compared to about 85 Lagrangian zones.

The subsequent radiative emission spectra calculated at the outer radius from Cretin is shown in Figure B.4, with focus on the spectral energy ranges that contain

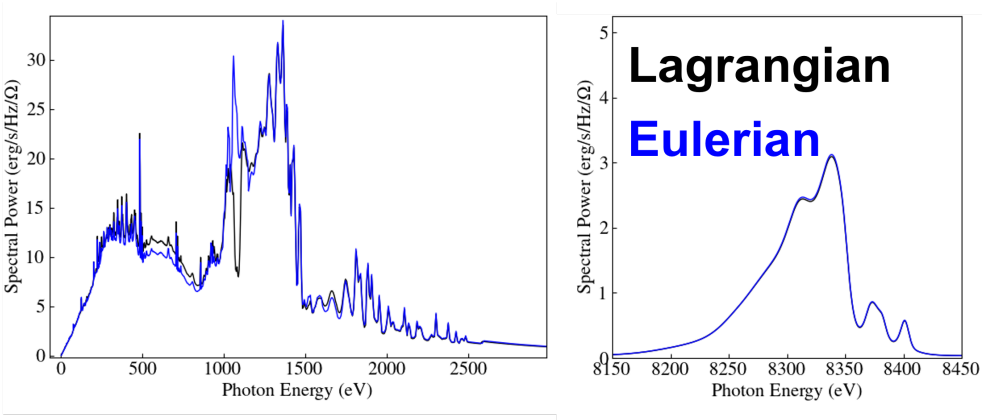

Figure B.4: Generated emitted radiative spectra at the outer boundary of the sphere system from Lagrangian (black) and Eulerian (blue) descriptions of the laser-plasma ablation front from copper sphere HYDRA simulations with irradiance $I_L = 10^{15}$ W/cm^2 at $t = 500$ picoseconds. The left panel shows spectra details from lower energy (< 2.5 keV) thermal radiation composed of continuum radiation as well as line emissions from $L-$ and $M-$shell transitions, while the right panel shows the spectra for the 2-1 transition $K-$shell feature.

background continuum radiation as well as line emissions from the $K-$, $L-$, and $M-$shell transitions. It is evident that Lagrangian and Eulerian descriptions predict different intensities from the lower energy $L-$ and $M-$ shell transitions, with the Lagrangian description predicting higher radiative fluxes from the $M-$shell, while the Eulerian simulation predicts a substantially higher intensity from the $L-$shell line at ~ 1100 eV. The total radiative flux also differs, with the Eulerian case emitting 7.657 TW of power compared to 7.564 TW from the Lagrangian simulation.

To interpret differences from each simulation it is first necessary to evaluate where regions of the plasma profiles from each description may be under-resolved. As a cursory approach, the system is evaluated based upon the density gradient scale length $L_{n_e} = |n_e/(\partial n_e/\partial r)|$. Ostensibly, one desires the zone/cell width Δr to be comparable or smaller to L_{n_e} in order to sufficiently resolve the density profile.

In the radiation-dominated thermal front L_{n_e} ranges from 1-27 μm (microns). The minimum value for L_{n_e} here is about micron, located at the lowest temperature foot of the radiation front where the electron density approaches the artificial limit

of 5×10^{23} cm^{-3} – necessary for stability of K2-VFP simulations – and the electron temperature ranges from $10 - 100$ eV. L_{n_e} is maximum in the flat-top region where $T_e = 150 - 250$ eV, hovering at ~ 30 μm here. For the Lagrangian simulation, $\Delta r \sim 0.06\mu$m (15μm/250 zones). In the electron-thermal-transport dominated ablation front, the density gradient scale length is smallest ($\approx 2\mu$m) at the foot of this temperature front, where electron temperatures range from 200-500 eV. For the Lagrangian description, $\Delta r \sim 0.06$ still at the interface of the two heat fronts because the Lagrangian spacing is inversely proportionate to ρ. Finally, in the coronal plasma the density profiles are much smoother with $L_{n_e} = 50 - 100$ μm, and the Lagrangian resolution is approximately 2 microns here.

For the Eulerian description, it is evident that the cell resolution ($\Delta r \approx 0.92$ μm) is comparable to the density gradient scale length at the lower temperature portion of the radiation foot where electron temperatures range from tens up to a hundred eV, and in the low foot of the electron ablation front with temperatures of a few hundred eV. In contrast, the Lagrangian description is more resolved in these two regions of the laser-plasma. In the coronal region, both descriptions give comparable numerical resolution. The differences in numerical resolution in the plasma profile mirrors the observed discrepancies, in the Cretin spectra, which manifests in the $L-$ and $M-$shell lines that emerge primarily from denser, inner radiation dominated and electron dominated ablation regions. In contrast, because the $K-$shell lines largely originate from the hotter, less dense outer coronal plasma, we find these features are insensitive to the Lagrangian or Eulerian descriptions.

BIBLIOGRAPHY

BIBLIOGRAPHY

[1] G. P. Schurtz, P. D. Nicolaï, and M. Busquet, "A nonlocal electron conduction model for multidimensional radiation hydrodynamics codes," *Phys. Plasmas*, vol. 7, no. 10, pp. 4238–4249, 2000.

[2] J. Brodrick, R. Kingham, M. Marinak, M. Patel, A. Chankin, J. T. Omotani, *et al.*, "Testing nonlocal models of electron thermal conduction for magnetic and inertial confinement fusion applications," *Phys. Plasmas*, vol. 24, p. 092309, Sep 2017.

[3] R. P. Drake, *High-Energy-Density Physics*. Graduate Texts in Physics, Springer International Publishing, 2018.

[4] I. Shkarofsky, T. Johnston, and M. Bachynski, *The Particle Kinetics of the Plasmas*. Addison-Wesley Publishing Company, 1966.

[5] L. Spitzer and R. Härm, "Transport Phenomena in a Completely Ionized Gas," *Phys. Rev.*, vol. 89, pp. 977–981, Mar 1953.

[6] D. Mihalas and B. Weibel-Mihalas, *Foundations of Radiation Hydrodynamics*. Courier Corporation, 1999.

[7] F. Hoyle and W. A. Fowler, "Nucleosynthesis in supernovae.," *The Astrophysical Journal*, vol. 132, p. 565, 1960.

[8] E. Pian, P. D?Avanzo, S. Benetti, M. Branchesi, E. Brocato, S. Campana, E. Cappellaro, S. Covino, V. d?Elia, J. Fynbo, *et al.*, "Spectroscopic identification of r-process nucleosynthesis in a double neutron-star merger," *Nature*, vol. 551, no. 7678, pp. 67–70, 2017.

[9] S. Atzeni and J. Meyer-ter Vehn, *The Physics of Inertial Fusion: Beam Plasma Interaction, Hydrodynamics, Hot Dense Matter*, vol. 125. Oxford University Press, 06 2004.

[10] J. H. Nuckolls, "The feasibility of inertial-confinement fusion," *Physics Today*, vol. 35, no. 9, pp. 24–31, 1982.

[11] M. Haines, "A review of the dense z-pinch," *Plasma Physics and Controlled Fusion*, vol. 53, no. 9, p. 093001, 2011.

[12] M. R. Gomez, M. A. Sweeney, D. Ampleford, S. A. Slutz, G. A. Rochau, and D. Sinars, "Inertial confinement fusion-experimental physics: Z-pinch and magnetized liner inertial fusion.," tech. rep., Sandia National Lab.(SNL-NM), Albuquerque, NM (United States), 2021.

[13] J. Ongena, R. Koch, R. Wolf, and H. Zohm, "Magnetic-confinement fusion," *Nature Physics*, vol. 12, no. 5, pp. 398–410, 2016.

[14] G. A. Wurden, S. C. Hsu, T. P. Intrator, T. Grabowski, J. Degnan, M. Domonkos, P. Turchi, E. Campbell, D. Sinars, M. Herrmann, *et al.*, "Magneto-inertial fusion," *Journal of Fusion Energy*, vol. 35, pp. 69–77, 2016.

[15] S. A. Slutz and R. A. Vesey, "High-gain magnetized inertial fusion," *Phys. Rev. Lett.*, vol. 108, p. 025003, Jan 2012.

[16] E. National Academies of Sciences and Medicine, *Plasma Science: Enabling Technology, Sustainability, Security, and Exploration*. The National Academies Press.

[17] R. S. Craxton, K. S. Anderson, T. R. Boehly, V. N. Goncharov, D. R. Harding, J. P. Knauer, *et al.*, "Direct-drive inertial confinement fusion: A review," *Phys. Plasmas*, vol. 22, p. 110501, Nov 2015.

[18] J. Lindl, "Development of the indirect-drive approach to inertial confinement fusion and the target physics basis for ignition and gain," *Physics of Plasmas*, vol. 2, pp. 3933–4024, 11 1995.

[19] R. Betti and O. Hurricane, "Inertial-confinement fusion with lasers," *Nature Physics*, vol. 12, no. 5, pp. 435–448, 2016.

[20] N. Fleurot, C. Cavailler, and J. Bourgade, "The laser megajoule (lmj) project dedicated to inertial confinement fusion: Development and construction status," *Fusion Engineering and design*, vol. 74, no. 1-4, pp. 147–154, 2005.

[21] H. Azechi, M. Nakai, K. Shigemori, N. Miyanaga, H. Shiraga, H. Nishimura, M. Honda, R. Ishizaki, J. Wouchuk, H. Takabe, *et al.*, "Direct-drive hydrodynamic instability experiments on the gekko xii laser," *Physics of Plasmas*, vol. 4, no. 11, pp. 4079–4089, 1997.

[22] S. Garanin, G. A. Kirillov, G. G. Kochemasov, L. S. Mkhitaryan, V. M. Murugov, S. A. Sukharev, and N. V. Zhidkov, "Investigations on inertial confinement fusion at the russian federal nuclear center—vniief," *Plasma Physics and Controlled Fusion*, vol. 45, p. A471, nov 2003.

[23] S. Jiang, F. Wang, Y. Ding, S. Liu, J. Yang, S. Li, T. Huang, Z. Cao, Z. Yang, X. Hu, *et al.*, "Experimental progress of inertial confinement fusion based at the shenguang-iii laser facility in china," *Nuclear Fusion*, vol. 59, no. 3, p. 032006, 2018.

[24] E. Moses, R. Boyd, B. Remington, C. Keane, and R. Al-Ayat, "The national ignition facility: Ushering in a new age for high energy density science," *Physics of Plasmas*, vol. 16, no. 4, 2009.

[25] T. Boehly, D. Brown, R. Craxton, R. Keck, J. Knauer, *et al.*, "Initial performance results of the omega laser system," *Optics Communications*, vol. 133, no. 1-6, pp. 495–506, 1997.

[26] G. Miller, E. Moses, and C. Wuest, "The national ignition facility: enabling fusion ignition for the 21st century," *Nuclear fusion*, vol. 44, no. 12, p. S228, 2004.

[27] S. Skupsky, J. Marozas, R. Craxton, R. Betti, T. Collins, J. Delettrez, *et al.*, "Polar direct drive on the national ignition facility," *Physics of Plasmas*, vol. 11, no. 5, pp. 2763–2770, 2004.

[28] M. Hohenberger, P. Radha, J. Myatt, S. LePape, J. Marozas, F. Marshall, *et al.*, "Polar-direct-drive experiments on the national ignition facility," *Physics of Plasmas*, vol. 22, no. 5, 2015.

[29] J. Lawson, "Some criteria for a power producing thermonuclear reactor," *Proceedings of the Physical Society. Section B*, vol. 70, p. 6, Jan 1957.

[30] R. Aymar, P. Barabaschi, and Y. Shimomura, "The iter design," *Plasma physics and controlled fusion*, vol. 44, no. 5, p. 519, 2002.

[31] A. Creely, M. J. Greenwald, S. B. Ballinger, D. Brunner, J. Canik, J. Doody, T. Fülöp, D. Garnier, R. Granetz, T. Gray, *et al.*, "Overview of the sparc tokamak," *Journal of Plasma Physics*, vol. 86, no. 5, p. 865860502, 2020.

[32] S. Wurzel and S. Hsu, "Progress toward fusion energy breakeven and gain as measured against the Lawson criterion," *Physics of Plasmas*, vol. 29, p. 062103, 06 2022.

[33] H. Abu-Shawareb, R. Acree, P. Adams, J. Adams, B. Addis, R. Aden, *et al.*, "Lawson criterion for ignition exceeded in an inertial fusion experiment," *Phys. Rev. Lett.*, vol. 129, p. 075001, Aug 2022.

[34] A. Kritcher, A. Zylstra, D. Callahan, O. Hurricane, C. Weber, D. Clark, and OTHERS, "Design of an inertial fusion experiment exceeding the lawson criterion for ignition," *Phys. Rev. E*, vol. 106, p. 025201, Aug 2022.

[35] A. Zylstra, A. Kritcher, O. Hurricane, D. Callahan, J. Ralph, D. Casey, *et al.*, "Experimental achievement and signatures of ignition at the national ignition facility," *Phys. Rev. E*, vol. 106, p. 025202, Aug 2022.

[36] A. Zylstra, O. Hurricane, D. Callahan, A. Kritcher, J. Ralph, H. Robey, *et al.*, "Burning plasma achieved in inertial fusion," *Nature*, vol. 601, no. 7894, pp. 542–548, 2022.

[37] "Lawrence livermore national laboratory achieves fusion ignition," *Lawrence LIvermore National Laboratory.*

[38] K. Chang, "A laser fusion breakthrough gets a bigger burst of energy," *New York Times.*

[39] S. Langer, I. Karlin, and M. Marinak, "Performance Characteristics of HYDRA-a Multi-Physics simulation code from Lawrence Livermore National Laboratory," tech. rep., Lawrence Livermore National Lab, Livermore, CA (United States), 2014.

[40] S. Lyon and J. Johnson, "Sesame: the los alamos national laboratory equation of state database. los alamos national laboratory, los alamos, nm," tech. rep., LA-UR-92-3407, 1992.

[41] J. MacFarlane, I. Golovkin, and P. Woodruff, "Helios-cr–a 1-d radiation-magnetohydrodynamics code with inline atomic kinetics modeling," *Journal of Quantitative Spectroscopy and Radiative Transfer*, vol. 99, no. 1-3, pp. 381–397, 2006.

[42] M. M. Marinak, G. D. Kerbel, N. A. Gentile, O. Jones, D. Munro, S. Pollaine, *et al.*, "Three-dimensional HYDRA simulations of National Ignition Facility targets," *Phys. Plasmas*, vol. 8, pp. 2275–2280, May 2001.

[43] W. Kruer, *The physics of laser plasma interactions.* crc Press, 2019.

[44] H. Scott and S. Hansen, "Advances in NLTE modeling for integrated simulations," *High Energy Density Phys.*, vol. 6, pp. 39–47, Jan 2010.

[45] J. R. Albritton, "NLTE/LTE Equation-Of-State Models," *AIP Conference Proceedings*, vol. 730, pp. 180–189, 10 2004.

[46] J. Sanz, R. Betti, V. A. Smalyuk, M. Olazabal-Loume, V. Drean, V. Tikhonchuk, *et al.*, "Radiation hydrodynamic theory of double ablation fronts in direct-drive inertial confinement fusion," *Phys. Plasmas*, vol. 16, no. 8, 2009.

[47] A. Thomas, M. Tzoufras, A. Robinson, R. Kingham, C. Ridgers, *et al.*, "A review of vlasov–fokker–planck numerical modeling of inertial confinement fusion plasma," *Journal of Computational Physics*, vol. 231, no. 3, pp. 1051–1079, 2012. Special Issue: Computational Plasma Physics.

[48] M. Tabak, D. S. Clark, S. P. Hatchett, M. H. Key, B. F. Lasinski, R. A. Snavely, *et al.*, "Review of progress in Fast Ignitiona)," *Physics of Plasmas*, vol. 12, 05 2005. 057305.

[49] R. Betti, C. D. Zhou, K. S. Anderson, L. J. Perkins, W. Theobald, and A. A. Solodov, "Shock ignition of thermonuclear fuel with high areal density," *Phys. Rev. Lett.*, vol. 98, p. 155001, Apr 2007.

[50] A. Bell and M. Tzoufras, "Electron transport and shock ignition," *Plasma Physics and Controlled Fusion*, vol. 53, p. 045010, mar 2011.

[51] S. Chapman and T. Cowling, *The Mathematical Theory of Non-uniform Gases: An Account of the Kinetic Theory of Viscosity, Thermal Conduction and Diffusion in Gases*. Cambridge Mathematical Library, Cambridge University Press, 1990.

[52] E. M. Epperlein and R. W. Short, "A practical nonlocal model for electron heat transport in laser plasmas," *Phys. Fluids B Plasma Phys.*, vol. 3, pp. 3092–3098, Nov 1991.

[53] J. R. Sanmartín, J. Ramírez, R. Fernández-Feria, and F. Minotti, "Self-consistent, nonlocal electron heat flux at arbitrary ion charge number," *Physics of Fluids B: Plasma Physics*, vol. 4, pp. 3579–3585, 11 1992.

[54] Y. Lee and R. More, "Electron conductivity model for dense plasmas," *Phys. Fluids; (United States)*.

[55] P. Mora and H. Yahi, "Thermal heat-flux reduction in laser-produced plasmas," *Phys. Rev. A*, vol. 26, pp. 2259–2261, Oct 1982.

[56] M. Rosen, H. Scott, D. Hinkel, E. Williams, D. Callahan, R. Town, *et al.*, "The role of a detailed configuration accounting (DCA) atomic physics package in explaining the energy balance in ignition-scale hohlraums," *High Energy Density Phys.*, vol. 7, pp. 180–190, Sep 2011.

[57] O. S. Jones, L. J. Suter, H. A. Scott, M. A. Barrios, W. A. Farmer, S. B. Hansen, *et al.*, "Progress towards a more predictive model for hohlraum radiation drive and symmetry," *Phys. Plasmas*, vol. 24, no. 5, 2017.

[58] E. M. Epperlein, R. W. Short, and A. Simon, "Damping of ion-acoustic waves in the presence of electron-ion collisions," *Phys. Rev. Lett.*, vol. 69, pp. 1765–1768, Sep 1992.

[59] J. R. Albritton, "Laser absorption and heat transport by non-Maxwell-Boltzmann electron distributions," *Phys. Rev. Lett.*, vol. 50, no. 26, pp. 2078–2081, 1983.

[60] A. R. Bell, R. G. Evans, and D. J. Nicholas, "Elecron Energy Transport in Steep Temperature Gradients in Laser-Produced Plasmas," *Phys. Rev. Lett.*, vol. 46, pp. 243–246, Jan 1981.

[61] J. F. Luciani, P. Mora, and J. Virmont, "Nonlocal heat transport due to steep temperature gradients," *Phys. Rev. Lett.*, vol. 51, no. 18, pp. 1664–1667, 1983.

[62] M. Sherlock, J. P. Brodrick, and C. P. Ridgers, "A comparison of non-local electron transport models for laser-plasmas relevant to inertial confinement fusion," *Phys. Plasmas*, vol. 24, p. 082706, Aug 2017.

[63] P. D. Nicolaï, J.-L. A. Feugeas, and G. P. Schurtz, "A practical nonlocal model for heat transport in magnetized laser plasmas," *Physics of Plasmas*, vol. 13, 03 2006. 032701.

[64] A. Marocchino, M. Tzoufras, S. Atzeni, A. Schiavi, P. D. Nicolaï, J. Mallet, *et al.*, "Comparison for non-local hydrodynamic thermal conduction models," *Phys. Plasmas*, vol. 20, no. 2, 2013.

[65] G. Schurtz, S. Gary, S. Hulin, C. Chenais-Popovics, J.-C. Gauthier, F. Thais, *et al.*, "Revisiting Nonlocal Electron-Energy Transport in Inertial-Fusion Conditions," *Phys. Rev. Lett.*, vol. 98, p. 095002, Feb 2007.

[66] D. Cao, G. Moses, and J. Delettrez, "Improved non-local electron thermal transport model for two-dimensional radiation hydrodynamics simulations," *Phys. Plasmas*, vol. 22, p. 082308, Aug 2015.

[67] K. H. Ma, M. V. Patel, M. Sherlock, W. A. Farmer, and E. Johnsen, "Thermal transport modeling of laser-irradiated spheres," *Physics of Plasmas*, vol. 29, 11 2022. 112307.

[68] A. Langdon, "Nonlinear Inverse Bremsstrahlung and Heated-Electron Distributions," *Phys. Rev. Lett.*, vol. 44, pp. 575–579, Mar 1980.

[69] R. Kidder, "Hot-electron preheat of laser-driven targets," *Nucl. Fusion*, vol. 21, pp. 145–151, Feb 1981.

[70] W. Seka, D. H. Edgell, J. P. Knauer, J. F. Myatt, A. V. Maximov, R. W. Short, *et al.*, "Time-resolved absorption in cryogenic and room-temperature direct-drive implosions," *Phys. Plasmas*, vol. 15, no. 5, p. 056312, 2008.

[71] T. R. Boehly, D. Munro, P. M. Celliers, R. E. Olson, D. G. Hicks, V. N. Goncharov, *et al.*, "Demonstration of the shock-timing technique for ignition targets on the National Ignition Facility," *Phys. Plasmas*, vol. 16, no. 5, 2009.

[72] S. G. Glendinning, S. N. Dixit, B. A. Hammel, D. H. Kalantar, M. H. Key, J. D. Kilkenny, *et al.*, "Measurement of a dispersion curve for linear-regime rayleigh-taylor growth rates in laser-driven planar targets," *Phys. Rev. Lett.*, vol. 78, no. 17, pp. 3318–3321, 1997.

[73] V. N. Goncharov, T. C. Sangster, P. B. Radha, R. Betti, T. R. Boehly, T. J. B. Collins, *et al.*, "Performance of direct-drive cryogenic targets on OMEGA," *Phys. Plasmas*, vol. 15, p. 056310, May 2008.

[74] W. Manheimer, D. Colombant, and V. Goncharov, "The development of a Krook model for nonlocal transport in laser produced plasmas. I. Basic theory," *Phys. Plasmas*, vol. 15, no. 8, 2008.

[75] D. Del Sorbo, J. L. Feugeas, P. Nicolaï, M. Olazabal-Loumé, B. Dubroca, S. Guisset, *et al.*, "Reduced entropic model for studies of multidimensional nonlocal transport in high-energy-density plasmas," *Phys. Plasmas*, vol. 22, no. 8, 2015.

[76] W. C. Mead, E. M. Campbell, K. G. Estabrook, R. E. Turner, W. L. Kruer, P. H. Y. Lee, *et al.*, "Laser-Plasma Interactions at 0.53 μm for Disk Targets of Varying <math display="inline"> <mi>Z</mi> </math>," *Phys. Rev. Lett.*, vol. 47, pp. 1289–1292, Nov 1981.

[77] E. L. Dewald, M. Rosen, S. H. Glenzer, L. J. Suter, F. Girard, J. P. Jadaud, *et al.*, "X-ray conversion efficiency of high-Z hohlraum wall materials for indirect drive ignition," *Phys. Plasmas*, vol. 15, p. 072706, Jul 2008.

[78] A. Sunahara, J. A. Delettrez, C. Stoeckl, R. W. Short, and S. Skupsky, "Time-Dependent Electron Thermal Flux Inhibition in Direct-Drive Laser Implosions," *Phys. Rev. Lett.*, vol. 91, no. 9, pp. 1–4, 2003.

[79] W. A. Farmer, M. D. Rosen, G. F. Swadling, C. Bruulsema, C. D. Harris, W. Rozmus, *et al.*, "Investigation of heat transport using directly driven gold spheres," *Physics of Plasmas*, vol. 28, no. 3, p. 032707, 2021.

[80] J. J. Thomson, W. L. Kruer, G. J. Caporaso, V. C. Rupert, W. C. Mead, D. W. Phillion, *et al.*, "The interaction of 1.06 μm laser radiation with high Z disk targets," *Phys. Fluids*, vol. 22, no. 10, p. 2020, 2003.

[81] P. Alaterre, H. Pépin, R. Fabbro, and B. Faral, "X-ray conversion efficiency as a function of atomic number for 0.26- μ m-laser – irradiated targets," *Phys. Rev. A*, vol. 34, pp. 4184–4194, Nov 1986.

[82] R. J. Henchen, M. Sherlock, W. Rozmus, J. Katz, D. Cao, J. P. Palastro, *et al.*, "Observation of Nonlocal Heat Flux Using Thomson Scattering," *Phys. Rev. Lett.*, vol. 121, p. 125001, Sep 2018.

[83] P. D. Goldstone, S. R. Goldman, W. C. Mead, J. A. Cobble, G. Stradling, R. H. Day, *et al.*, "Dynamics of high-Z plasmas produced by a short-wavelength laser," *Phys. Rev. Lett.*, vol. 59, no. 1, pp. 56–59, 1987.

[84] T. Mochizuki, T. Yabe, K. Okada, M. Hamada, N. Ikeda, S. Kiyokawa, *et al.*, "Atomic-number dependence of soft-x-ray emission from various targets irradiated by a 0.53- μ m-wavelength laser," *Phys. Rev. A*, vol. 33, pp. 525–539, Jan 1986.

[85] D. S. Montgomery, O. L. Landen, R. P. Drake, K. G. Estabrook, H. A. Baldis, S. H. Batha, *et al.*, "Measurements of Radial Heat Wave Propagation in Laser-Produced Exploding-Foil Plasmas," *Phys. Rev. Lett.*, vol. 73, pp. 2055–2058, Oct 1994.

[86] J. A. Stamper, K. Papadopoulos, R. N. Sudan, S. O. Dean, E. A. McLean, and J. M. Dawson, "Spontaneous Magnetic Fields in Laser-Produced Plasmas," *Phys. Rev. Lett.*, vol. 26, no. 17, pp. 1012–1015, 1971.

[87] W. A. Farmer, C. Bruulsema, G. F. Swadling, M. W. Sherlock, M. D. Rosen, W. Rozmus, *et al.*, "Validation of heat transport modeling using directly driven beryllium spheres," *Physics of Plasmas*, vol. 27, no. 8, p. 082701, 2020.

[88] R. Kingham and A. Bell, "An implicit Vlasov–Fokker–Planck code to model non-local electron transport in 2-D with magnetic fields," *J. Comput. Phys.*, vol. 194, pp. 1–34, Feb 2004.

[89] B. Chang, "A deterministic photon free method to solve radiation transfer equations," *J. Comput. Phys.*, vol. 222, no. 1, pp. 71–85, 2007.

[90] M. Tzoufras, A. Bell, P. Norreys, and F. Tsung, "A Vlasov–Fokker–Planck code for high energy density physics," *J. Comput. Phys.*, vol. 230, pp. 6475–6494, Jul 2011.

[91] S. Weng, Z. Sheng, and J. Zhang, "Inverse bremsstrahlung absorption with nonlinear effects of high laser intensity and non-Maxwellian distribution," *Phys. Rev. E - Stat. Nonlinear, Soft Matter Phys.*, vol. 80, no. 5, pp. 1–5, 2009.

[92] S. X. Hu, V. A. Smalyuk, V. N. Goncharov, S. Skupsky, T. C. Sangster, D. D. Meyerhofer, *et al.*, "Validation of Thermal-Transport Modeling with Direct-Drive, Planar-Foil Acceleration Experiments on OMEGA," *Phys. Rev. Lett.*, vol. 101, p. 055002, Jul 2008.

[93] W. M. Manheimer, "Steady-state planar ablative flow," *Phys. Fluids*, vol. 25, no. 9, p. 1644, 1982.

[94] G. Fiocco and E. Thompson, "Thomson Scattering of Optical Radiation from an Electron Beam," *Phys. Rev. Lett.*, vol. 10, pp. 89–91, Feb 1963.

[95] R. F. Schmalz, "Free unsteady expansion of a polytropic gas: Self-similar solutions," *Phys. Fluids*, vol. 29, no. 5, p. 1389, 1986.

[96] W. Seka, R. E. Bahr, R. W. Short, A. Simon, R. S. Craxton, D. S. Montgomery, *et al.*, "Nonlinear laser–matter interaction processes in long-scale-length plasmas," *Phys. Fluids B Plasma Phys.*, vol. 4, pp. 2232–2240, Mar 1992.

[97] A. Colaïtis, I. Igumenshchev, J. Mathiaud, and V. Goncharov, "Inverse ray tracing on icosahedral tetrahedron grids for non-linear laser plasma interaction coupled to 3d radiation hydrodynamics," *Journal of Computational Physics*, vol. 443, p. 110537, 2021.

[98] A. Colaïtis, D. P. Turnbull, I. V. Igumenschev, D. Edgell, R. C. Shah, O. M. Mannion, *et al.*, "3d simulations capture the persistent low-mode asymmetries evident in laser-direct-drive implosions on omega," *Phys. Rev. Lett.*, vol. 129, p. 095001, Aug 2022.

[99] J. M. Liu, J. S. De Groot, J. P. Matte, T. W. Johnston, and R. P. Drake, "Electron heat transport with non-Maxwellian distributions," *Physics of Plasmas*, vol. 1, pp. 3570–3576, 11 1994.

[100] K. G. Whitney and P. E. Pulsifer, "Plasma conditions for non-maxwellian electron distributions in high current discharges and laser-produced plasmas," *Phys. Rev. E*, vol. 47, pp. 1968–1976, Mar 1993.

[101] A. Zhidkov, A. Sasaki, I. Fukumoto, T. Tajima, T. Auguste, P. Oliveira, *et al.*, "Pulse duration effect on the distribution of energetic particles produced by intense femtosecond laser pulses irradiating solids," *Physics of Plasmas*, vol. 8, no. 8, pp. 3718–3723, 2001.

[102] V. L. Kantsyrev, D. A. Fedin, A. S. Shlyaptseva, S. Hansen, D. Chamberlain, and N. Ouart, "Energetic electron beam generation and anisotropy of hard x-ray emission from 0.9 to 1.0 MA high-Z X pinches," *Physics of Plasmas*, vol. 10, pp. 2519–2526, 05 2003.

[103] H. M. Smith and E. Verwichte, "Hot tail runaway electron generation in tokamak disruptions," *Physics of Plasmas*, vol. 15, p. 072502, 07 2008.

[104] M. H. Key, M. D. Cable, T. E. Cowan, K. G. Estabrook, B. A. Hammel, S. P. Hatchett, *et al.*, "Hot electron production and heating by hot electrons in fast ignitor research," *Physics of Plasmas*, vol. 5, pp. 1966–1972, 05 1998.

[105] M. Haines, M. S. Wei, F. N. Beg, and R. B. Stephens, "Hot-electron temperature and laser-light absorption in fast ignition," *Phys. Rev. Lett.*, vol. 102, p. 045008, Jan 2009.

[106] D. Montgomery, "Two decades of progress in understanding and control of laser plasma instabilities in indirect drive inertial fusion," *Physics of Plasmas*, vol. 23, no. 5, 2016.

[107] Y. Ping, R. Shepherd, B. F. Lasinski, M. Tabak, H. Chen, H. K. Chung, *et al.*, "Absorption of short laser pulses on solid targets in the ultrarelativistic regime," *Phys. Rev. Lett.*, vol. 100, p. 085004, Feb 2008.

[108] J. Matte, M. Lamoureux, C. Moller, R. Yin, J. Delettrez, J. Virmont, *et al.*, "Non-maxwellian electron distributions and continuum x-ray emission in inverse bremsstrahlung heated plasmas," *Plasma Physics and Controlled Fusion*, vol. 30, p. 1665, nov 1988.

[109] R. Yan, C. Ren, J. Li, A. Maximov, W. Mori, Z. Sheng, *et al.*, "Generating energetic electrons through staged acceleration in the two-plasmon-decay instability in inertial confinement fusion," *Physical review letters*, vol. 108, no. 17, p. 175002, 2012.

[110] V. Zakharov *et al.*, "Collapse of langmuir waves," *Sov. Phys. JETP*, vol. 35, no. 5, pp. 908–914, 1972.

[111] H. X. Vu, D. F. DuBois, J. F. Myatt, and D. A. Russell, "Hot-electron production and suprathermal heat flux scaling with laser intensity from the two-plasmon–decay instability," *Physics of Plasmas*, vol. 19, p. 102703, 10 2012.

[112] M. Lamoureux, "Atomic physics and non-maxwellian plasmas," in *Advances in atomic, molecular, and optical physics*, vol. 31, pp. 233–295, Elsevier, 1993.

[113] D. J. Strozzi, D. S. Bailey, P. Michel, L. Divol, S. M. Sepke, G. D. Kerbel, *et al.*, "Interplay of laser-plasma interactions and inertial fusion hydrodynamics," *Phys. Rev. Lett.*, vol. 118, p. 025002, Jan 2017.

[114] I. V. Igumenshchev, W. Seka, D. H. Edgell, D. T. Michel, D. H. Froula, V. N. Goncharov, *et al.*, "Crossed-beam energy transfer in direct-drive implosionsa)," *Physics of Plasmas*, vol. 19, p. 056314, 05 2012.

[115] A. Colaitis, R. K. Follett, J. P. Palastro, I. Igumenschev, and V. Goncharov, "Adaptive inverse ray-tracing for accurate and efficient modeling of cross beam energy transfer in hydrodynamics simulations," *Physics of Plasmas*, vol. 26, p. 072706, 07 2019.

[116] K. Li and W. Huo, "The nonlocal electron heat transport under the non-Maxwellian distribution in laser plasmas and its influence on laser ablation," *Physics of Plasmas*, vol. 30, p. 042702, 04 2023.

[117] G. Gregori, S. H. Glenzer, J. Knight, C. Niemann, D. Price, D. H. Froula, *et al.*, "Effect of nonlocal transport on heat-wave propagation," *Phys. Rev. Lett.*, vol. 92, p. 205006, May 2004.

[118] T. Ditmire, R. A. Smith, J. W. G. Tisch, and M. H. R. Hutchinson, "High intensity laser absorption by gases of atomic clusters," *Phys. Rev. Lett.*, vol. 78, pp. 3121–3124, Apr 1997.

[119] B. Scheiner and M. Schmitt, "Considerations for the modeling of the laser ablation region of icf targets with lagrangian simulations," *AIP Advances*, vol. 11, no. 10, p. 105208, 2021.